National Technical University of Athens
School of Mechanical Engineering
Fluids Section
Parallel CFD & Optimization Unit

Contribution to constraint handling in CFD topology and shape optimization

Diploma Thesis

Othon Valeras

Advisor: Kyriakos C. Giannakoglou, Professor NTUA

Athens, February 2025

Contents

1 Introduction **7**

1.1 CFD Topology Optimization . . . 7

1.2 CFD Shape Optimization . . . 9

1.3 Optimization Algorithms . . . 10

1.4 Thesis Structure . . . 13

2 Adjoint Solvers **15**

2.1 Primal Problem . . . 15

2.1.1 Primal Problem in ShpO . . . 15

2.1.2 Primal Problem in TopO . . . 16

2.1.3 Primal Problem in CHT TopO . . . 18

2.2 Adjoint Problem . . . 19

2.2.1 Adjoint Problem in ShpO . . . 19

2.2.2 Adjoint Problem in TopO . . . 20

2.2.3 Adjoint Problem in CHT TopO . . . 20

2.3 Primal-Adjoint Optimization Algorithm . . . 21

3 Sequential Quadratic Programming **22**

3.1 Relaxation of Constraints By Introducing Extra Design Variables . . . 22

3.2 Optimality Conditions for QP Sub-Problem . . . 25

3.3 Extra Design Variables Multiplier's Influence In SQP Solution . . . 26

4 Overcoming SQP Issues - Demonstrations in TopO **29**

4.1 TopO Applications Using Constant Factor's Values . . . 30

4.1.1 Case 1 - 2D . . . 30

4.1.2 Case 2 - 2D . . . 31

4.1.3 Case 3 - 3D . . . 31

4.1.4 Case 4 - 3D . . . 32

4.2 TopO Applications Using Varying Factor's Values . . . 33

4.2.1 Case 1 - 2D 35
4.2.2 Case 2 - 2D 35
4.2.3 Case 3 - 3D 36
4.2.4 Case 4 - 3D 37

5 Overcoming SQP Issues - Demonstrations in ShpO **49**
5.1 NACA0012 With Control Box A 50
5.2 NACA0012 With Control Box B 52
5.3 TU Berlin TurboLab Stator Blade 53

6 Overcoming SQP Issues - Demonstrations in CHT TopO **65**
6.1 Objective's components weights: 95% - 5% 67
6.2 Objective's components weights: 90% - 10% 70
6.3 Objective's components weights: 80% - 20% 73

7 Summary - Conclusion **78**

National Technical University of Athens
School of Mechanical Engineering
Fluids Section
Parallel CFD & Optimization Unit

Contribution to constraint handling in CFD topology and shape optimization

Diploma Thesis

Othon Valeras

Supervisor: Kyriakos C. Giannakoglou, Professor NTUA

Athens, February 2025

Abstract

This diploma thesis involves solving CFD-related, shape, and topology optimization (ShpO and TopO) problems with constraints. A gradient-based approach is utilized that includes the continuous adjoint method which computes the gradients of the objective and constraint functions with respect to (w.r.t) the design variables. For that purpose, the implied optimization tool has been the primal-adjoint solver of OpenFOAM® library, with an improved SQP approach for the design variable update. The improvement lies in the modification made for better handling problems with constraints, which cannot be satisfied at the initial optimization cycles or become unsatisfied as the optimization routine progresses. In some cases, these constraints have been shown to lead the optimization algorithm in low-quality or/and pure solutions, resulting in impractical generated geometries. The modifications proposed are related to a parameter that can drastically influence the convergence speed and the final solutions acquired by the existing OpenFOAM SQP algorithm.

To test the proposed SQP algorithm, a number of 2D and 3D benchmarks is evaluated. Specifically, three aerodynamic TopO problems are solved: (i) a 2D, laminar, single-inlet dual-outlet case, (ii) a 2D, turbulent, single-inlet dual-outlet case, (iii) a 3D, turbulent, single-inlet dual-outlet case, which corresponds to an air-duct design problem for automotive HVAC applications, and (iv) a similar 3D, turbulent, single-inlet triple-outlet case.

Three aerodynamic ShpO problems are investigated: (i) a laminar NACA0012 airfoil case, (ii)

a similar turbulent case with different control box settings, and (iii) a 2D, turbulent stator blade optimization.

Finally, three 2D, mono-fluid, conjugate heat transfer topology optimization problems are examined. In all cases, aluminum heat sinks are generated using a turbulent, 2D, 1-inlet-1-outlet setup. A heat exchange-related and a fluid-related terms are scaled and added to create the objective function of these problems, with varying weight coefficients across different cases.

The goal of this diploma thesis is to test the proposed SQP setup and explore its optimal tuning, for solving laminar or turbulent, 2D or 3D, topology and shape optimization problems, in aerodynamic or conjugate heat transfer applications.

Εθνικό Μετσόβιο Πολυτεχνείο
Σχολή Μηχανολόγων Μηχανικών
Τομέας Ρευστών
Μονάδα Παράλληλης Υπολογιστικής Ρευστοδυναμικής
& Βελτιστοποίησης

Συμβολή στη διαχείριση περιορισμών σε προβλήματα βελτιστοποίησης μορφής και τοπολογίας στην Υπολογιστική Ρευστοδυναμική

Διπλωματική Εργασία

Όθων Βαλεράς

Επιβλέπων: Κυριάκος Χ. Γιαννάκογλου, Καθηγητής ΕΜΠ

Αθήνα, Φεβρουάριος 2025

Περίληψη

Αυτή η διπλωματική εργασία αναφέρεται στην βελτιστοποίηση σχήματος και τοπολογίας (ShpO και TopO) σε προβλήματα υπολογιστικής ρευστοδυναμικής (CFD) υπό περιορισμούς. Χρησιμοποιείται μια μέθοδος βασισμένη στις κλίσεις (gradient-based method), η οποία περιλαμβάνει τη συνεχή συζυγή μέθοδο (continuous adjoint method) για τον υπολογισμό των παραγώγων ευαισθησίας της αντικειμενικής συνάρτησης και των περιορισμών ως προς τις μεταβλητές σχεδιασμού. Για τον σκοπό αυτό, ο κώδικας βελτιστοποίησης που χρησιμοποιείται είναι ο primal-adjoint επιλύτης της βιβλιοθήκης OpenFOAM®, σε συνδυασμό με μια βελτιωμένη προσέγγιση SQP για την ενημέρωση των μεταβλητών σχεδιασμού. Η βελτίωση έγκειται σε τροποποιήσεις που επιτρέπουν καλύτερο χειρισμό προβλημάτων με περιορισμούς, οι οποίοι είτε δεν ικανοποιούνται στους αρχικούς κύκλους της βελτιστοποίησης είτε παραβιάζονται κατά την εξέλιξη της διαδικασίας. Σε ορισμένες περιπτώσεις, αυτοί οι περιορισμοί οδηγούν τον αλγόριθμο βελτιστοποίησης σε λύσεις ανεπαρκής ποιότητας ή σε τεχνολογικά, μη πρακτικές γεωμετρίες. Οι προτεινόμενες τροποποιήσεις σχετίζονται με μια παράμετρο που επηρεάζει δραστικά την ταχύτητα σύγκλισης και τις τελικές λύσεις που προκύπτουν από τον υπάρχοντα αλγόριθμο SQP του OpenFOAM.

Για τη δοκιμή του αλγορίθμου SQP, αξιολογούνται αρκετές 2D και 3D περιπτώσεις αναφοράς. Συγκεκριμένα, επιλύονται τρία αεροδυναμικά προβλήματα βελτιστοποίησης τοπολογίας: (i) ένα διδιάστατο, στρωτό, πρόβλημα με μία είσοδο και δύο εξόδους, (ii) ένα διδιάστατο, τυρβώδες, πρόβλημα με μία είσοδο και δύο εξόδους, (iii) ένα τρισδιάστατο, τυρβώδες πρόβλημα με μία είσοδο και δύο εξόδους, που αφορά τον σχεδιασμό αεραγωγού για HVAC εφαρμογές στην αυ-

τοκινητοβιομηχανία, καθώς και (iv) ένα παρόμοιο τρισδιάστατο, τυρβώδες πρόβλημα με μία είσοδο και τρεις εξόδους.

Επιπλέον, διερευνώνται τρία προβλήματα αεροδυναμικής βελτιστοποίησης σχήματος: (i) η βελτιστοποίηση μιας αεροτομής NACA0012, σε στρωτή ροή (ii) ένα αντίστοιχο τυρβώδες πρόβλημα με διαφορετικές ρυθμίσεις των σημείων ελέγχου, και (iii) η βελτιστοποίηση του σχήματος ενός διδιάστατης, σταθερού πτερυγίου στροβιλομηχανής.

Τέλος, εξετάζονται τρία, διδιάστατα προβλήματα βελτιστοποίησης τοπολογίας συζευγμένης μεταφοράς θερμότητας (Conjugate Heat Transfer), ενός ρευστού. Σε όλες τις περιπτώσεις, παράγονται διδιάστατες ψύκτρες αλουμινίου με μία είσοδο και μία έξοδο. Στις αντικειμενικές συναρτήσεις αυτών των προβλημάτων συνδυάζονται, με διαφορετικούς συντελεστές βαρύτητας, δύο όροι που σχετίζονται με τη μεταφορά θερμότητας και με τη ροή του ρευστού.

Στόχος αυτής της διπλωματικής εργασίας είναι η δοκιμή του προτεινόμενου SQP αλγορίθμου και η διερεύνηση της βέλτιστης ρύθμισής του, για την επίλυση προβλημάτων βελτιστοποίησης σχήματος και τοπολογίας, σε ροές στρωτές ή τυρβώδεις, δισδιάστατες ή τρισδιάστατες, με εφαρμογές στην αεροδυναμική και τη συζευγμένη μεταφορά θερμότητας.

Chapter 1

Introduction

Computational Fluid Dynamics (CFD) methods have become an indispensable tool to solve and analyze complex fluid dynamics problems in various engineering fields, such as in aeronautics [1], automotive engineering [2, 3], thermal and hydraulic turbomachinery [4], weather forecasting, to mention a few of them. The exponential growth of computational power and the increasing availability of modern High-Performance Computing (HPC) systems during the last decades, combined with the development of more efficient methods for predicting fluid flow behavior, has allowed CFD to largely replace expensive and time-consuming experiments in the design-optimization process of aero/hydrodynamic components. Despite notable advancements in CFD methods, challenges persist in accurately simulating turbulent flows with reasonable computational cost, due to the wide range of spatial and temporal scales of vortical structures.

1.1 CFD Topology Optimization

Topology Optimization (TopO) [5, 6] involves the pursuit of obtaining a better qualified design for a specific application by altering the material composition within its design space, while also satisfying the governing equations and design constraints. Introduced and almost matured in solid mechanics [7], TopO has been extended to various scientific fields due to the flexibility it offers, as it is not bounded by an a priori defined shape or topology. In fluid mechanics in specific, TopO has successfully been applied in Stokes [8], laminar [9, 10], and turbulent [11, 12], steady, and unsteady [13, 14, 15] flows. TopO's predominant methodology in fluid mechanics is via the porosity-based approach (a.k.a. the Brinkman penalization method), in which a porous material is introduced and controlled, giving rise to the design variables of the case. Solid regions are characterized by low porosity or high impermeability, impeding fluid flow by enforcing a zero velocity. The ability to radically change the topology of

the solution during the optimization cycles and the fairly simple implementation are the main advantages of the porosity-based TopO. Its main weakness is related to accuracy issues, as it cannot account for the accurate effect of solid walls on the computed flow field. Also, staircase effects, instead of curved boundaries, may result, whereas narrow solid regions cannot accurately be simulated, as pressure diffuses through the solid regions [16, 17]. This is why, optimized solutions computed by standard porosity-based TopO require re-evaluation using flow solvers running on body-fitted meshes. The extraction of the optimal body shape from the optimized porosity field becomes necessary and this is not a straightforward task which, among other, may impair the quality of the optimized solution since the re-evaluation usually computes a (slightly) different performance value. For this reason, after parameterizing the so-extracted boundaries, a shape optimization (ShpO) using this parameterization may follow to further refine the optimized solution [18].

These shortcomings of the porosity-based approach, the increasing complexity of TopO applications as well as the need to compute sharp fluid-solid interfaces [17, 19, 20], have rejuvenated surface-capturing approaches, in which solid boundaries are reconstructed during the optimization process rather than upon its completion, usually via level-set computations on fixed background meshes [16, 21, 22]. Capturing the solid surface anew within each optimization cycle allows for the imposition of accurate boundary conditions. In level-set TopO methods, the zero-level iso-surfaces are displaced by the computed sensitivity derivatives; these support topological changes such as boundary-merging, boundary-splitting, and boundary disappearance [23]. However, for the generation of new solid boundaries, i.e. the appearance of new fluid-solid interfaces inside the fluid domain, extra treatment is required [24].

Another approach to eliminate the porosity-based TopO approach is the cut-cell TopO method [25], which computes the intersections of the Fluid-Solid Interface (FSI) with the cells of the background CFD grid in each optimization cycle. This leads in cut-cell TopO method which is still based on the impermeability field pf porosity-based TopO. However, in contrast to porosity-based TopO, this is used exclusively to compute the FSI. The solution of the flow equations is, thus, performed on the cut-cell grid, allowing the imposition of exact boundary conditions on the FSI. ShpO is no more needed, and accurate performance values as well as a clear FSI become available.

1.2 CFD Shape Optimization

In ShpO [26], shapes (wings, vehicles, blades, etc) to be optimized according to userdefined objectives and constraints, are controlled using a shape parameterization technique. The selection of such a technique is crucial since it determines the design space to be explored, highly affecting the whole optimization process and the quality of the optimized designs. In general, they can be classified into two main categories: Computer-Aided Design (CAD)-free and CAD-based.

CAD-free parameterization techniques include node-based and free-form deformation approaches. The former directly control the coordinates of the nodes on the body surface, giving the richest possible design space. However, the independent displacement of each surface node may lead to high-frequency, noisy optimized shapes that might cause numerical instability in the subsequent optimization cycles or be unacceptable during manufacturing. To ensure smooth design updates, filtering functions are typically used. In free-form deformation, the shape to be optimized is enclosed by a lattice of control points, the coordinates of which constitute the design variables. Basis functions (such as radial basis functions, harmonic coordinates, Non-Uniform Rational B-Splines (NURBS) or volumetric B-splines) interpolate the displacement of each control point to the surface nodes of the CFD grid. Some of those techniques can simultaneously control both the boundary and (part of) the associated CFD grid.

The main drawback of CAD-free parameterization techniques is their inherent difficulty in importing the optimized geometry back into the CAD environment, as part of the iterative design process between different engineering departments or for final manufacturing. Returning to CAD is not trivial and often impairs the quality of designed shapes. Conversely, CAD-based parameterization techniques use as design variables either the native CAD model parameters or the control points of NURBS patches. Consequently, the optimized shapes already exist in a CAD format, such as the STEP format. Techniques using the native CAD model parameters as design variables may offer the best compromise between complexity and manufacturability but, in general, are difficult to be incorporated in a fully automated optimization workflow.

This thesis exclusively relies on CAD-free parameterization techniques. In particular, the design variables are the Cartesian coordinates of the control points of volumetric B-splines lattices, morphing the shape to be optimized and the part of the CFD grid encapsulated into the lattices. At each optimization cycle, this part of the grid is deformed following the displacement of the control points, eliminating the need to regenerate the grid.

1.3 Optimization Algorithms

Having defined the design variables of the optimization problem, a method must be selected to search for the optimal solution. Based on this criterion, CFD-based optimization methods can be categorized into stochastic (or gradient-free) and deterministic (or gradient-based). The most widely used representative of stochastic methods are the Evolutionary Algorithms (EAs) [27], which mimic the Darwinian evolution of species. EAs apply natural evolution operations, like crossover, mutation and elitism to evolve a set of candidate solutions (i.e. sets of design variables) from one generation to the next, searching for the best performing candidate solution. Provided that the optimization runs for a sufficient number of generations, EAs can locate the global optimum for a given set of design variables and their user-defined bounds. An additional advantage of EAs is that they do not require access to the source code of the software used to evaluate the objective function(s) and constraint(s), which means that an EA platform can be used in any optimization problem, using the corresponding evaluation software (flow solver, in a CFD application) as a "black box". Moreover, EAs can compute Pareto fronts of non-dominated solutions in multi-objective optimization problems, with a single run. However, the main disadvantage of EAs is that a large number of candidate solutions must be evaluated before reaching the optimal one(s), especially as the number of design variables increases. Practically, the number of the flow evaluations scales with the number of design variables. Various techniques have been proposed to decrease the computational cost and the turn-around time of EAs. Among other, these include the use of parallel EAs [28, 29], asynchronous EAs, suitable for heterogeneous multiprocessor platforms, and metamodel-assisted EAs [30, 31] which use a surrogate evaluation model to reduce the required number of computationally expensive CFD evaluations. Stochastic methods are beyond the scope of this thesis and are not discussed further.

Gradient-based methods [32] improve a given shape based on information related to the derivatives of the objective and constraint function(s) J with respect to (w.r.t.) the design variables, a.k.a. Sensitivity Derivatives (SDs). SDs dictate the search directions in the design space that the optimization should follow to minimize or maximize J. In general, gradient-based methods require fewer flow evaluations than EAs to reach an optimized shape, although they are more prone to becoming trapped into local minima. The efficiency of gradient-based methods strongly depends on the method used to compute SDs. The most straightforward method for computing SDs is through Finite Differences (FDs). Each design variable is perturbed by an infinitesimally small value, ϵ, and the objective function is re-evaluated on the perturbed design. For second-order accurate scheme, central FDs read

$$\frac{\partial J}{\partial b_n} = \frac{J(b_1, ..., b_n + \epsilon, ..., b_N) - J(b_1, ..., b_n - \epsilon, ..., b_N)}{2\epsilon} \tag{1.1}$$

Despite its simple implementation, the computational cost of FDs scales linearly with the number N of design variables, requiring $2N$ solutions of the flow Partial Differential Equations (PDEs), making it infeasible for practical optimization problems with many design variables. Additionally, the accuracy of $\delta J/\delta b_n$ highly depends on ϵ, the value of which is difficult to determine a priori. Large values increase truncation errors, while small values introduce round-off errors. To minimize the latter, the flow equations must be sufficiently converged, which might not always be possible in industrial applications.

Direct differentiation [33] is another method for computing SDs. To compute the derivatives of the flow variables w.r.t. to b_n appearing in the expression of SDs, the flow equations are differentiated w.r.t. b_n leading to N linear systems that must be solved, thus yielding a cost that scales with N. Practically, direct differentiation is as costly as FDs, with the extra burden of developing the equations and programming the corresponding software, but without the ambiguities associated with the value of ϵ. Nevertheless, direct differentiation is used in algorithms computing high-order SDs [34].

In contrast, the adjoint method computes SDs at a cost that is practically independent of the number of design variables and, more or less, equal to that of the numerical solution of the primal (i.e. flow, in a CFD application) problem. The adjoint method [35] defines the augmented objective function (or Lagrangian) L as the sum of J and the field integrals of the flow equations multiplied by the corresponding adjoint (or Lagrange multiplier) fields. Essentially, $L = J$ and $\delta L/\delta b_n = \delta J/\delta b_n$. The adjoint fields are introduced to provide the necessary degrees of freedom to eliminate the derivatives of the flow variables w.r.t. to b_n from the SDs expression. This is achieved by satisfying the field adjoint equations and adjoint boundary conditions. The remaining terms in $\delta L/\delta b_n$ depend on both the primal and adjoint fields and form the adjoint SDs.

Adjoint methods are categorized into continuous and discrete ones. In continuous adjoint, the objective function and primal equations are first differentiated w.r.t. bn and the adjoint equations are derived in the form of PDEs, i.e. in continuous form, which then require discretization for being numerically solved. Alternatively, working with both J and the primal equations in discrete form, their differentiation gives rise to the discrete adjoint method [36], in which the adjoint equations are directly derived in discrete form. This thesis relies on the continuous adjoint method.

Having computed SDs, the design variables values are updated. Gradient $\delta J/\delta b$ is orthogonal to the level sets (iso-surfaces) of J in the design space, pointing toward the direction with the greatest rate of increase in J value. The steepest descent method, one of the oldest methods for unconstrained optimization, relies on the observation that a continuous function should increase/decrease, at least initially, if one takes a step along the direction of the positive/negative gradient. However, steepest descent is known for its slow convergence, especially when approaching a stationary point. Alternative methods include Newton methods which use the exact Hessian matrix $\nabla^2 J$ and quasi-Newton which rely on approximations to $\nabla^2 J$, such as the Broyden-Fletcher-Goldfarb-Shanno (BFGS) algorithm [37] and the SR1 [38]. The Fletcher-Reeves conjugate gradients method [39] is another alternative which is more effective than steepest descent. Despite being more robust than Newton or quasi-Newton methods, conjugate gradients method do not attain the fast convergence rates of the latter.

Another class of optimization update methods is designed to handle constraints effectively while improving convergence. Among the most widely used approaches are the Method of Moving Asymptotes (MMA) and Sequential Quadratic Programming (SQP).

MMA [40] is a first-order optimization method specifically designed for topology and shape optimization problems with constraints. It introduces individual moving asymptotes for each design variable, dynamically adjusting the search space to improve numerical stability and convergence [41]. The method formulates the subproblem as a convex, separable programming problem, allowing for efficient solutions even when handling large numbers of design variables [42]. MMA is particularly well suited for structural and CFD-based shape optimization problems, where the design space is complex and traditional methods struggle with constraint handling [43]. It has been widely adopted in engineering applications due to its robustness and efficiency in dealing with highly nonlinear and ill-conditioned problems [44].

On the other hand, SQP [45] is an iterative method that approximates the original nonlinear optimization problem by solving a sequence of quadratic programming (QP) subproblems. Each subproblem is derived by locally approximating the objective function and constraints using a quadratic Taylor series expansion and a linearization of the constraints, respectively [46]. The resulting QP problem is then solved to obtain a search direction, which updates the design variables while maintaining feasibility with respect to the constraints. SQP methods have been extensively applied in CFD-based shape optimization due to their strong theoretical foundation and fast convergence properties [47]. However, they require the Hessian of the

Lagrangian function, which can be computationally expensive to compute and thus techniques such as BFGS approximations are often employed to alleviate this cost.

1.4 Thesis Structure

Chapter 2: A brief introduction in TopO and ShpO and the continuous adjoint for the calculation of the sensitivity derivatives in CFD problems.

Chapter 3: The mathematical framework of the SQP algorithm for constrained optimization, taking into account constraint infeasibility, using additional design variables.

Chapter 4: TopO case studies in 2D and 3D geometries. That includes:

1. A 2D, laminar, single-inlet dual-outlet case, where the objective is the minimization of total pressure losses while enforcing a volume-occupied-by-fluid constraint, used in the porosity-based TopO approach.

2. A 2D turbulent single-inlet, dual-outlet case, where the objectives remain the minimization of total pressure losses and the enforcement of the volume-occupied-by-fluid constraint, with an additional constraint ensuring equal mass partitioning at the outlets.

3. A 3D, turbulent, single-inlet dual-outlet case, which corresponds to an air-duct design problem for automotive HVAC applications. The objective is to minimize a flow uniformity index at the outlets while satisfying three constraints: the volume-occupied-by-fluid constraint, the equal-outlet-mass-partition constraint, and a target total-pressure-loss constraint.

4. A 3D, turbulent, single-inlet triple-outlet case, which corresponds to an air-duct design problem for automotive HVAC applications. The objective is to minimize a flow uniformity index at the outlets while satisfying three constraints: the volume-occupied-by-fluid constraint, the equal-outlet-mass-partition constraint, and a target total-pressure-loss constraint.

Chapter 5: ShpO case studies in 2D geometries. That includes:

1. A 2D, laminar optimization case of a NACA0012-airfoil. The objective is the minimization of drag, while satisfying an airfoil-minimum-volume constraint and a lift-target constraint.

2. A similar, turbulent NACA0012-airfoil case with different control box settings.

3. A 2D, turbulent optimization case revolving the TU Berlin TurboLab Stator Blade. The objective is the minimization of total pressure losses satisfying an airfoil-minimum-volume constraint and an target exit-flow-angle constraint.

Chapter 6: Three 2D, mono-fluid, conjugate heat transfer topology optimization cases, in which aluminum heat sinks are generated using a turbulent, 2D, single-inlet single-outlet setup. The objective is the weighted sum of the mean domain temperature and the total pressure losses, satisfying a volume-occupied-by-fluid constraint. In each case, the weights vary to transfer objective influence from the mean-temperature term to the total-pressure-losses term. At the end of the chapter, the best solutions of each benchmarks form part of a Pareto front.

Chapter 7: Presentation of conclusions drawn from the research performed in the thesis, along with suggestions for future work.

Chapter 2

Adjoint Solvers

2.1 Primal Problem

All optimization problems presented in this diploma thesis are governed by the steady, (laminar or turbulent) flow equations for incompressible flows. These define the fluid primal problem, which is modeled using either the Navier-Stokes or the Reynolds-Averaged Navier-Stokes (RANS) equations for laminar and turbulent flow respectively. The latter consists of the Reynolds-averaged continuity and momentum conservation equations, alongside the turbulence model equations. In this thesis, the Spalart-Allmaras model is used, together with the Eikonal equation computing distances (Δ) of the internal cells from the solid walls. In Conjugate Heat Transfer (CHT) cases presented in Chapter 6, the energy conservation equation is solved after the RANS-Spalart-Allmaras-Eikonal set of equations, concluding the primal problem solving step.

2.1.1 Primal Problem in ShpO

The primal equations used in ShpO [3], augmented with the Spalart-Allmaras equation, are presented below:

$$\text{Continuity:} \quad R_p = \frac{\partial u_i}{\partial x_i} = 0, \quad i = 1, 2(, 3) \tag{2.1}$$

$$\text{Momentum:} \quad R_{u,i} = u_j \frac{\partial u_i}{\partial x_j} + \frac{\partial p}{\partial x_i} - \frac{\partial \tau_{ij}}{\partial x_j} = 0 \tag{2.2}$$

$$\text{Turbulence:} \quad R_{\tilde{\nu}} = v_j \frac{\partial \tilde{\nu}}{\partial x_j} - \frac{\partial}{\partial x_j}\left[\left(\nu + \frac{\tilde{\nu}}{\sigma}\right)\frac{\partial \tilde{\nu}}{\partial x_j}\right] - \frac{c_{b2}}{\sigma}\left(\frac{\partial \tilde{\nu}}{\partial x_j}\right)^2 - \tilde{\nu}P(\tilde{\nu}) + \tilde{\nu}D(\tilde{\nu}) = 0. \tag{2.3}$$

$$\text{Eikonal:} \quad R_\Delta = \frac{\partial}{\partial x_j}\left(\frac{\partial \Delta}{\partial x_j}\Delta\right) - \Delta\frac{\partial^2 \Delta}{\partial x_j^2} - 1 = 0 \tag{2.4}$$

where u_i are the velocity components, p the pressure divided by the density, τ_{ij} the stress tensor given by: $\tau_{ij} = (\nu + \nu_t)\left(\frac{\partial u_i}{\partial x_j} + \frac{\partial u_j}{\partial x_i}\right)$, ν and ν_t the bulk and eddy viscosity coefficients respectively.

2.1.2 Primal Problem in TopO

In the porosity approach implemented in the OpenFOAM optimization library, *adjointOptimization*, the porosity scalar field α is introduced, ranging from 0 to 1 and interpolating the solid and the fluid regions. The values equal to 0 represent the fluid region and values equal to 1 the solid region. Source terms (also referred to as Brinkman penalization source terms) augment the initial conservation equations, which either drive the solution towards values corresponding to solid walls, by deactivating the equations at the solid region(continuity and momentum equations). In CHT problems, the energy equation source term also interpolates between the thermo-physical properties of the fluid and solidified domains [30, 31]. The Brinkman-augmented RANS-Spalart-Allmaras primal set of equations solved in TopO [6] problems are presented:

$$\text{Continuity:} \quad R_p = \frac{\partial u_i}{\partial x_i} = 0, \qquad i = 1, 2(, 3) \tag{2.5}$$

$$\text{Momentum:} \quad R_{u,i} = u_j \frac{\partial u_i}{\partial x_j} + \frac{\partial p}{\partial x_i} - \frac{\partial \tau_{ij}}{\partial x_j} + \beta_{max} I^u(\beta) u_i = 0 \tag{2.6}$$

$$\text{Turbulence:} \quad R_{\tilde{\nu}} = v_j \frac{\partial \tilde{\nu}}{\partial x_j} - \frac{\partial}{\partial x_j}\left[\left(\nu + \frac{\tilde{\nu}}{\sigma}\right)\frac{\partial \tilde{\nu}}{\partial x_j}\right] - \frac{c_{b2}}{\sigma}\left(\frac{\partial \tilde{\nu}}{\partial x_j}\right)^2 \tag{2.7}$$

$$- \tilde{\nu}P(\tilde{\nu}) + \tilde{\nu}D(\tilde{\nu}) + \beta_{\max} I_{\tilde{\nu}}(\beta)\tilde{\nu} = 0 \tag{2.8}$$

$$\text{Eikonal:} \quad R_\Delta = \frac{\partial}{\partial x_j}\left(\frac{\partial \Delta}{\partial x_j}\Delta\right) - \Delta\frac{\partial^2 \Delta}{\partial x_j^2} - 1 + \beta_{\max} I_\Delta(\beta)\Delta = 0 \tag{2.9}$$

where β is a function of α with the same physical interpretations and value range, β_{max} a scalar quantity used to ensure that the u_i values are practically zero in the solidified domain. Its value can be computed based on the Darcy number, quantifying the ratio between viscous and porous forces,

$$Da = \frac{\nu}{\beta_{max} L^2} \tag{2.10}$$

where L is a characteristic length of the case under consideration, such as the inlet hydraulic diameter in duct problems. A typical value is $Da = 10^{-5}$. The parameter $\beta_{\max}$ should be set to a relatively large value, but not excessively so, as abnormally high values can cause numerical instabilities. A typical choice is $\beta_{\max} = 2500$.
A number of $I(\beta)$ functions have been proposed in the literature including those proposed by Borrvall and Petersson [40] and the Solid Isotropic Material with Penalization (SIMP).

$$I_{SIMP}(\beta) = \beta^b \tag{2.11}$$

$$I_{B-P}(\beta) = \frac{\beta}{1 + b(1-\beta)} \tag{2.12}$$

where b is a parameter controlling the steepness of the interpolation function. Larger b values correspond to sharper distinctions between the fluid and solid domains. However, larger b values also lead to stiffer optimization problems. Typical choices for b range from 1 to 10.

Regularization and Projection

In a number of TopO problems, especially those related to CHT, checkerboard artifacts may appear in the α field. To avoid these artifacts and mitigate the effects of local grid size to the optimized solution, the so-called regularization of the porosity field can be performed. A typical regularization technique involves a Helmholtz-type filter, i.e,

$$-r^2 \frac{\partial^2 \tilde{\alpha}}{\partial^2 x_j^2} + \tilde{\alpha} = \alpha \tag{2.13}$$

where $\tilde{\alpha}$ is the regularized porosity field and r can be seen as a smoothing radius, usually computed as a function of the average grid cell size. Regularization, as any other smoothing technique, unavoidably blurs the line between the fluid and solidified domains. To increase the contrast of the $\tilde{\alpha}$ field, projection can follow the regularization step, calculating the β field which appears in the source terms in the augmented conservation equations. Regulated β field is calculated typically by equation (2.15).

$$\beta = \frac{tanh(0.5b) + tanh[b(\tilde{\alpha} - 0.5)]}{2tanh(0.5b)} \tag{2.14}$$

where b is another sharpening parameter.

If no regularization or projection is applied, then $\beta = \alpha$ in the primal equations. In Figure 2.1, the impact of the predescribed steps are shown for a 2D TopO case with one inlet (left) and two outlets (down and right).

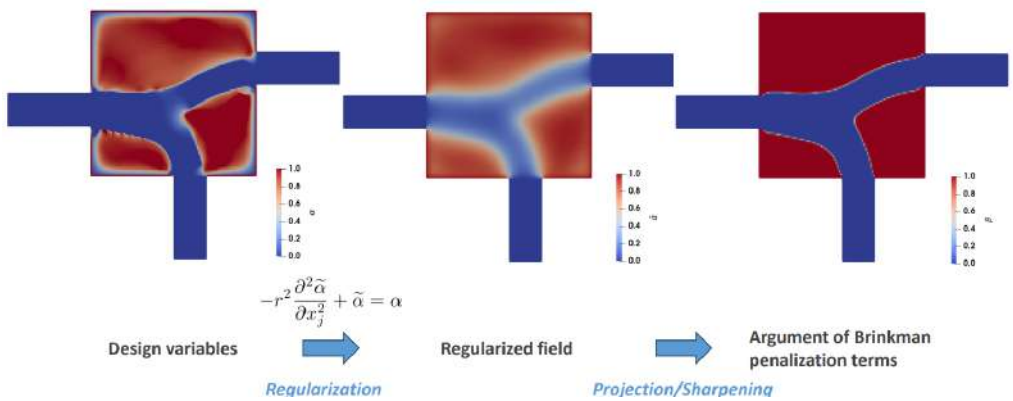

Figure 2.1: The left figure illustrates the initial porosity field, where transition regions contain intermediate porosity values around 0.5, indicating a mixture of fluid and solid characteristics. In the middle figure, the regularization step smooths these transition areas, ensuring a more gradual variation of porosity. Finally, the right figure presents the result after the projection step, where the porosity field is quite sharp defined with distinct 0 (solid) and 1 (fluid) regions, effectively eliminating intermediate values and ensuring a clear material distribution.

2.1.3 Primal Problem in CHT TopO

With the addition of the Brinkman-augmented energy equation, the CHT TopO [11] primal set of equations are:

$$\text{Continuity:} \quad R_p = \frac{\partial u_i}{\partial x_i} = 0, \qquad i = 1, 2(, 3) \tag{2.15}$$

$$\text{Momentum:} \quad R_{u,i} = u_j \frac{\partial u_i}{\partial x_j} + \frac{\partial p}{\partial x_i} - \frac{\partial \tau_{ij}}{\partial x_j} + \beta_{max} I^u(\beta) u_i = 0 \tag{2.16}$$

$$\text{Turbulence:} \quad R_{\tilde{\nu}} = v_j \frac{\partial \tilde{\nu}}{\partial x_j} - \frac{\partial}{\partial x_j}\left[\left(\nu + \frac{\tilde{\nu}}{\sigma}\right)\frac{\partial \tilde{\nu}}{\partial x_j}\right] - \frac{c_{b2}}{\sigma}\left(\frac{\partial \tilde{\nu}}{\partial x_j}\right)^2 \tag{2.17}$$

$$- \tilde{\nu} P(\tilde{\nu}) + \tilde{\nu} D(\tilde{\nu}) + \beta_{\max} I_{\tilde{\nu}}(\beta)\tilde{\nu} = 0 \tag{2.18}$$

$$\text{Eikonal:} \quad R_\Delta = \frac{\partial}{\partial x_j}\left(\frac{\partial \Delta}{\partial x_j}\Delta\right) - \Delta \frac{\partial^2 \Delta}{\partial x_j^2} - 1 + \beta_{\max} I_\Delta(\beta)\Delta = 0 \tag{2.19}$$

$$\text{Energy:} \quad R_T = (1-\beta)\rho C_p \frac{\partial (u_j\, T)}{\partial x_j} - \frac{\partial}{\partial x_j}\left(k I^k(\beta)\frac{\partial T}{\partial x_j}\right) = 0 \tag{2.20}$$

where T is the temperature field, ρ the constant fluid density, C_p the specific heat transfer coefficient under constant pressure and k the thermal conductivity. In the energy equation, the convection term is multiplied with $(1-\beta)$ to cancel out the inevitable small-scale leakage of fluid into the solid domain, almost always observed in TopO.

2.2 Adjoint Problem

2.2.1 Adjoint Problem in ShpO

After forming the augmented objective function adding the residual terms of equations 2.1-2.5, differentiating w.r.t the design variables, integrating by parts and setting the primal-fields-derivatives terms equal to zero, the adjoint equations for the ShpO [6] are formed:

$$R_q = -\frac{\partial u_j}{\partial x_j} = 0, \tag{2.21}$$

$$R_{u_i} = u_j \frac{\partial v_j}{\partial x_i} - \frac{\partial (v_j u_i)}{\partial x_j} - \frac{\partial \tau_{ij}^\alpha}{\partial x_j} + \frac{\partial q}{\partial x_i} + \tilde{\nu}_a \frac{\partial \tilde{\nu}}{\partial x_i} - \frac{\partial}{\partial x_l}\left(\frac{\tilde{\nu}_a \tilde{\nu}}{C_Y}\epsilon_{mjk}\frac{\partial v_k}{\partial x_j}\epsilon_{mli}\right) = 0, \quad i = 1, 2, (3)$$

$$R_{\tilde{\nu}_a} = -\frac{\partial (v_j \tilde{\nu}_a)}{\partial x_j} - \frac{\partial}{\partial x_j}\left[\left(\nu + \frac{\tilde{\nu}}{\sigma}\right)\frac{\partial \tilde{\nu}_a}{\partial x_j}\right] + \frac{1}{\sigma}\frac{\partial \tilde{\nu}_a}{\partial x_j}\frac{\partial \tilde{\nu}}{\partial x_j} + 2\frac{c_{b2}}{\sigma}\frac{\partial}{\partial x_j}\left(\tilde{\nu}_a \frac{\partial \tilde{\nu}}{\partial x_j}\right)$$

$$+ \tilde{\nu}_a \tilde{\nu} C_{\tilde{\nu}} + \frac{\partial \nu_t}{\partial \tilde{\nu}}\frac{\partial u_i}{\partial x_j}\left(\frac{\partial v_i}{\partial x_j} + \frac{\partial v_j}{\partial x_i}\right) + (-P + D)\tilde{\nu}_a = 0, \tag{2.22}$$

$$R_{\Delta_\alpha} = -2\frac{\partial}{\partial x_j}\left(\Delta_\alpha \frac{\partial \Delta}{\partial x_j}\right) + \tilde{\nu}\tilde{\nu}_a C_\Delta = 0, \tag{2.23}$$

where u_i are the adjoint velocity components, q the adjoint pressure, $\tilde{\nu}_a$ the adjoint to the turbulence model variable, $\tau_{ij}^\alpha = (\nu + \nu_t)\left(\frac{\partial u_i}{\partial x_j} + \frac{\partial u_j}{\partial x_i}\right)$ are the adjoint stresses.

2.2.2 Adjoint Problem in TopO

Following the continuous adjoint methodology for equations 2.6-2.11, the TopO adjoint equations [11] are derived:

$$R_q = -\frac{\partial u_j}{\partial x_j} = 0, \tag{2.24}$$

$$\begin{aligned} R_{u_i} = {} & u_j \frac{\partial v_j}{\partial x_i} - \frac{\partial (v_j u_i)}{\partial x_j} - \frac{\partial \tau_{ij}^{\alpha}}{\partial x_j} + \frac{\partial q}{\partial x_i} + \tilde{\nu}_a \frac{\partial \tilde{\nu}}{\partial x_i} - \frac{\partial}{\partial x_l}\left(\frac{\tilde{\nu}_a \tilde{\nu}}{C_Y}\epsilon_{mjk}\frac{\partial v_k}{\partial x_j}\epsilon_{mli}\right) \\ & + \rho c_p \left\{(1-\beta)T_a \frac{\partial}{\partial x_j}\left(\frac{\partial T}{\partial x_j}\right) - \frac{\partial}{\partial x_j}\left[(1-\beta)T_a \frac{\partial T}{\partial x_j}\right]\right\} + \beta_{\max} I_v(\beta) u_i = 0, \quad i = 1,2,(3) \end{aligned} \tag{2.25}$$

$$\begin{aligned} R_{\tilde{\nu}_a} = {} & -\frac{\partial (v_j \tilde{\nu}_a)}{\partial x_j} - \frac{\partial}{\partial x_j}\left[\left(\nu + \frac{\tilde{\nu}}{\sigma}\right)\frac{\partial \tilde{\nu}_a}{\partial x_j}\right] + \frac{1}{\sigma}\frac{\partial \tilde{\nu}_a}{\partial x_j}\frac{\partial \tilde{\nu}}{\partial x_j} + 2\frac{c_{b2}}{\sigma}\frac{\partial}{\partial x_j}\left(\tilde{\nu}_a \frac{\partial \tilde{\nu}}{\partial x_j}\right) \\ & + \tilde{\nu}_a \tilde{\nu} C_{\tilde{\nu}} + \frac{\partial \nu_t}{\partial \tilde{\nu}}\frac{\partial u_i}{\partial x_j}\left(\frac{\partial v_i}{\partial x_j} + \frac{\partial v_j}{\partial x_i}\right) + (-P + D)\tilde{\nu}_a + \beta_{\max} I_{\tilde{\nu}}(\beta)\tilde{\nu}_a = 0, \end{aligned} \tag{2.26}$$

$$R_{\Delta_\alpha} = -2\frac{\partial}{\partial x_j}\left(\Delta_\alpha \frac{\partial \Delta}{\partial x_j}\right) + \tilde{\nu}\tilde{\nu}_a C_\Delta + \beta_{\max} I_\Delta(\beta)\Delta_\alpha = 0 \tag{2.27}$$

2.2.3 Adjoint Problem in CHT TopO

Adding the energy-adjoint equation, the complete CHT TopO [11] adjoint problem is formulated:

$$R_q = -\frac{\partial u_j}{\partial x_j} = 0, \tag{2.28}$$

$$\begin{aligned} R_{u_i} = {} & u_j \frac{\partial v_j}{\partial x_i} - \frac{\partial (v_j u_i)}{\partial x_j} - \frac{\partial \tau_{ij}^{\alpha}}{\partial x_j} + \frac{\partial q}{\partial x_i} + \tilde{\nu}_a \frac{\partial \tilde{\nu}}{\partial x_i} - \frac{\partial}{\partial x_l}\left(\frac{\tilde{\nu}_a \tilde{\nu}}{C_Y}\epsilon_{mjk}\frac{\partial v_k}{\partial x_j}\epsilon_{mli}\right) \\ & + \rho c_p \left\{(1-\beta)T_a \frac{\partial}{\partial x_j}\left(\frac{\partial T}{\partial x_j}\right) - \frac{\partial}{\partial x_j}\left[(1-\beta)T_a \frac{\partial T}{\partial x_j}\right]\right\} + \beta_{\max} I_v(\beta) u_i = 0, \quad i = 1,2,(3) \end{aligned} \tag{2.29}$$

$$\begin{aligned} R_{\tilde{\nu}_a} = {} & -\frac{\partial (v_j \tilde{\nu}_a)}{\partial x_j} - \frac{\partial}{\partial x_j}\left[\left(\nu + \frac{\tilde{\nu}}{\sigma}\right)\frac{\partial \tilde{\nu}_a}{\partial x_j}\right] + \frac{1}{\sigma}\frac{\partial \tilde{\nu}_a}{\partial x_j}\frac{\partial \tilde{\nu}}{\partial x_j} + 2\frac{c_{b2}}{\sigma}\frac{\partial}{\partial x_j}\left(\tilde{\nu}_a \frac{\partial \tilde{\nu}}{\partial x_j}\right) \\ & + \tilde{\nu}_a \tilde{\nu} C_{\tilde{\nu}} + \frac{\partial \nu_t}{\partial \tilde{\nu}}\frac{\partial u_i}{\partial x_j}\left(\frac{\partial v_i}{\partial x_j} + \frac{\partial v_j}{\partial x_i}\right) + (-P + D)\tilde{\nu}_a + \beta_{\max} I_{\tilde{\nu}}(\beta)\tilde{\nu}_a = 0, \end{aligned} \tag{2.30}$$

$$R_{\Delta_\alpha} = -2\frac{\partial}{\partial x_j}\left(\Delta_\alpha \frac{\partial \Delta}{\partial x_j}\right) + \tilde{\nu}\tilde{\nu}_a C_\Delta + \beta_{\max} I_\Delta(\beta)\Delta_\alpha = 0, \tag{2.31}$$

$$R_{T_\alpha} = -\rho c_p \frac{\partial}{\partial x_j}\left[(1-\beta)v_j T_a\right] - \frac{\partial}{\partial x_j}\left[k(I_k(\beta))\frac{\partial T_a}{\partial x_j}\right] = 0 \tag{2.32}$$

where T_α is the adjoint temperature field.

2.3 Primal-Adjoint Optimization Algorithm

The optimization algorithm using the SQP method for the update of the design variables, utilized in the TopO and ShpO cases in this diploma thesis is shown below. More information about the SQP sub-routine is provided in the next section.

Algorithm 1 Primal-Adjoint Optimization Algorithm

```
design variables initialization
while convergence criteria are not met do
    Primal step - solve the primal equations
    Adjoint step - solve the adjoint equations and compute sensitivity derivatives
    Update step - solve quadratic sub-problem and update the design variables
end while
```

Chapter 3

Sequential Quadratic Programming

In this chapter, the main mathematical framework of the SQP algorithm is presented. This is based on solving approximations to the initial constrained optimization problem, and updating the design variables till the selected convergence criteria are satisfied. The approximated problem is constructed using the sensitivity derivatives of the objective and constraint functions, evaluated using the continuous adjoint method mentioned in the previous chapter.

To handle infeasible initiation of the design variables, the constraints are relaxed using a set of auxiliary design variables in a similar fashion, described in [40]. As the SQP algorithm drives the solution towards the feasible domain these pseudo design variables dissipate, bearing no influence on the final solution. These design variables are added in the initial objective function, multiplied by a scalar, which plays an important role in the convergence of the algorithm. Steering this factor's value to achieve best performance of the SQP algorithm in TopO and ShpO problems is the main concern of this diploma thesis. At the end of this chapter, the results of a certain TopO case are presented, showcasing the influence of this factor's value in resulting geometries.

3.1 Relaxation of Constraints By Introducing Extra Design Variables

The problems solved in this thesis include constraints related to demanding flow characteristics, such as maximum value for the total pressure drop between inlet and, outlets and in TopO cases, constraints inflicting direct bounds to the design variables. In this thesis, to differentiate between them, the bound constraints on the design variables are referred to as *bounds*, while other constraints are termed *constraints, flow constraints, or geometry con-*

straints, depending on their physical interpretation. Additionally, all equality constraints are converted into inequalities by squaring their original form. With this in mind, the typical structure of a problem addressed in this thesis is:

$$\begin{aligned} &\min_{x \in \Re^n} \; f(x) \\ &\text{s.t.} \quad g_i(x) \leq 0, \qquad i = 1, \ldots, m \quad (\textit{inequality constraints}) \\ &\qquad\; l \leq x_i \leq u, \qquad i = 1, \ldots, n \quad (\textit{bounds}) \end{aligned} \tag{3.1}$$

where: n is the size of the design variables and the bounds, m is the number of imposed constraints g_i.

To showcase the structure of SQP method, its framework will be presented for a simpler problem (3.2) with a single inequality constraint:

$$\begin{aligned} &\min_{x \in \Re^n} \; f(x) \\ &\text{s.t.} \quad g(x) \leq 0 \end{aligned} \tag{3.2}$$

The Quadratic Problem (QP) is formulated using a quadratic expansion for the objective f and a linear expansion for the constraint g, using sensitivity derivatives of f and g evaluated at the current cycle k, with design variables x_k. This results in the following optimization problem (3.3):

$$\begin{aligned} \min_{p_x \in \Re^n} \tilde{f}(p_x) \;&=\; f_k + \nabla f_k^T p_x + \frac{1}{2} p_x^T H_k p_x \\ \text{s.t. } \tilde{g}(p_x) \;&=\; g_k + \nabla g_k^T p_x \;\leq 0 \end{aligned} \tag{3.3}$$

where H_k is the Hessian matrix of f, approximated using a method such as BFGS at x_k, and p_x represents the step from x_k. Terms g_k, ∇f_k, and ∇g_k correspond to the values of the constraint function and the gradients of the objective and constraint functions, respectively, all evaluated at x_k.

In CFD optimization, the initialization of the design variables x in the QP may not satisfy the problem's constraints, causing the algorithm to fail from the start. Constraints that are not satisfied are referred to as infeasible constraints. In this thesis, infeasibility always refers to the quadratic problem, not the original problem, unless explicitly stated otherwise. Infeasibility appears often in TopO at the initial cycle due to the volume-related constraint. Its linear approximation cannot be satisfied in the initial cycles due to the projection procedure's application on the porosity field. More specifically, projection implies a flattening effect on the objective's quadratic approximation except for the fluid-solid transition region. This ef-

fect limits the ability of the porosity field to change across the entire fluid and solid domain, except near the interface of the two phases. As a result, the design variables cannot change significantly enough to satisfy the linear approximation to the volume constraint, leading to infeasibility.

Other constraints can also be infeasible and, either, like the lift constraint in ShpO airfoil case presented in the sections 5.1 and 5.2. In all cases, the goal remains to find a feasible solution or, a solution that suppresses constraint violations, in cases where a constraint in the initial optimization problem (not its linear approximation) can not be satisfied (i.e TU Berlin TurboLab Stator Blade case in chapter 5.3).

To overcome these issues, the linearized constraint g is relaxed by introducing a non-negative auxiliary variable y, which is incorporated into the function to be minimized, multiplied with a weighting factor c, which leads to the following constrained minimization problem:

$$\begin{aligned} \min_{p_x \in \Re^n,\ y \in \Re} \ & \tilde{f}(p_x) + cy \\ \text{s.t. } & \tilde{g}(p_x) - y \leq 0 \\ & -y \leq 0 \end{aligned} \tag{3.4}$$

In the new problem, there always exists a positive y value that satisfies the modified constraint, even if $\tilde{g}(p_x)$ is infeasible, meaning $\tilde{g}(p_x) > 0$. Naturally, if the QP (3.3) becomes feasible, the additional variable y will be set to zero, acquiring a nonzero value only when the design variables do not satisfy $\tilde{g}$. Consequently, the optimization algorithm shifts its focus from solely minimizing the original objective function f to also reducing y, thereby adjusting the design variables x to restore feasibility.

The weight factor c controls the influence of constraints on the new function to be minimized. Higher values of c force the algorithm to steer the design variables more aggressively toward the feasible domain, ensuring faster constraint satisfaction. However, this comes with the risk of converging to regions with high f values. Conversely, lower values of c allow the design variables to explore better regions in terms of f but may delay constraint satisfaction. While c is typically kept constant, in some cases, it may be beneficial to vary its value with each iteration. Varying values of c, across optimization cycles can lead the SQP algorithm to different final solutions, as demonstrated in the following chapters.

3.2 Optimality Conditions for QP Sub-Problem

To acquire the KKT optimality conditions for the QP sub-problem (3.4), this is simplified by introducing the positive slack variable g_s in linearized, y-augmented constrained, turning it into an equality constraint.

$$\begin{aligned} \min_{p_x \in \Re^n,\ y \in \Re} \ & \tilde{f}(p_x) + cy \\ \text{s.t. } & \tilde{g}(p_x) - y + g_s = 0 \\ & g_s \geq 0 \\ & y \geq 0 \end{aligned} \tag{3.5}$$

The two remaining, simpler inequality constraints are eliminated by being incorporated in the logarithmic barrier terms, added in the objective, transforming problem (3.5) into equality-constrained problem (3.6):

$$\begin{aligned} \min_{p_x \in \Re^n,\ y \in \Re,\ g_s \in \Re} \ & \tilde{f}(p_x) + cy - \epsilon \cdot log(y) - \epsilon \cdot log(g_s) \\ \text{s.t. } & G(p_x, y, g_s) = \tilde{g}(p_x) - y + g_s = 0 \end{aligned} \tag{3.6}$$

where ϵ a positive scalar, refered to as the barrier parameter.
It is noted that as g_s and y approach zero (from positive values, i.e from feasible space), the negative barrier terms goes to infinity. This obviously penalizes the objective and forces the algorithm to keep g_s positive. In each optimization cycle, a sequence of (3.6) sub-problems is being solved for a decreasing set of barrier parameters ϵ.

The Lagrangian of problem (3.6) is defined as:

$$L(p_x, y, \lambda, g_s) = \tilde{f}(p_x) + cy - \epsilon log(y) - \epsilon log(g_s) - \lambda G(p_x, y, g_s) \tag{3.7}$$

where λ is the non-negative Lagrange multiplier of equality constraint in problem (3.6).
The stationarity of the Lagrangian w.r.t p_x, y, λ, g_s, provide the KKT conditions for sub-problem (3.6), as follows:

$$\begin{aligned} & F_{L,x}(p_x, y, \lambda, \mu, g_s) = \nabla \tilde{f} - \lambda \nabla \tilde{g} = H_k p_k + \lambda \nabla g_k = 0 \\ & F_{L,y}(p_x, y, \lambda, \mu, g_s) = cy - \lambda y - \epsilon = 0 \\ & F_{\lambda}(p_x, y, \lambda, \mu, g_s) = \tilde{g}(p_x) - y + g_s = g_k + \nabla g_k p_k + gs - y = 0 \\ & F_{g_s}(p_x, y, \lambda, \mu, g_s) = \lambda g_s + \epsilon = 0 \end{aligned} \tag{3.8}$$

Solution $(p'_x, y', \lambda', g'_s)$ to problem (3.8) is:

$$\begin{aligned} p'_x =& p_x + \delta p_x \\ y' =& y + \delta y \\ \lambda' =& \lambda + \delta\lambda \\ g'_s =& g_s + \delta g_s \end{aligned} \tag{3.9}$$

where the corrections are computed by solving the linear system:

$$\begin{pmatrix} H_k & 0 & \nabla g_k^T & 0 \\ 0 & c+\lambda & y & -1 \\ \nabla g_k^T & -1 & 0 & 1 \\ 0 & 0 & g_s & \lambda \end{pmatrix} \begin{pmatrix} \delta p_x \\ \delta y \\ \delta\lambda \\ \delta g_s \end{pmatrix} = - \begin{pmatrix} F_{L,x} \\ F_{L,y} \\ F_\lambda \\ F_{g_s} \end{pmatrix} \tag{3.10}$$

System (3.10) is being solved iteratively by progressive decreasing values of ϵ, until a required small value is achieved. After that, the new optimization cycle will start.

The solution diagram of the optimization problem in each step is presented in Algorithm 2:

Algorithm 2 SQP Algorithm

```
Solve the primal and adjoint problem and compute the sensitivity derivatives and the
  Hessian matrix
Initialize ϵ
while convergence criteria are not satisfied do
    Solve KKT and compute the update direction for the design variables
    Perform line search and update design variables
    Decrease ϵ
end while
Begin next optimization cycle
```

3.3 Extra Design Variables Multiplier's Influence In SQP Solution

Before continuing, it must be specified that a feasible initialization in TopO may provide faster convergence, but in many cases the achieved solution may not be the best achieved. Additionally, even with a feasible initialization, the design variables can also move into the infeasible region afterwards. The fact that the quality of the initialization in many TopO cases is not known beforehand, renders an infeasibility-handling-technique mandatory, when

an SQP algorithm is used.

The multiplier of the extra design variables, c (see objective in problem (3.5)), scales the influence of constraint in-satisfaction on the augmented objective and plays a significant role in the convergence of a constrained optimization problem. Pure c tuning, may lead in slower convergence or even impractical solutions in some 2D TopO cases, as in figure 3.1. This figures presents the results of a TopO case, which cannot be solved with a standard SQP algorithm, using a uniform fluid initialization, $a = 0$. The objective is the minimization of the total pressure losses from the left inlet to the right and bottom outlets, satisfying a volume-occupied-by-fluid constraint less than 46.2% of the computational domain.

For instance, setting $c = 100$, as proposed in [41], forces the SQP algorithm to satisfy the volume constraint aggressively, leading to the closure of the right outlet and the formation of a sealed fluid chamber, rendering the solution impractical. This demonstrates that, although the resulting solution was feasible, it was non the less unacceptable.

On the other hand, a weaker constraint term in the objective function—achieved by setting $c = 1$ or $c = 5$—guides the SQP algorithm towards acceptable results.

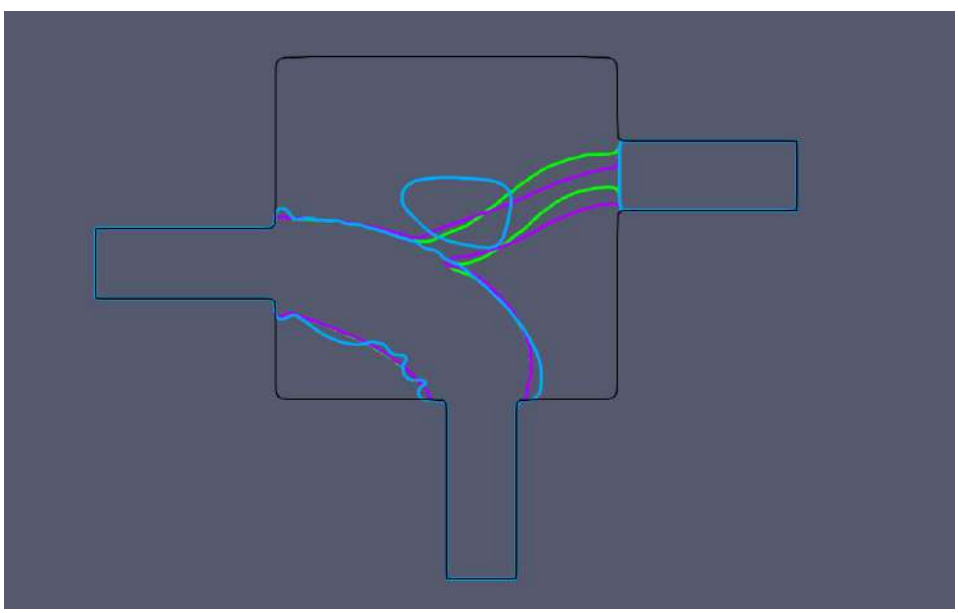

Figure 3.1: 2D TopO case in which three different runs have been conducted for factor's values, c = 1 (green), c = 5 (purple), c = 100 (blue).

In 3D TopO and ShpO cases, inappropriate choice of its value can also lead in the SQP algo-

rithm divergence.

Accounting for the influence of factor c values, the main focus of this diploma thesis is to seek the most appropriate factoring of the constraint term in the augmented objective used in the proposed SQP framework, for 2D, 3D, TopO and ShpO problems. In this attempt, constant and varying values of c have been tested, with the latest showing (in many cases) improved results as demonstrated in the following chapters.

Chapter 4

Overcoming SQP Issues - Demonstrations in TopO

To determine the influence of the weighted, extra design variables in the augmented function in TopO, a number of 2D and 3D benchmarks is evaluated. Each case is being solved with the same setup, for different settings of weight c. Constant and varying values are examined, to detect the best-suited setup.

The objectives to be minimized and constraints used in the following cases are the inlet-to-outlets total pressure losses, the outlet uniformity index, the flow rate partition across all outlets and the fluid occupied volume:

Fluid Occupied Volume

$$J = \left(\frac{\int_\Omega (1-\beta)\, d\Omega}{\int_\Omega d\Omega} - \pi_{\text{tar}} \right) \frac{1}{\pi_{\text{tar}}}$$

This quantifies the difference between the fluid volume and a target value π_{tar}, normalized by the latter.

Total Pressure Losses

$$J = -\int_{S_I, S_O} \left(p + \frac{1}{2} v_k^2 \right) v_i n_i \, dS$$

where S_I and S_O are the inlet and outlet patches, respectively.

Flow Rate Partition

$$J = \frac{1}{2} \sum_{l=1}^{L} \left(t_l - \frac{\int_{S_{Ol}} v_i n_i \, dS}{m_I} \right)^2$$

$$m_I = -\int_{S_I} v_i n_i \, dS$$

This quantifies the distribution of the inlet flow rate m_I to specific outlets S_{Ol} with target percentages t_l.

Uniformity Index

$$J = \frac{1}{2} \frac{\int_S (v_i - \overline{v_i})^2 \, dS}{\int_S dS}$$

$$\overline{v_i} = \frac{\int_S v_i \, dS}{\int_S dS}$$

This index (to be minimized) quantified the variance of velocity v_i over an inlet or outlet patch S.

In the first section of this chapter the impact of the scaling factor c on the convergence behavior and solution quality in 2D and 3D topology optimization problems is examined. In the second section, the change of c across the optimization cycles is explored, aiming at improved convergence.

4.1 TopO Applications Using Constant Factor's Values

4.1.1 Case 1 - 2D

Case 1 consists of a laminar problem with 1 inlet and 2 outlets, with an inlet-height Reynolds number equal to, $Re = 200$. The objective function to be minimied is the total pressure losses between the inlet and the outlets, normalized by the initial value. The porosity field is initialized to 0 in every cell, i.e the entire volume is initially occupied by fluid. The only constraint is the fluid volume constraint lessthan 46.2% of the computational domain. The mesh, and consequently the design variable vector, consists of 13,000 cells. The boundary conditions used for the primal problem is presented in table (4.1).

Region	**U**	**p**
Inlet	(1,0)	zero gradient
Outlets	zero gradient	0
Domain Boundary	(0,0)	zero gradient

Table 4.1: Boundary Conditions of the primal problem in 2D laminar case 1, with 1 inlet and 2 outlets.

In Figure (4.1), the duct geometry for four cycles, including the final one, is shown for three

different runs of the case with $c = 1$, 5, and 100. The resulting velocity fields are presented in Figure (4.2). The objective and constraint values for 100 optimization cycles are presented in Figure (4.3).

As expected, the rate of constraint reduction is proportional to the value of c, which can be observed in Figure (4.3). This is further reflected on the positioning of the solid lines in Figure (4.2). Specifically, the 'purple' line, corresponding to $c = 100$, moves significantly faster than the other two, to enclose the constraint's maximum fluid volume percentage of 46.2%. The rate at which feasibility is achieved is so rapid that the path to the right outlet becomes solidified, and this remains the case for the rest of the optimization cycle. The cycles of $c = 1$, 5 reach a solution with a total reduction of 26% of the objective.

4.1.2 Case 2 - 2D

Case 2 contains the same settings as Case 1 with the addition of a mass flow partition constraint with mass fragments 50% and 50% for the two outlets. The duct geometries for four cycles including the final one are presented in Figure (4.4). The resulting velocity fields are presented in Figure (4.5). The objective and constraint values for 100 optimization cycles are presented in Figure (4.6).

In contrast to Case 1, all runs in this case converge to the same solution, as shown both numerically in Figure (4.6) and geometrically in Figure (4.3). The total reduction in the objective is 8%, significantly smaller than in Case 1, due to the addition of the mass-flow-partition constraint. Similarly to Case 1, the run with $c = 100$ reaches the constraints more quickly, but this results in oscillations in the mass flow partition constraint. $c = 5$ run, fail to converge within 100 cycles in the same solution and oscillations are observed as well. Setting $c = 1$, lead the SQP algorithm into faster convergence without oscillations in the mass-flow-partition constraint values.

In both 2D TopO cases, setting $c = 1$ shows best convergence qualities, in comparison to the other two used values.

4.1.3 Case 3 - 3D

In case 3, a 3D laminar problem is being solved with 1 inlet and 2 outlets, with an inlet-height Reynolds number, $Re = 800$. The objective function used is the flow uniformity index

referring to the two exits, normalized by its initial value. The porosity field is initialized to 0 in every cell. There are 3 constraints in this problem: a total pressure losses target of 0.778, fluid volume less than 10% and exit mass fractions 50-50. The computational mesh, and consequently the design variable vector, consists of 221,644 elements. The boundary conditions used for the primal problem is presented in table (4.2).

Region	**U**	**p**
Inlet	$-10\vec{n}$	zero gradient
Outlets	zero gradient	0
Domain Boundary	(0,0,0)	zero gradient
Symmetry Wall	$\partial/\partial\vec{n} = 0$	$\partial/\partial\vec{n} = 0$

Table 4.2: Boundary Conditions of the primal fields in 3D symmetrical, laminar case 3, with 1 inlet and 2 outlets. $\vec{n}$ stands for the normal unit vector to the corresponding surface.

The duct geometries for three runs including the final one are presented in Figures (4.7) - (4.9). The objective and constraint values for 70 cycles are presented in Figure (4.11). All three cycles reach feasible solutions with the same objective reduction of 58%. As expected, constraint violation is being reduced proportionally with the value of c, as depicted in volume and mass-flow-partition constraint plots of Figure (4.12), but using different c in this cases does not affect the convergence substantially. The flow fields of the resulting ducts are shown in Figure (4.10).

In contrast to the previous 2D cases with the default value of $c = 100$, the cycle converges faster.

4.1.4 Case 4 - 3D

In case 4 a 3D problem is also targeted, 1 inlet and 3 outlets. The flow is turbulent, with an inlet-height Reynolds number, $Re = 50,000$. The function to be minimized is the flow uniformity index referring to the three exits, normalized by its initial value and the constraints are a total-pressure-losses target of 20, fluid volume less than 15% and exit-mass-flow fractions 33-33-33. The porosity field is initialized to 0.5 in every cell. The computational mesh, and consequently the design variable vector, consists of 109,960 elements.
For the inlet velocity, a constant value is used, calculated for a constant volumetric flow rate of 0.05 m^3/s. At the outlets, a mixed boundary condition is applied, setting a zero gradient for outflow and a value of 0 for inflow. A wall function is employed to calculate $\tilde{\nu}$ at the wall boundary cells. The boundary conditions for the primal fields are presented in Table (4.3).
In contrast to the previous test cases, only $c = 100$ produces a solution, as for $c = 2$ and $c = 5$ the adjoint problem corresponding to the objective fail to converge sufficiently in cycle 2. For

Region	U	p	$\tilde{\nu}$
Inlet	* (Dirichlet)	zero gradient	0.0001 (Dirichlet)
Outlets	* mixed	0 (Dirichlet)	zero gradient
Domain Boundary	(0,0,0) (Dirichlet)	zero gradient (Neumann)	-

Table 4.3: Boundary Conditions of the primal problem in 3D case 3. $\vec{n}$ stands for the normal unit vector of the corresponding surfaces.

$c = 100$, a sudden change is observed in duct geometry at cycle 32, which worsens the final solution.
The duct geometries for $c = 100$ at three cycles, including the 50th and final-one, are presented in Figures (4.12). The objective and constraint values for 50 cycles are presented in Figure (4.15). An 11% reduction in the objective is achieved in the first 32 cycles. The flow field of the solution geometry is presented in Figure (4.13).

The value of $c = 100$ appears to yield better results in 3D cases like Case 3 and Case 4 compared to the 2D cases.

4.2 TopO Applications Using Varying Factor's Values

To explore whether a varying value of c could potentially improve the results in Topology Optimization (TopO), the following additional runs were conducted.

For the 2D cases, where it is shown that smaller values of c (e.g., $c = 1$) produce better results, the value of c is varied piecewise linearly according to the columns in Table (4.4). In Sets 1, 2 and 3c has an initial value of $c = 1$ or $c = 0.1$ and is gradually being increased, while in Set 4, it is being decreased to zero. In all sets, c is initially held at a tested optimal value for the first half or third of the optimization loop, after which it is being changed intensely either increasing or decreasing, to determine which strategy yields better results.

Cycle	1	2	3
1	1	0.1	1
30	5	1	0.5
60	5	2	0.2
80	20	5	0.1
100	50	50	0

Table 4.4: Varying values of c for 2D cases 1 and 2.

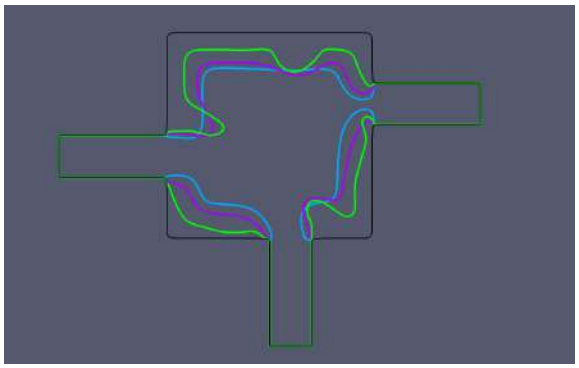

(a) t = 20

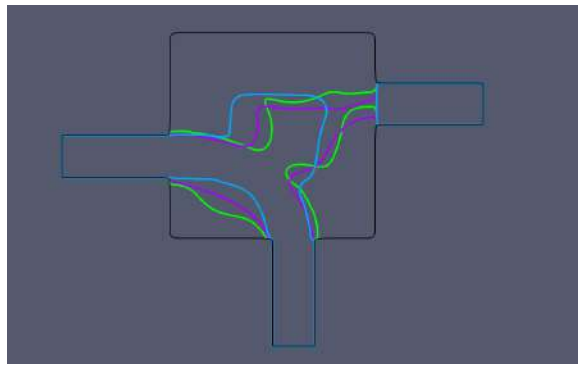

(b) t = 40

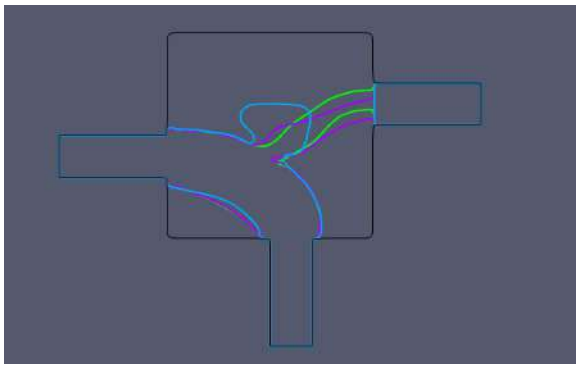

(c) t = 70

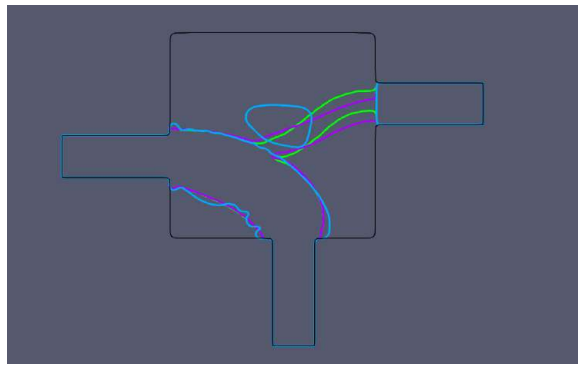

(d) t = 100

Figure 4.1: Evolving geometry of the duct in Case 1 for cycles 20, 40, 70, 100. The initial all-fluid domain is shown in black, the 'c = 1' geometry in green the 'c = 5' geometry in purple and the 'c = 100' geometry in blue.

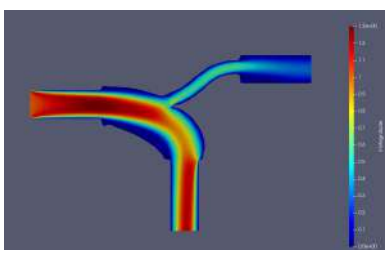

(a) c = 1

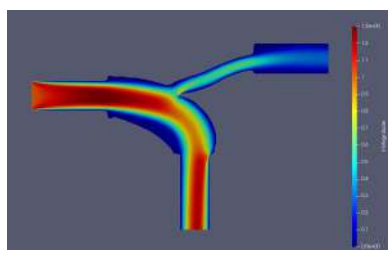

(b) c = 5

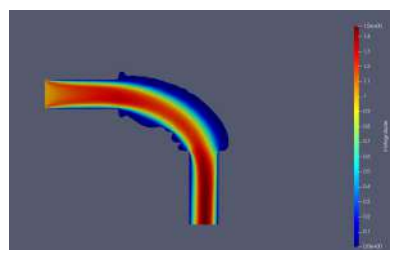

(c) c = 100

Figure 4.2: Case 1 resulting velocity magnitude fields for $c = 1$, 5, 100.

For the 3D cases the value of c is being increased and decreased linearly and quadratically with a total variance of 100 and an initial value equal to the default, $c = 100$, which has already been shown to produce better results.

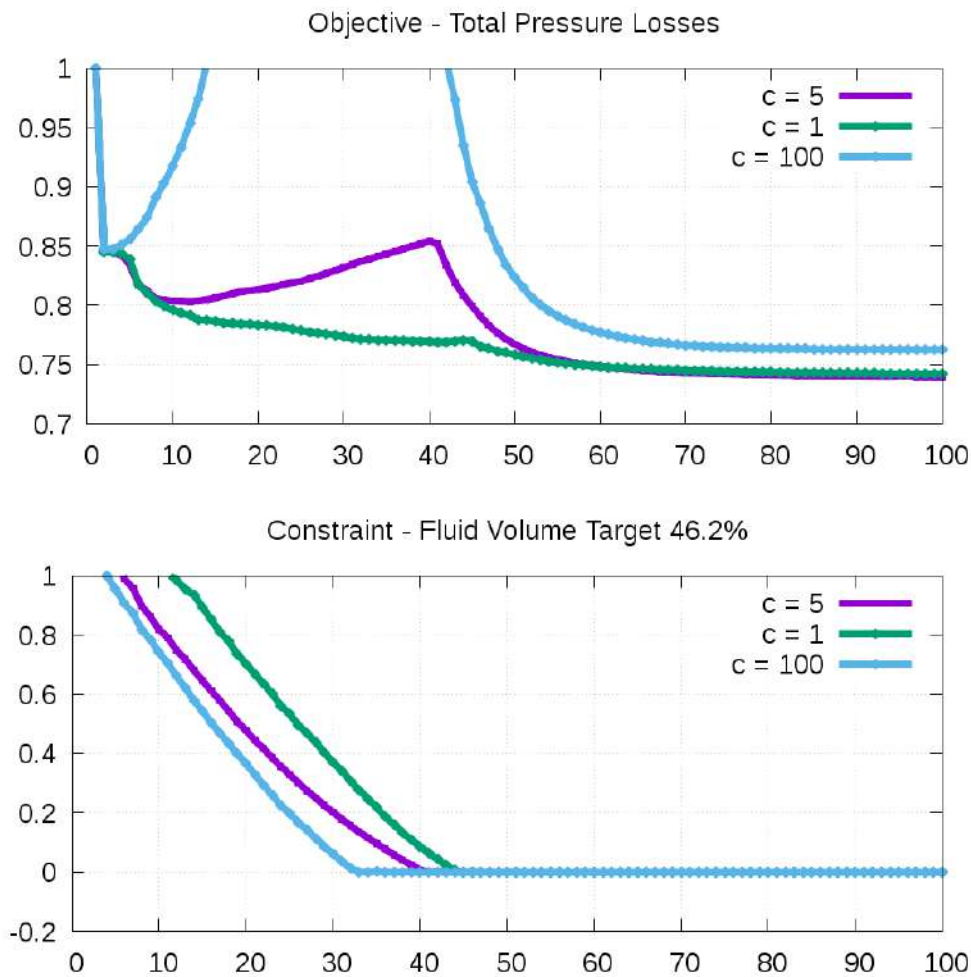

Figure 4.3: Objective - total pressure losses and constraint - TopO geometry for case 1 and c = 1, 5, 100.

4.2.1 Case 1 - 2D

For the 2D laminar case 1 with 1 inlet and 2 outlets, the results are presented in Figure (4.15). Similar objective and constraint convergence is being observed and in all runs same objective reduction is being reached. However initializing $c = 0.1$ and reducing its value accross the optimization loop, produces smoother objective reduction.

4.2.2 Case 2 - 2D

In case 3, as it is shown in Figure 4.16, increasing c according to column 1 and 2 of Table 4.4, drives the SQP algorithm to the same solution as in $c = 1$ run. Decreasing it however leads, without oscillations, to a new improved feasible solution with an objective value, J = 89.2 % in contrast to 92.7%. The resulting geometry with its corresponding flow field is presented in

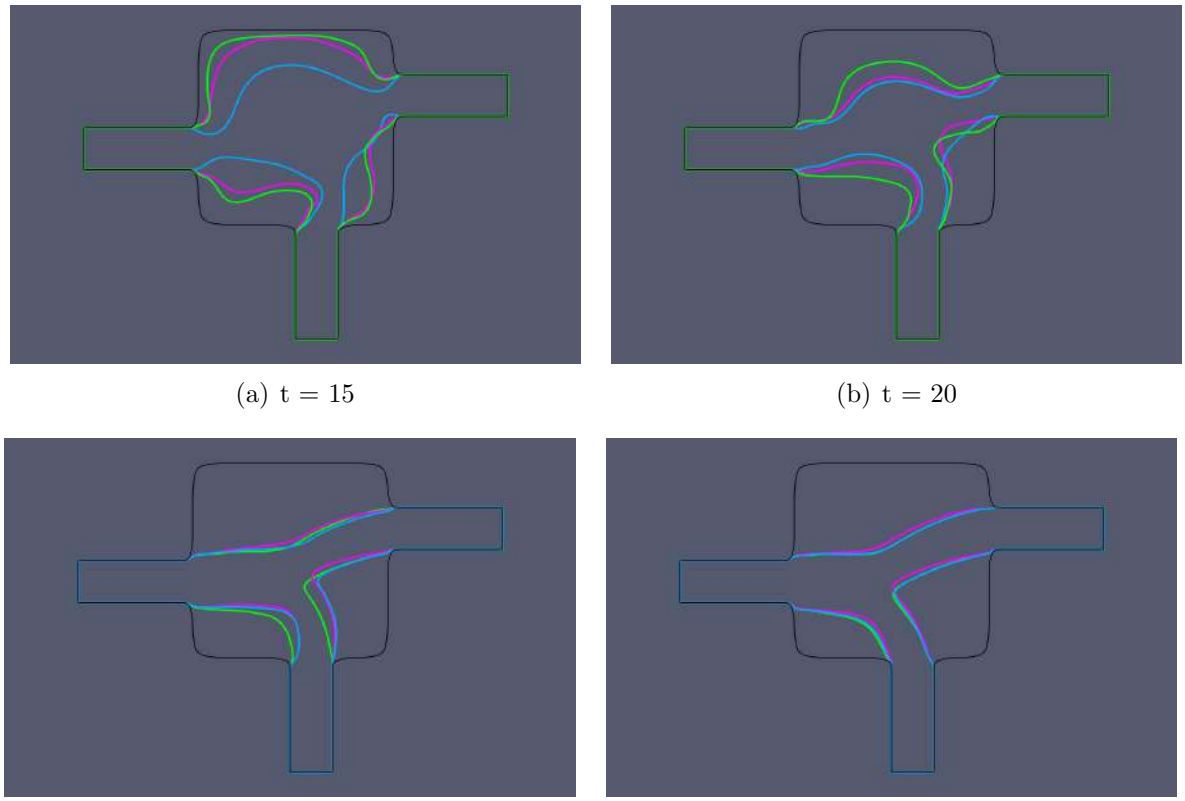

(a) t = 15 (b) t = 20

(c) t = 40 (d) t = 100

Figure 4.4: Evolving geometry of the duct in Case 2 for time-steps 15, 20, 40, 100. The initial all-fluid domain is shown in black, the 'c = 1' geometry in green the 'c = 5' geometry in purple and the 'c = 100' geometry in blue.

Figure (4.17).

In both 2D TopO cases, initializing $c = 1$ and reducing it across the optimization loop produces smoother convergence and deactivates gradually the $+cy$ term in the augmented objective (problem 3.4), allowing for greater objective reduction if possible.

4.2.3 Case 3 - 3D

The results of case 3 runs, using linearly and quadratically increased or decreased c are presented in Figure (4.18). No improvement of the final solution or in the convergence path is observed. A sudden change in design variables is depicted in the final cycle of run using quadratic decreasing c, caused by a partially converged adjoint problem corresponding to the objective.

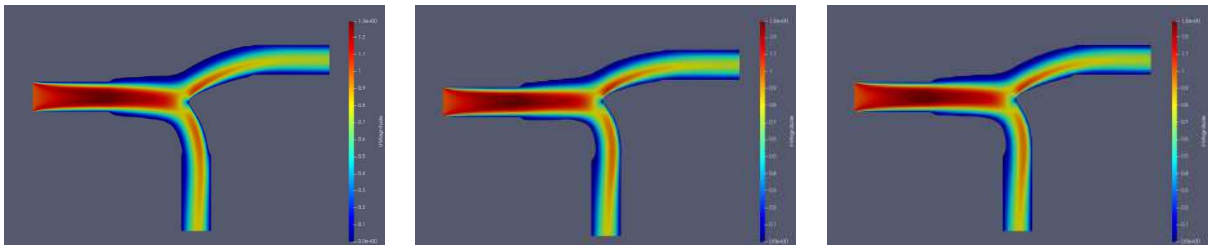

(a) c = 1 (b) c = 5 (c) c = 100

Figure 4.5: Case 2 resulting velocity magnitude fields for $c = 1$, 5, 100.

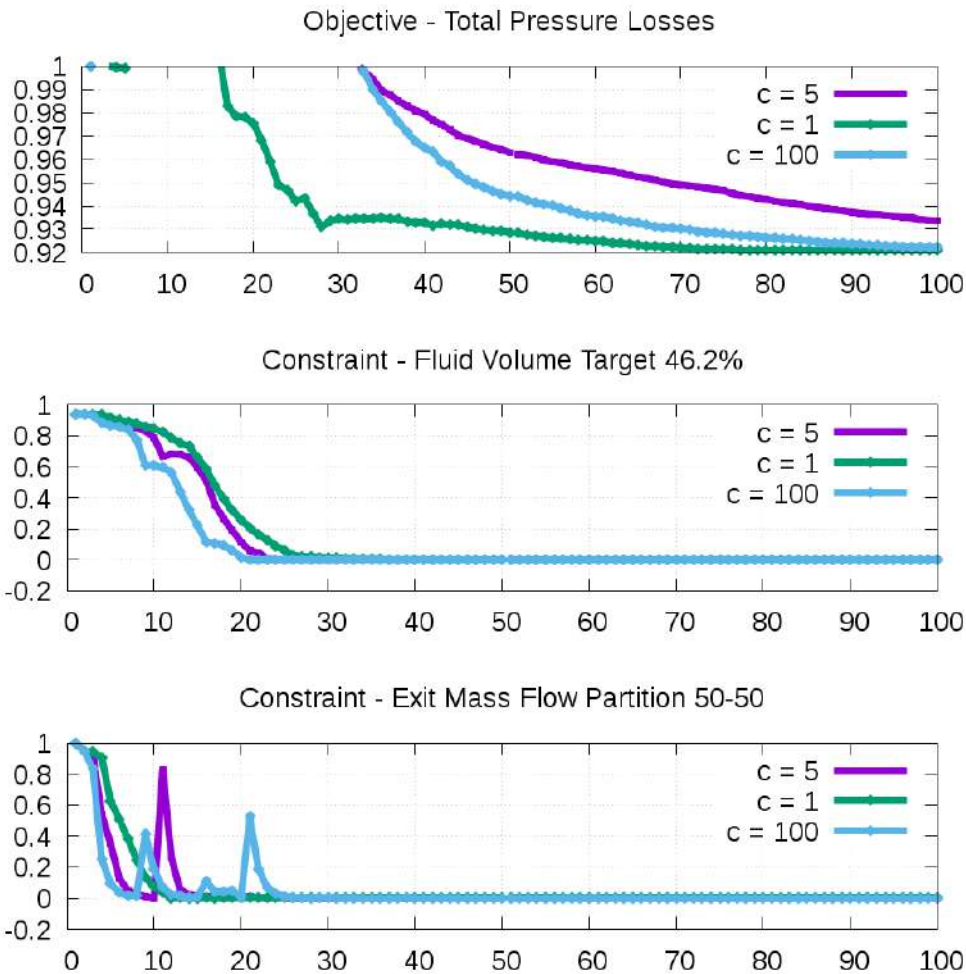

Figure 4.6: Objective - total pressure losses and constraints - TopO geometry and mass flow partition for case 2 and c = 1, 5, 100.

4.2.4 Case 4 - 3D

For the 3D turbulent Case 3, with one inlet and three outlets, varying c across the optimization loop produces the results are presented in Figure (4.19). A sudden jump in the design

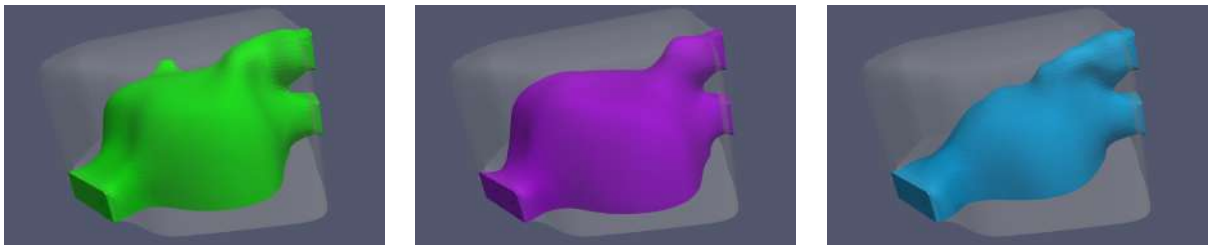

(a) c = 2 (b) c = 5 (c) c = 100

Figure 4.7: Cycle 15 duct geometries in Case 3 for c = 2, 5, 100.

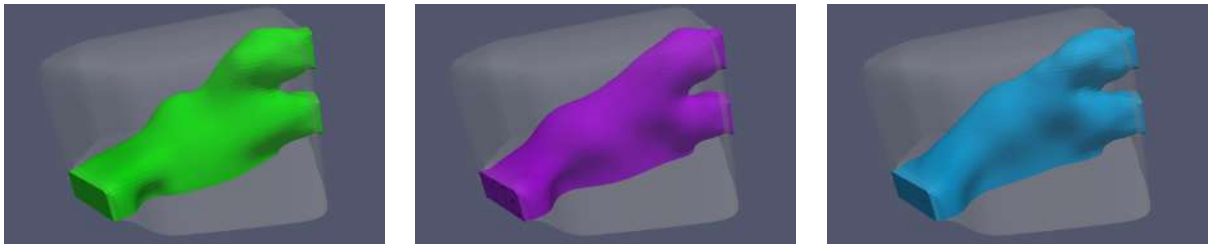

(a) c = 2 (b) c = 5 (c) c = 100

Figure 4.8: Cycle 30 duct geometries in Case 3 for c = 2, 5, 100.

variable occurs again at cycle 32 for linearly decreasing c, and at cycle 45 for the quadratically increasing c. Different feasible solutions were obtained for each run, with the best results achieved using linearly and quadratically decreasing values of c. The third decreasing-value run, however, did not reach cycle 50 due to convergence issues at cycle 46 in the mass flow rate adjoint fields. The resulting geometries and corresponding flow fields are shown in Figure (4.20).

Overall in TopO, decreasing values of c is a safer option, in contrast to keeping it constant, as it can steer the optimization algorithm towards better solutions. Moreover, in 2D cases initialization $c = 1$ shows the best results, whereas in 3D cases $c = 100$ is preferable.

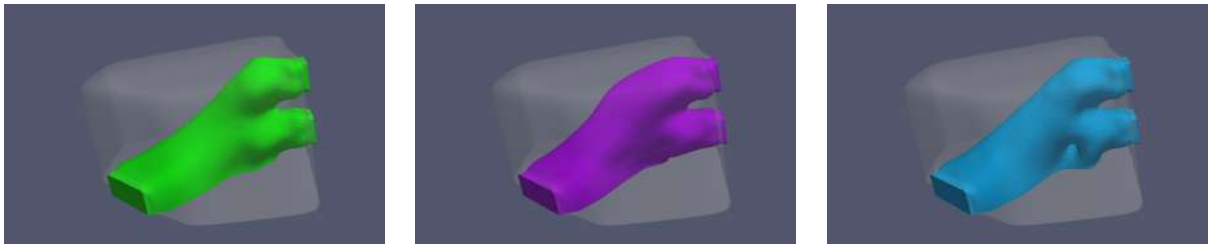

(a) c = 2 (b) c = 5 (c) c = 100

Figure 4.9: Cycle 70 duct geometries in Case 3 for c = 2, 5, 100.

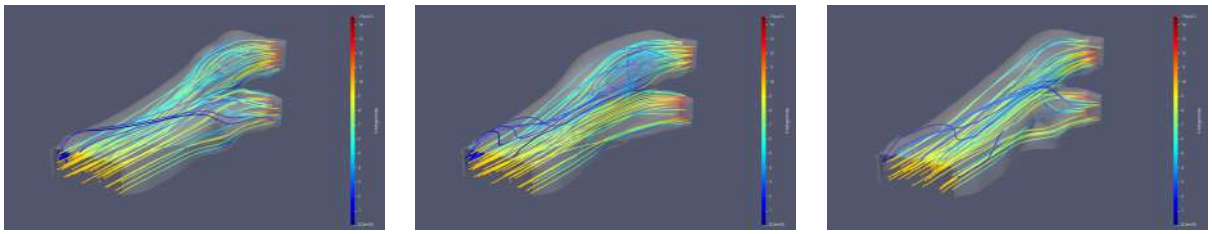

(a) c = 2 (b) c = 5 (c) c = 100

Figure 4.10: Streamlines of the generated geometries in case 3 for $c = 2$, 5, 100.

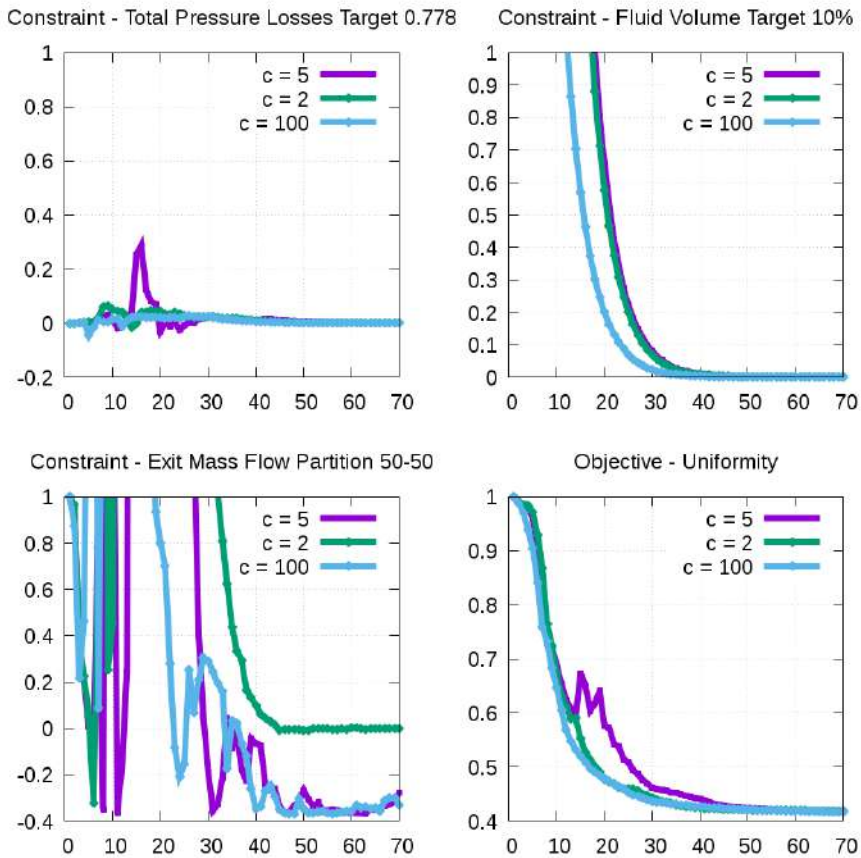

Figure 4.11: Objective - uniformity at the outlets and constraints TopO volume, outlet mass flow partition, total pressure losses for case 3 and c = 2, 5, 100.

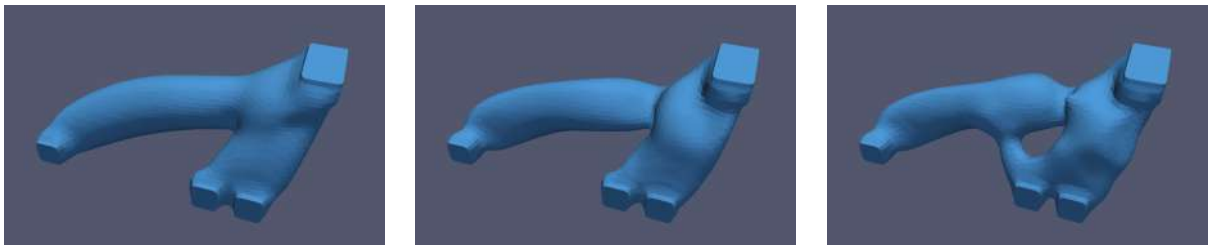

(a) t = 10 (b) t = 32 (c) t = 50

Figure 4.12: Geometry of the ducts in Case 4 for c = 100.

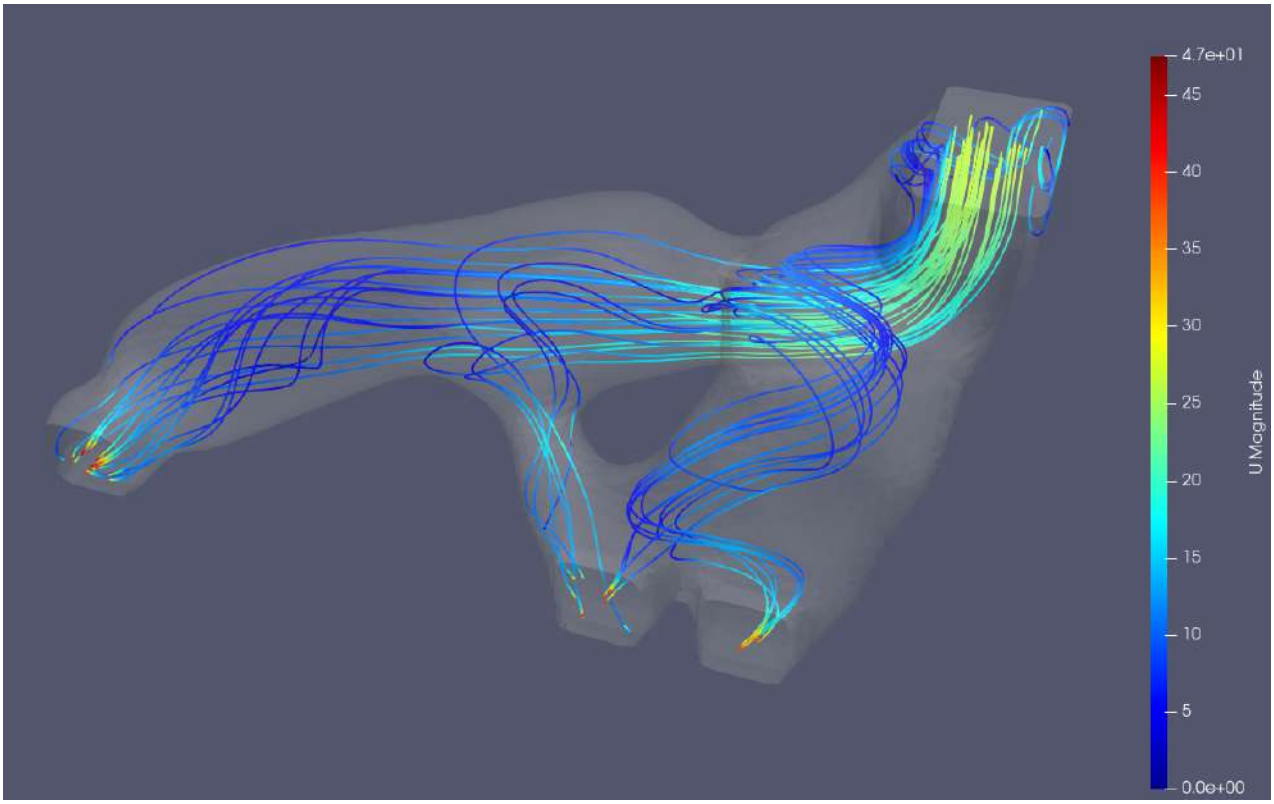

Figure 4.13: Streamlines of duct in Case 4 for c = 100.

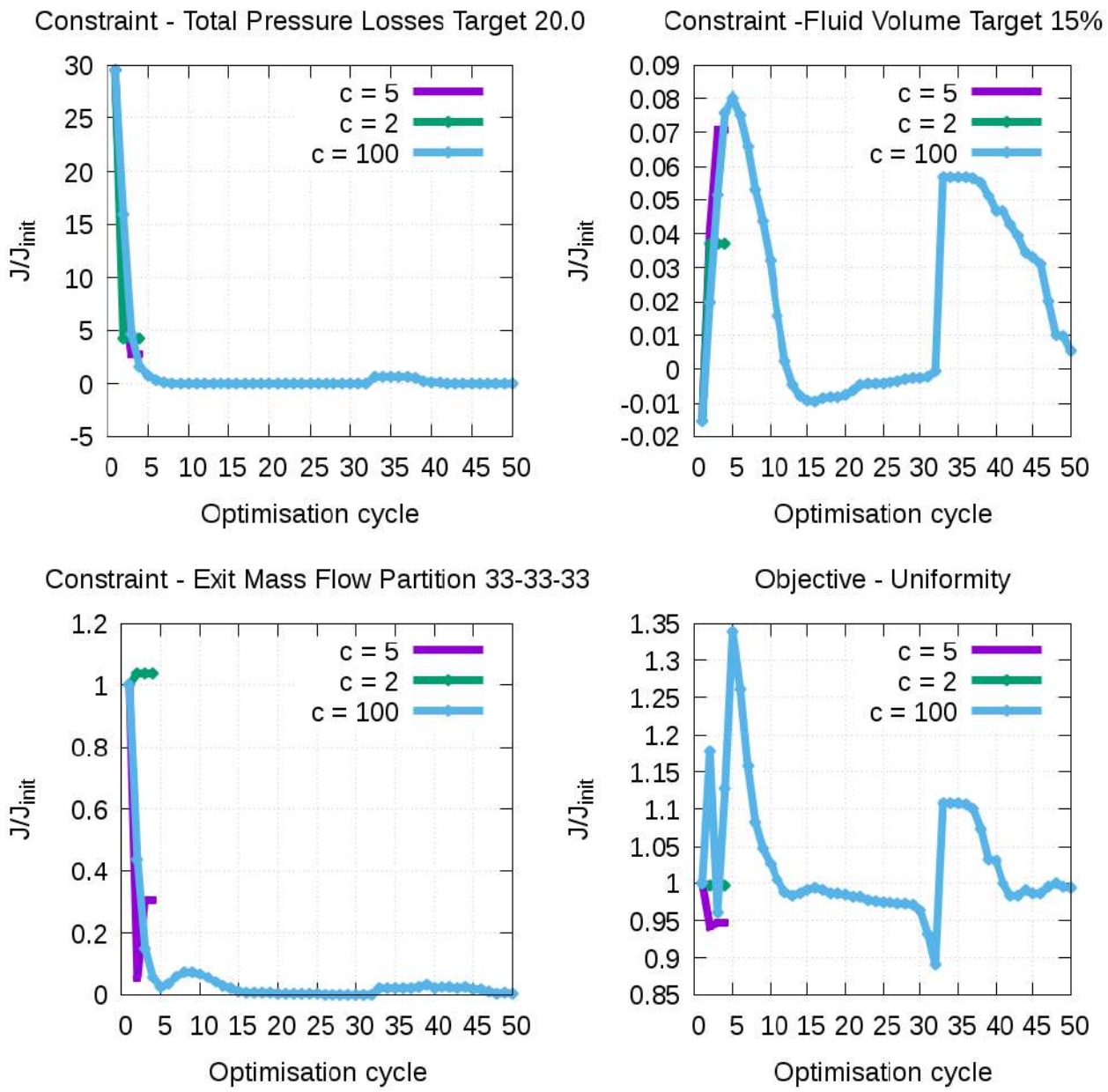

Figure 4.14: Objective - uniformity at the outlets and constraints TopO volume, outlet mass flow partition, total pressure losses for case 4 and c = 2, 5, 100.

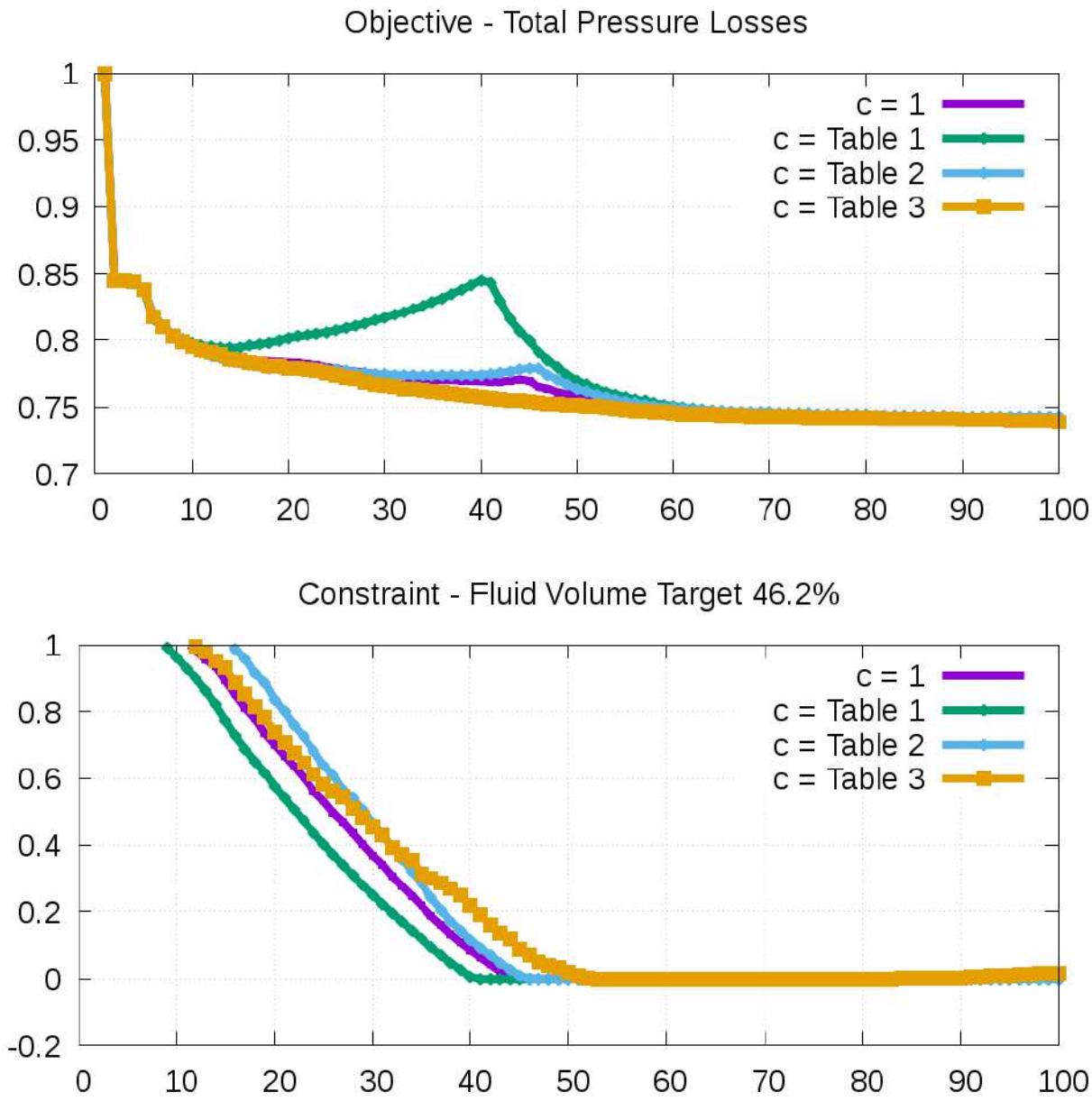

Figure 4.15: Objective-total pressure losses and constraint-TopO geometry for case 1 and c keeping a constant value of 1 and varying according to table 1, 2, 3.

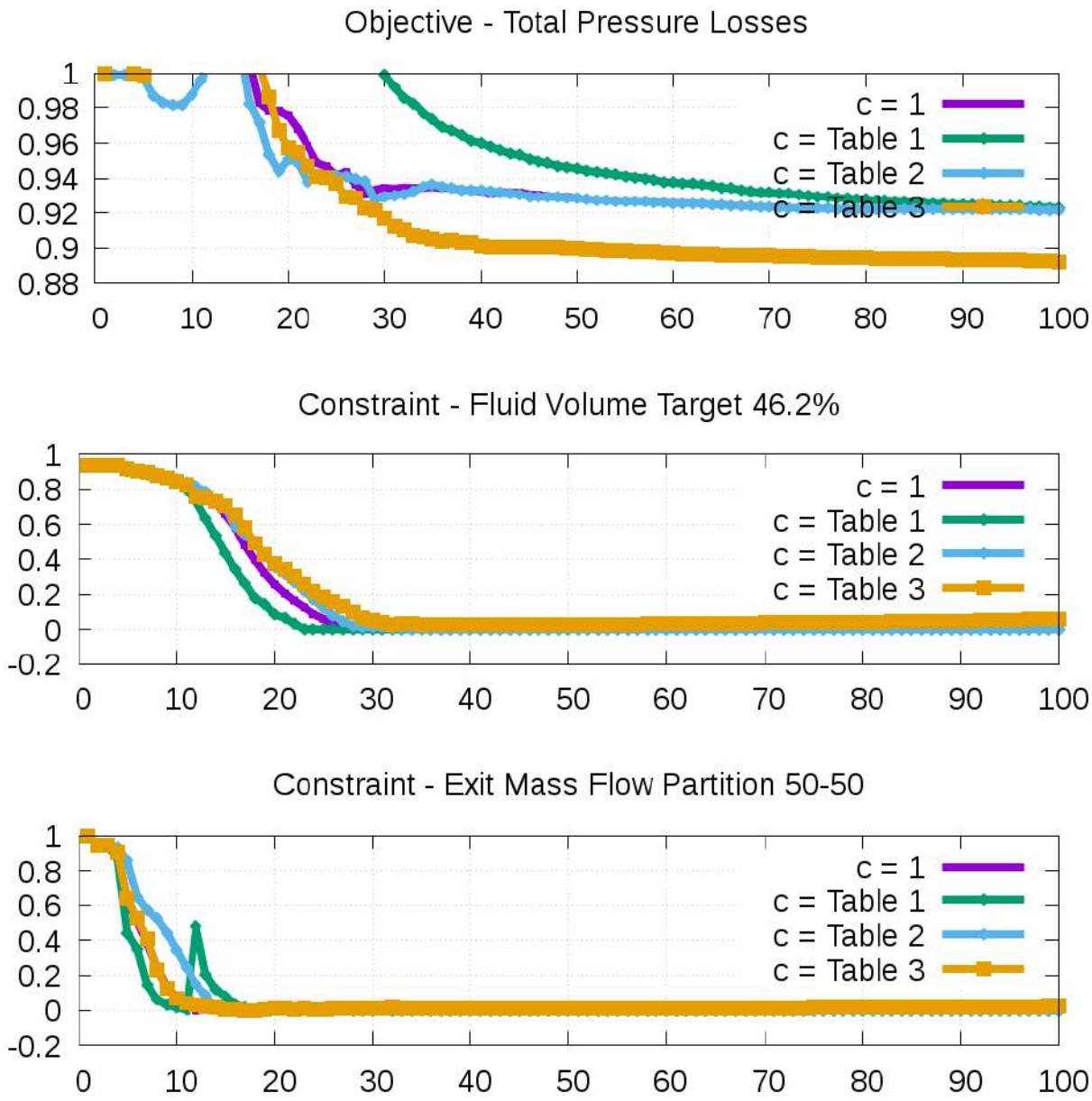

Figure 4.16: Objective-total pressure losses and constraint-TopO geometry and mass partition for case 2 and c keeping a constant value of 1 and varying according to table 1, 2, 3.

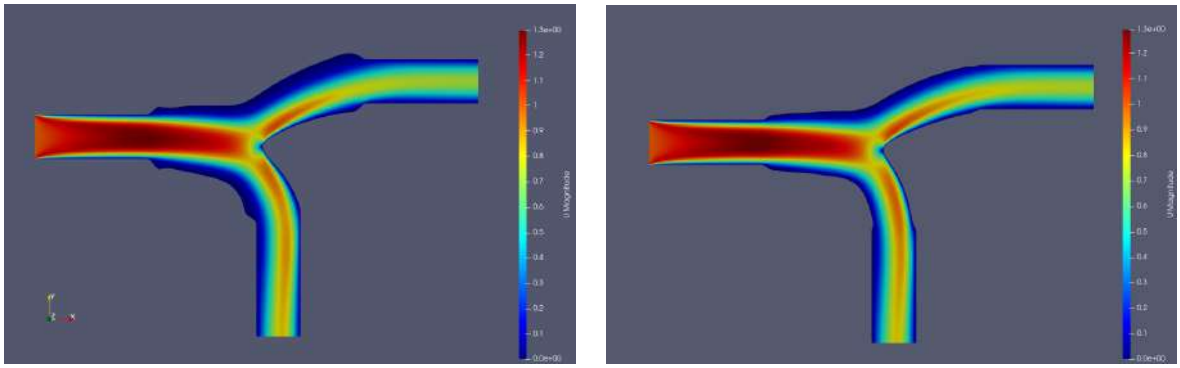

(a) Reducing c according to Table 3.

(b) $c = 1$

Figure 4.17: Case 2 resulting velocity magnitude fields for reducing value of c according to Table 3 and constant value $c = 1$.

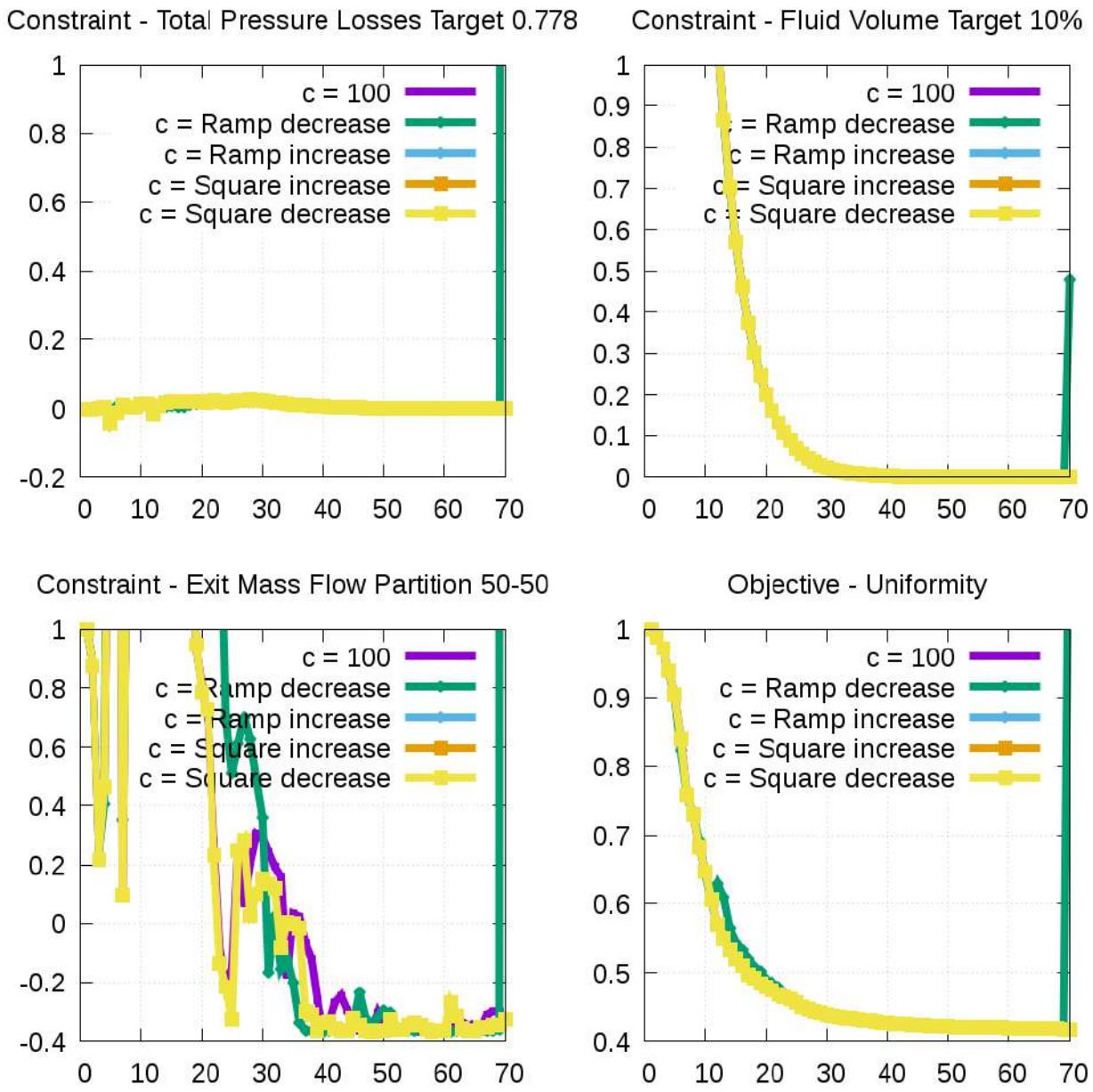

Figure 4.18: Objective (flow uniformity at the outlets) and constraints (TopO volume, outlet mass flow partition, and total pressure losses) for Case 3, with c held constant at 100, and varied linearly and quadratically (increasing and decreasing).

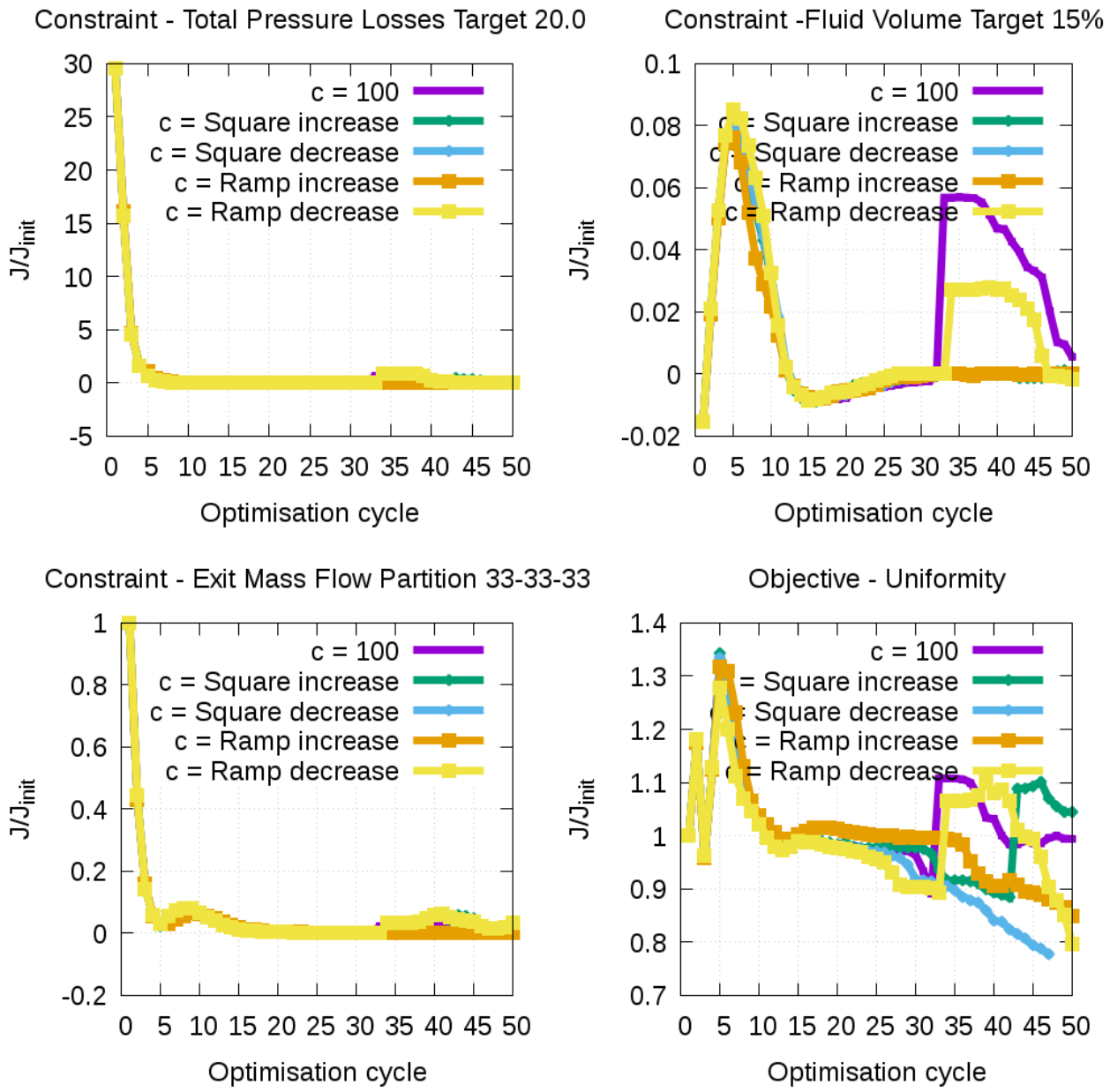

Figure 4.19: Objective (flow uniformity at the outlets) and constraints (TopO volume, outlet mass flow partition, and total pressure losses) for Case 4, with c held constant at 100, and varied linearly and quadratically (increasing and decreasing).

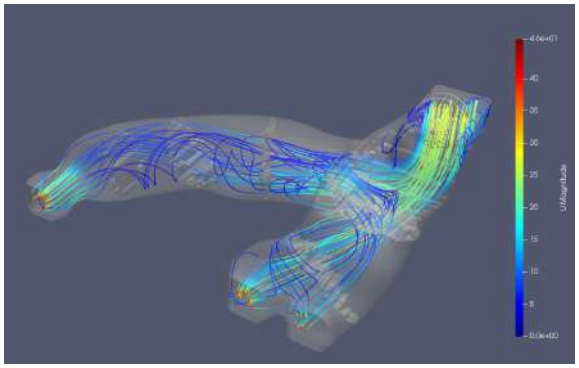

(a) Linearly reduced c.

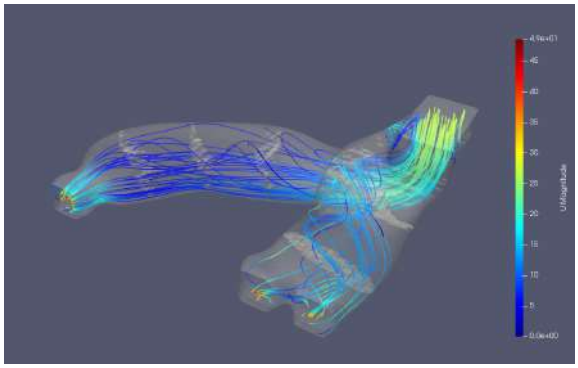

(b) Linearly increased c.

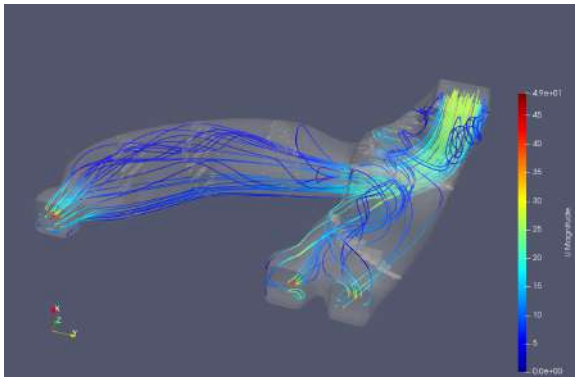

(c) Quadratically reduced c.

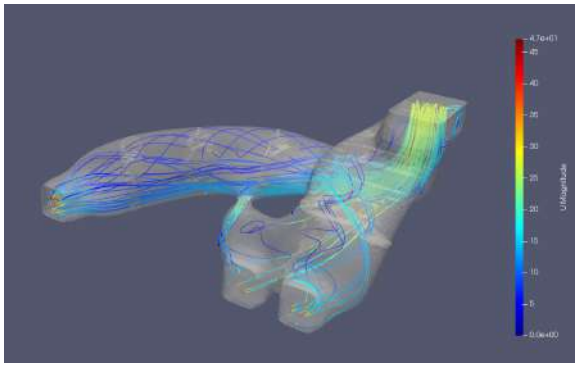

(d) Quadratically increased c.

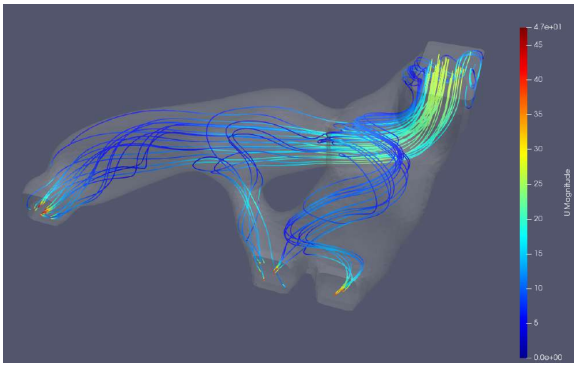

(e) $c = 100$

Figure 4.20: Case 4 resulting geometries and stream lines for reducing and increasing value of c (linearly and quadratically) and constant value $c = 100$.

Chapter 5

Overcoming SQP Issues - Demonstrations in ShpO

Infeasibility in the SQP sub-problems , can also be observed in Shape Optimization problems. This is typically the case, for applications with initial geometries significantly violating the imposed constraints. In this chapter, three 2D aerodynamic benchmarks are being examined. The fist two involve drag minimization of a NACA0012 airfoil with different B splines control boxes, used for mesh control. In the third, total pressure losses of a turbomachine's stator blade are minimized. In all cases, the same settings for c are applied, both constant and varying, as in the TopO cases of the previous chapter.

The objectives to be minimized and constraints used in the following cases are: the aerodynamic forces, i.e lift and drag, in the first and second case, the inlet-to-outlet total pressure losses in the third case and the partial volume between suction and pressure sides in all three cases. The exact mathematical expressions are presented:

Force

$$J = \frac{\int_{S_W} \rho \left(-\tau_{ij} n_j + p n_i\right) r_i \, dS}{\frac{1}{2}\rho A U_\infty^2}$$

where τ_{ij} are the components of the stress tensor, p is the pressure divided by the constant density ρ and n the unit normal vector. Vector r defines the direction in which the force vector should be projected (e.g. parallel to the farfield velocity to minimize drag). Repeated indices imply summation. In addition, S_W are the wall patches on which force is defined, A is the frontal area and U_{inf} the farfield velocity magnitude.

Total Pressure Losses

$$J = -\int_{S_{I,O}} \left(p + \frac{1}{2}v_k^2\right) v_i n_i \, dS$$

where u_i are the components of the velocity field, S_I and S_O are the inlet and outlet patches, respectively.

Partial Volume

$$J = \frac{V - V_{\text{init}}}{V_{\text{init}}}$$

$$V = -\frac{1}{3}\int_{S_W} x_k n_k \, dS$$

where V is the volume enclosed by the patches defining S_W and V_{init} is the volume of the initial geometry, defined in the same way.

5.1 NACA0012 With Control Box A

The following case, involves a symmetric NACA0012 airfoil with span of 1 m. The 2D air flow is entering the domain with an attack angle equal to +2 deg, and is assumed incompressible and laminar. The Reynolds number, based on the airfoil's span, is 400,000. The optimisation problem aims to minimize the drag force implied on the airfoil, keeping a volume decrease lower than 15% of its initial value and increase lift by 20%. A C-type mesh is being used of 37,800 cells and the distance from the airfoil to the farfield boundary set is equal to 15 times the airfoil's span. The mesh is presented in Figures 5.1.a and 5.1.b and the boundary conditions for velocity and pressure in Table 5.1:

Region	**U**	**p**
Farfield	(5.99, 0.21) (Dirichlet)	zero gradient (Neumann)
Airfoil	zero gradient (Neumann)	0 (Dirichlet)

Table 5.1: Boundary Conditions of the primal fields in 2D laminar case 1.

The B-splines parameterized, domain is being controlled by the Control Points (CPs) presented in Figure 5.2. The control box of this case has been chosen in a way to exclude the leading and the trailing edge of the airfoil. The design variable set consist of the (x, y) position coordinates of the four inner CP columns. The two far left and far right, CP columns are kept fixed to mitigate thickness decreasing at the edges.

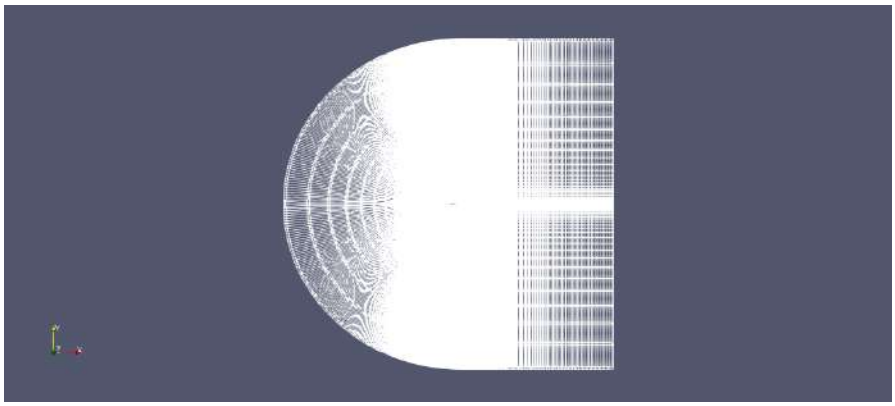

(a)

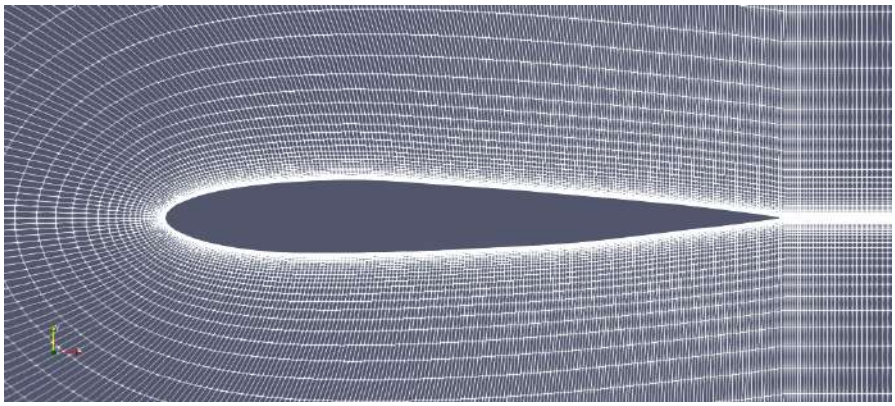

(b)

Figure 5.1: Mesh of NACA0012 cases.

Five runs have been conducted with similar setting as in TopO benchmarks in chapter 4: setting c equal to 1, equal to 100 and varying its value according to columns of Table 5.2. Corresponding to Table 4.3 for the TopO cases, the 1st column implies a gradual increase on factor c with a start value of 1 and end value of 100, the 2nd column implies a gradual increase with a start value of 0.1 and end value of 50 and the 3rd column implies a gradual decrease with a start value of 1 and end value of 0.

Cycle	**1**	**2**	**3**
1	1	0.1	1
5	5	1	0.5
12	5	2	0.2
16	20	5	0.1
20	50	50	0

Table 5.2: Varying values of c for all three ShpO cases.

Without the addition of the extra design variables, the QP sub-problem has been shown to fail

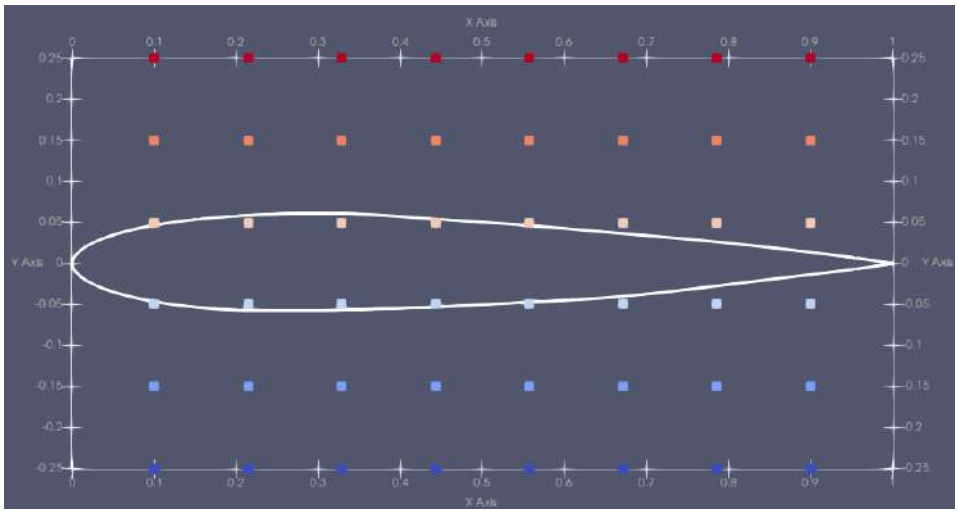

Figure 5.2: B-splines control box of the airfoil case 1.

to converge, at the 1st optimization cycle. Different c settings doesn't change the objective's decrease rate significantly, depicted in Figure 5.3. All runs converge to a drag decrease of 1% and a volume decrease of 9%. The starting and final geometries, velocity magnitude and pressure fields are presented in Figure 5.4.

5.2 NACA0012 With Control Box B

The 2nd case of NACA0012 airfoil is turbulent, and shares the same settings, except for a similar CP box including leading and trailing edges with fixed. The CP is shown in Figure 5.5. The Spalart-Allmaras model is being used for turbulence handling, together with a High-Re approach for the calculation of $\tilde{\nu}$ at the wall cells.

Similar results are produced as laminar case 1. The optimization problem cannot be solved without the addition of the extra design variables. Different c settings lead to similar optimization trajectories and end-geometries with total drag and volume reductions of $2 - 2.5\%$ and 14%, shown in Figure (4.6). $c = 1$, drives the SQP algorithm towards a slightly better solution, yet the relative difference of 0.25% is considered negligible, taking into account the semi-convergence of all runs, indicated by the non zero slope of the objective's and constraint's. The initial and final geometries, velocity magnitude and pressure fields are presented in Figure (5.7) and (5.8). The pressure contours are illustrated in Figure (5.9).

The setup used in the 2nd airfoil case, leads to a smoother geometry with uniform volume reduction across the airfoil's body. This major difference between the two cases is caused by

including the whole airfoil's body into the control box. Different c setup has not shown to improve objective reduction or constraint satisfaction rate in the 2D external aerodynamic cases of NACA0012 airfoil.

5.3 TU Berlin TurboLab Stator Blade

The last ShpO case involves the minimization of total pressure losses of a 2D section of the TU Berlin TurboLab Stator. The velocity is entering the domain with an attack angle of -42 deg from axial and magnitude of $48m/s$ and exiting with an angle of -2 deg at 0 pressure.
The air flow is considered incompressible and turbulent and a high-Re approach is being utilized with the usage of a wall function for the calculation of $\tilde{\nu}$ at the wall cells. The kinematic viscosity air is $\nu = 1.339e-05$. The mesh made of 63,332 cells is presented in Figure 5.12. The B-splines control box is depicted in Figure 5.11. The left two and right two columns of CP's are being kep at fixed position to prevent airfoil edge's thickness decrease. The bottom and up boundary sets are coupled with cyclic boundary conditions.

The boundary conditions corresponding to the primal problem are presented in Table 5.3. The objective of this case is the minimization of inlet-to-outlet total pressure losses and two constraints are included, a max volume reduction allowance of 20% and the exit flow angle's minimum value of 15 deg. The angle constraint produces the infeasibility targeted in the current case. For the same c settings the objective and constraints values across 20 optimization cycles are presented in Figure (5.14).

Region	**U**	**p**	$\tilde{\nu}$
Inlet	(35.67, -32.11)	zero gradient	30e-5
Outlet	zero gradient	0	zero gradient
Airfoil	0	zero gradient	-

Table 5.3: Boundary Conditions of the primal fields in case 3.

In all cases the angle constraint remains unsatisfied. All c settings, apart from the dynamically decreasing values of the 3rd column of Table (5.2), lead to exit flow angles over 13 deg and most of them in increased objective values up to 20%. This is showcased also by the non uniformly distributed camber, depicted in the corresponding optimised geometries presented in Figures (5.15), for increasing or constant value, $c = 100$ and c varying according to 1st and 2nd columns of Table (5.2). On the other hand, c values lower or equal than 1, lead to pressure drops equal to its initial value and the resulting flow twist is similar to the rest of

the runs. The pressure and velocity magnitude fields of the initial blade and the optimised ones for $c = 1$ and $c = Table3$ are presented in Figures (5.16).

To conclude, in contrast to the first two ShpO cases, steering the value of c, drives the SQP algorithm towards different optimised geometries. Setting initially $c = 1$ and increasing its value (Table 1, Table 2 results) enforces gradually exit-flow-angle infeasible term $+cy$ in the augmented objective (problem 3.4), yet leading in high objective values. Decreasing c on the other hand produces a solution with low objective value, related to the other results, but it undermines the angle constraint satisfaction. The best c setting is keeping it at constant value of 1, leading into a gemetry with low constraint violation and objective value.

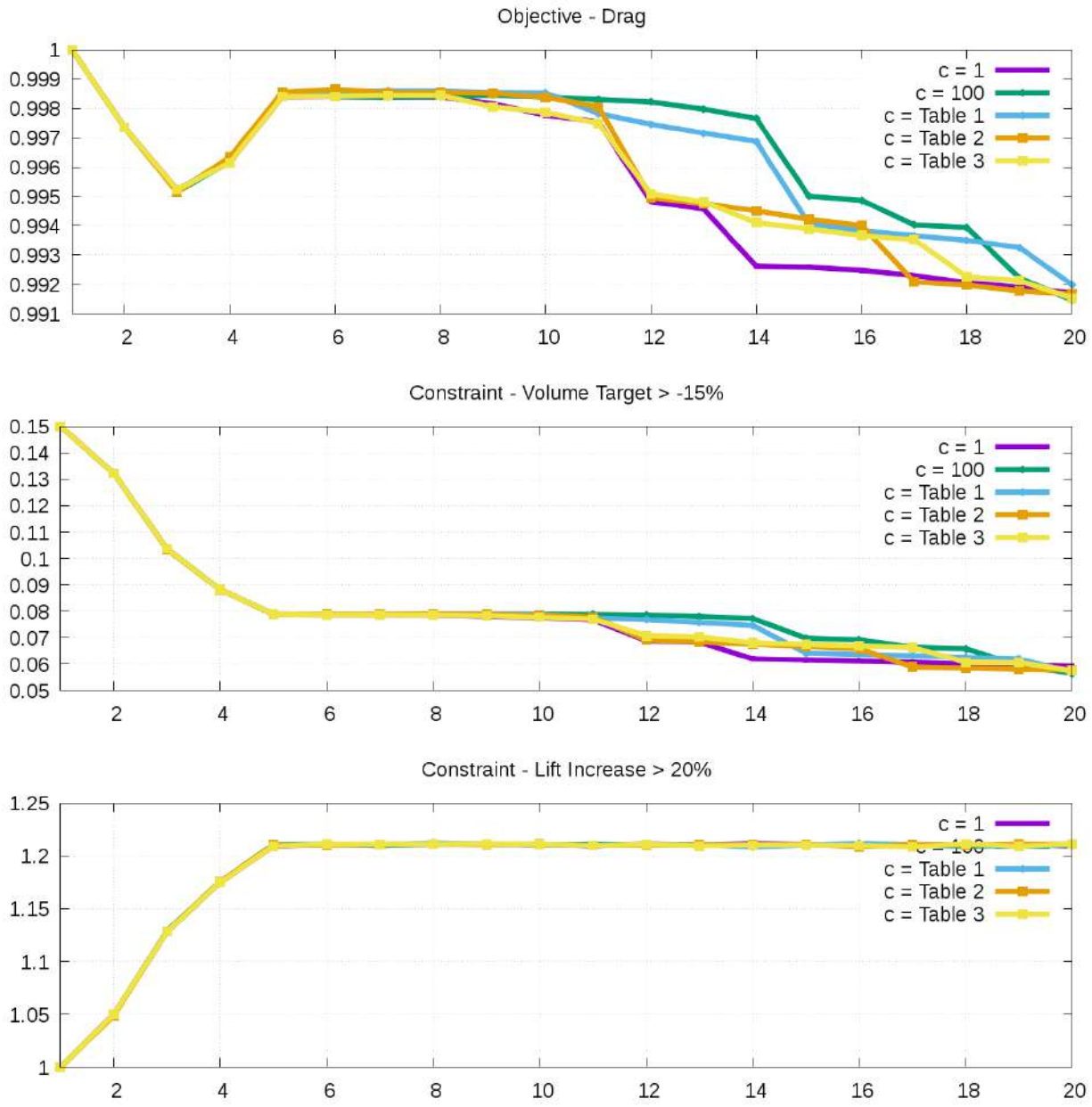

Figure 5.3: Objective and constraints results for the different settings of factor c.

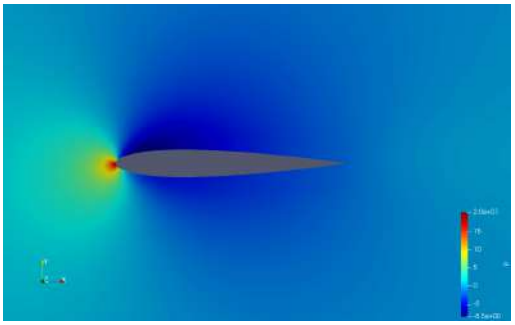

(a) Initial pressure field.

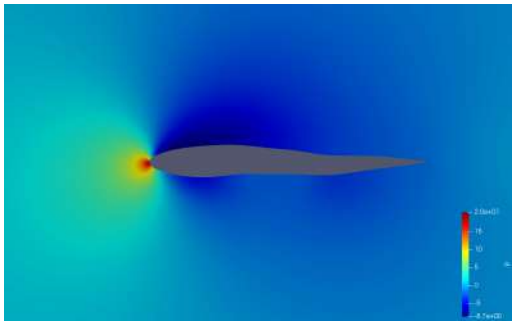

(b) Final pressure field.

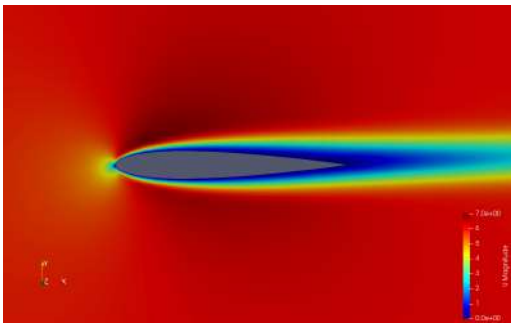

(c) Initial velocity magnitude field.

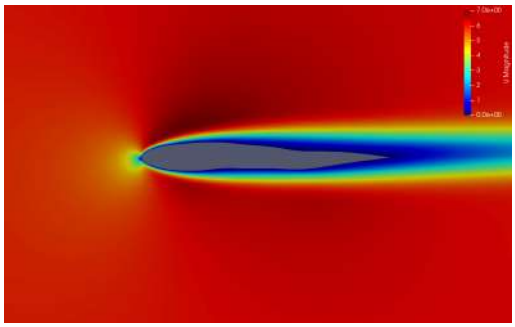

(d) Final velocity magnitude field.

Figure 5.4: Velocity and pressure fields for case's 1 start and end airfoil geometries.

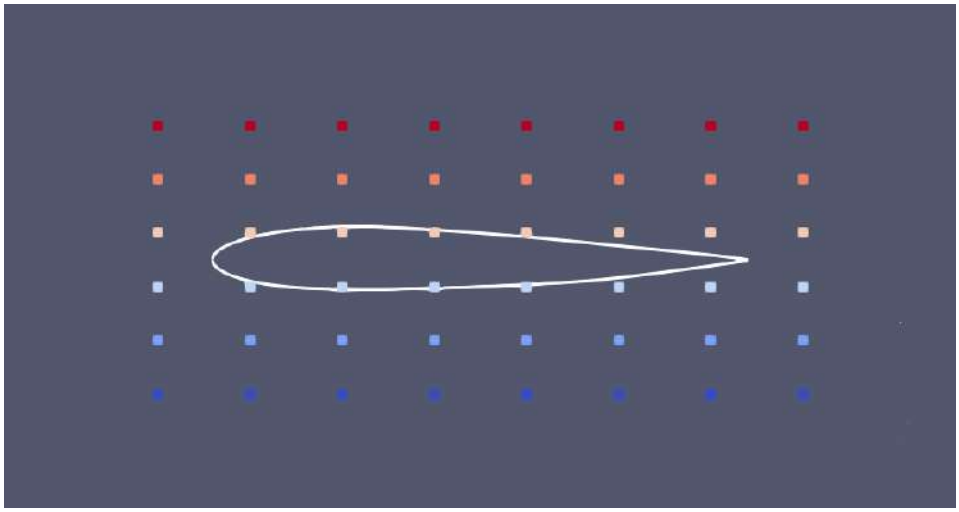

Figure 5.5: B-splines control box of the airfoil case 2.

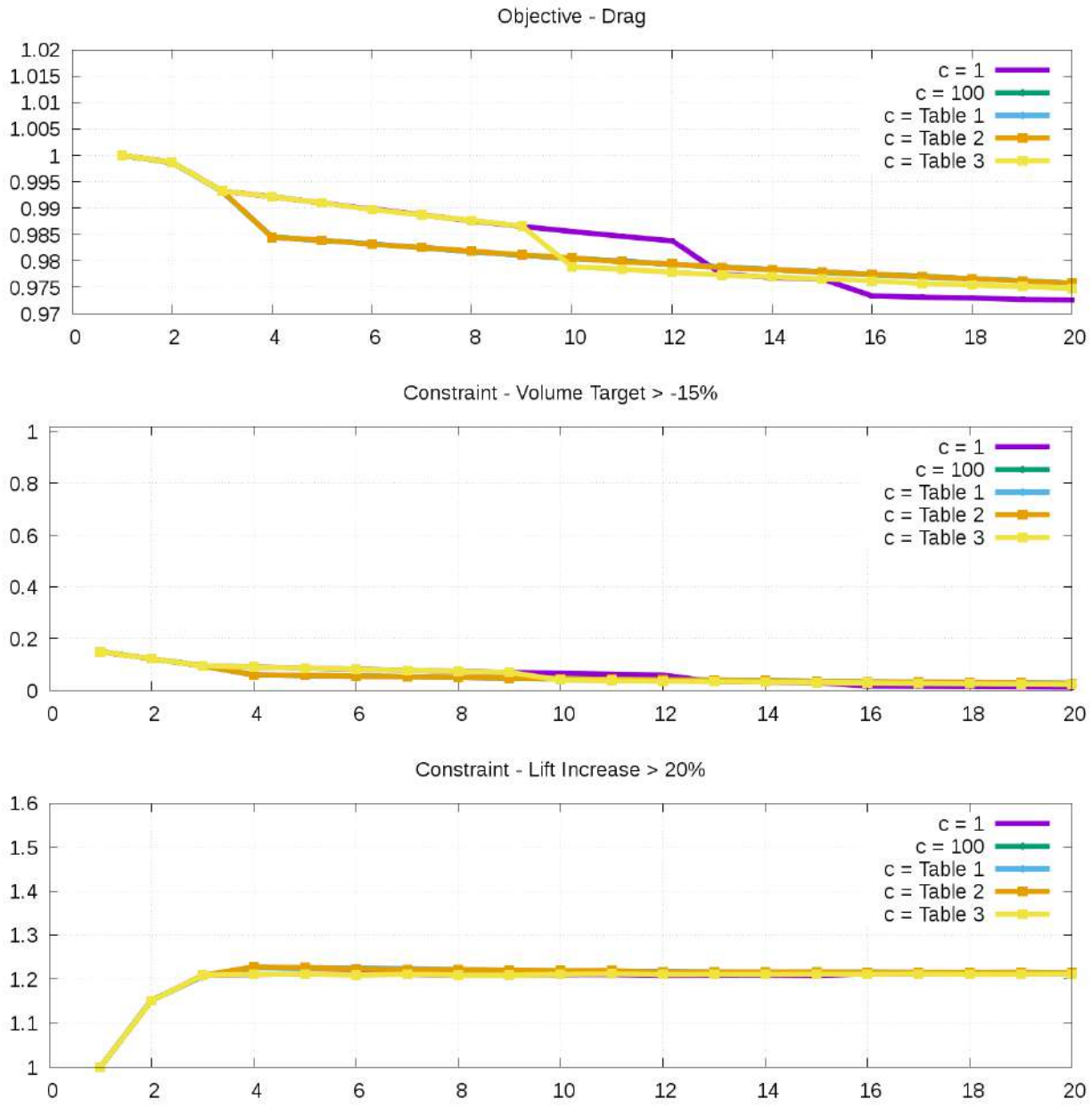

Figure 5.6: Objective and constraints results for the different settings of factor c.

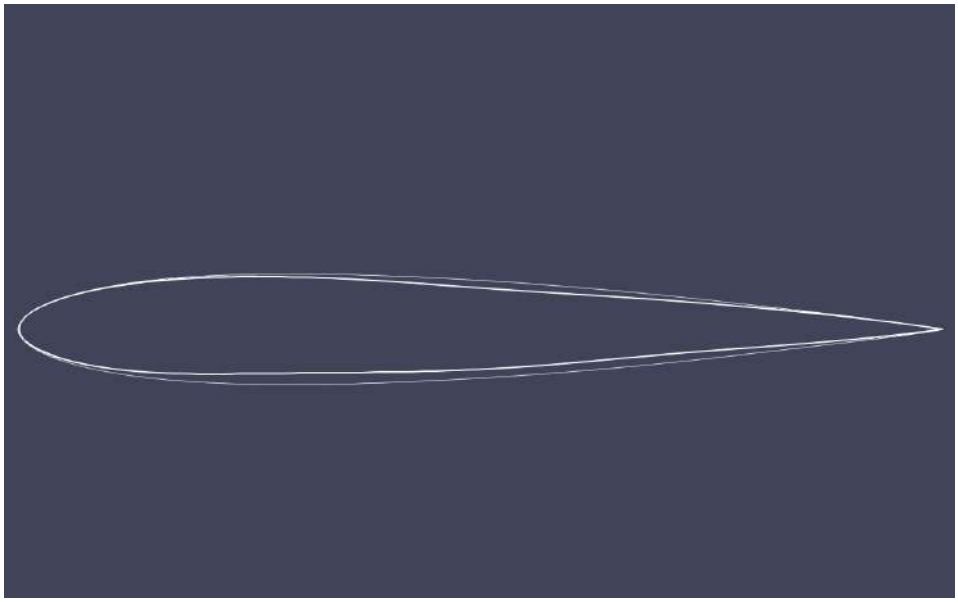

Figure 5.7: Initial and final geometry for NACA0012 airfoil turbulent case. The thicker airfoil-line corresponds to SQP solution.

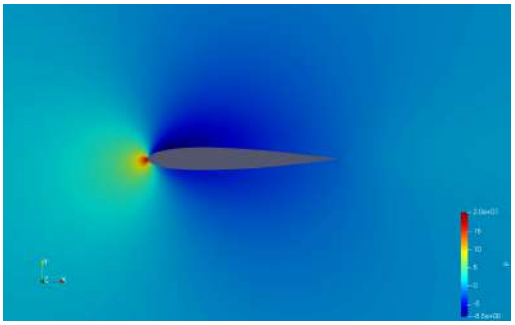

(a) Initial pressure field.

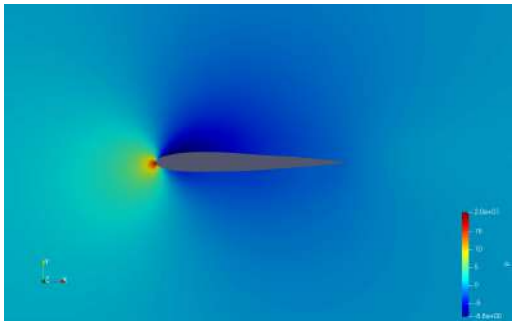

(b) Final pressure field.

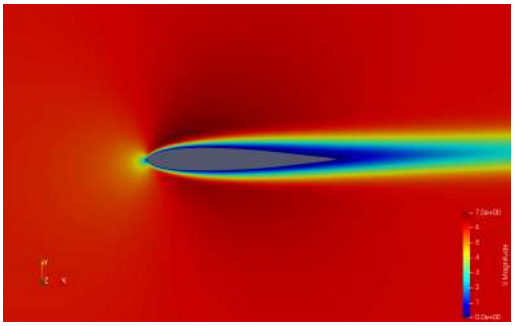

(c) Initial velocity magnitude field.

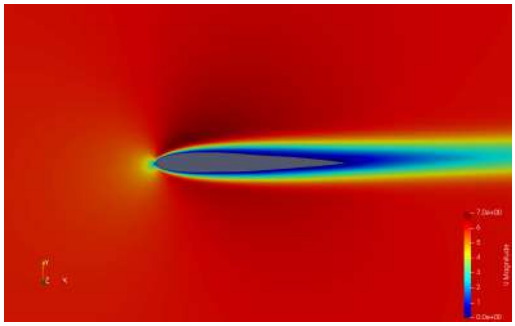

(d) Final velocity magnitude field.

Figure 5.8: Velocity and pressure fields for case's 2 start and end airfoil geometries.

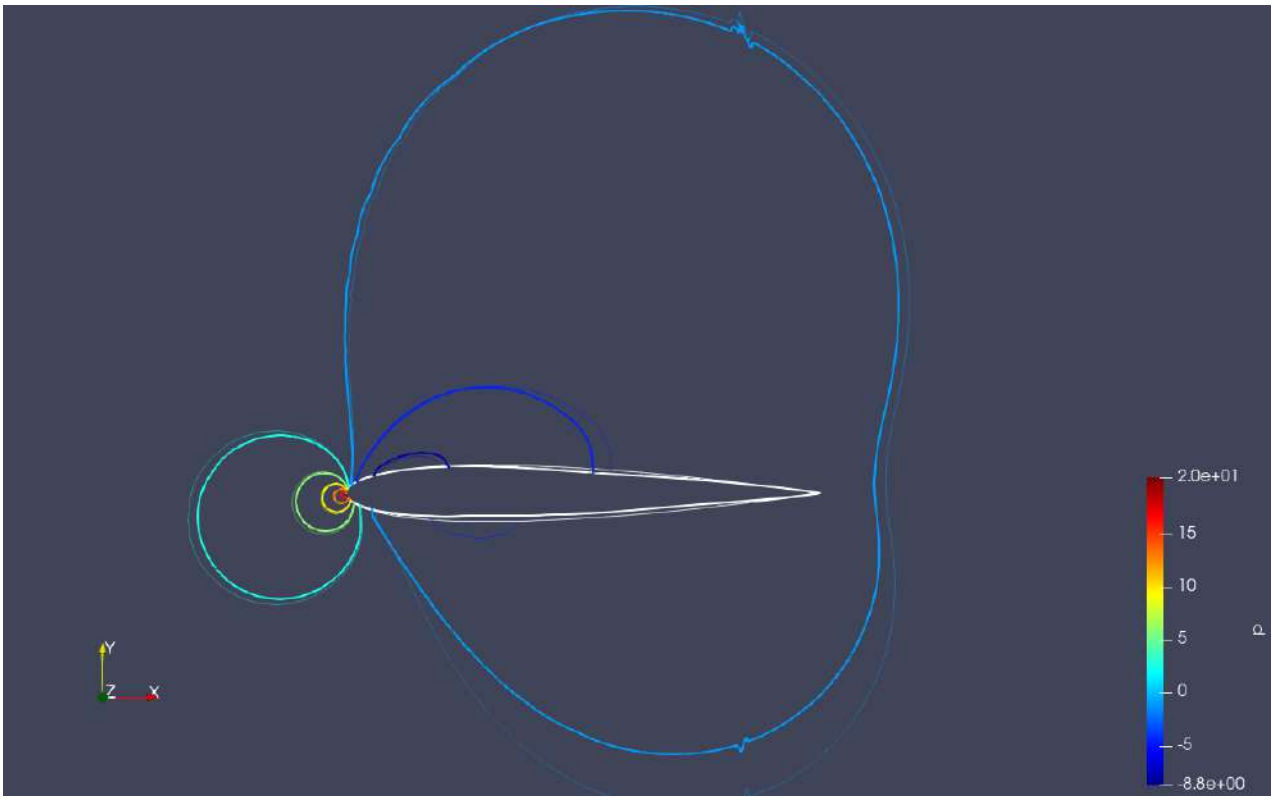

Figure 5.9: Pressure contours for initial and final geometry for turbulent case of NACA0012 airfoil. A set of ten contour lines are visible, for each geometry, corresponding to uniform distributed $\frac{p}{\rho}$ values from -8 to 20 $Pa/kg/m^3$. Thicker lines relate to final optimised airfoil's results.

Figure 5.10: TU Berlin TurboLab Stator model.

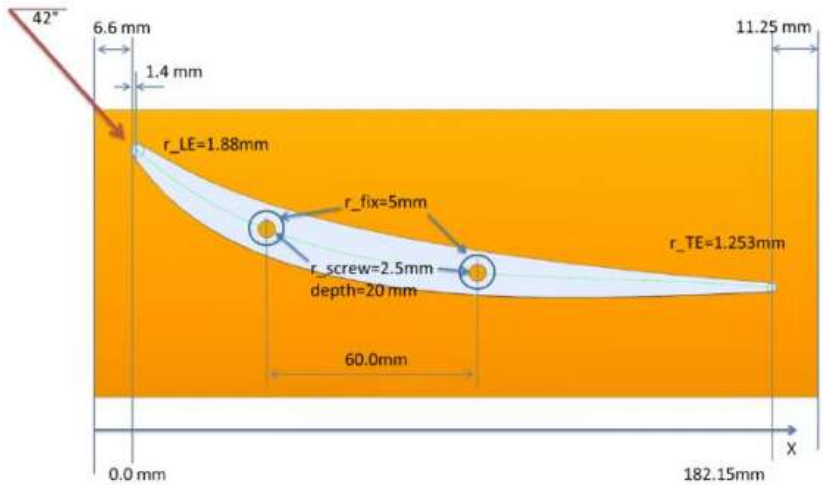

Figure 5.11: Stator blade section.

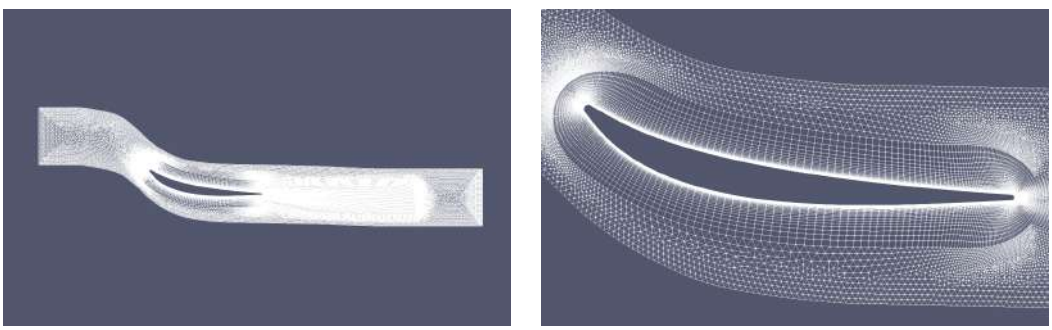

(a) (b)

Figure 5.12: Mesh of Berlin TurboLab stator's section .

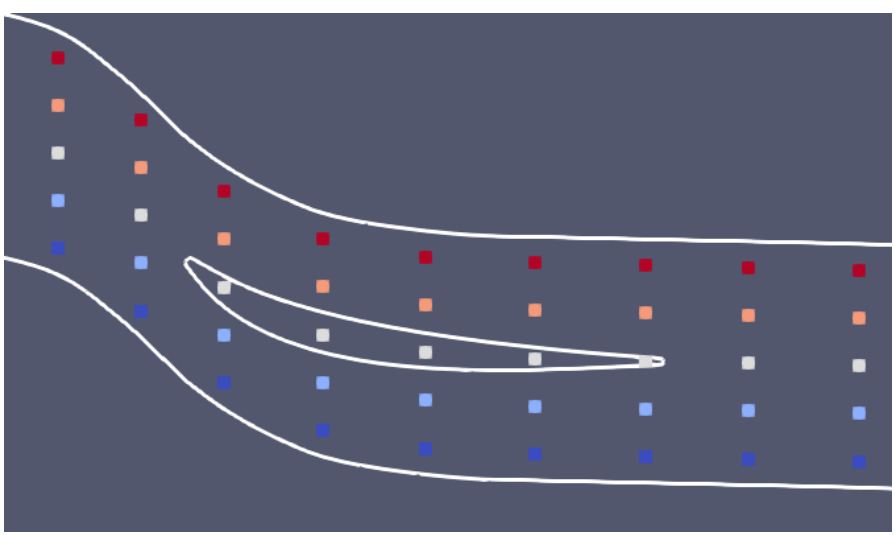

Figure 5.13: B-splines control box for Berlin TurboLab stator's case.

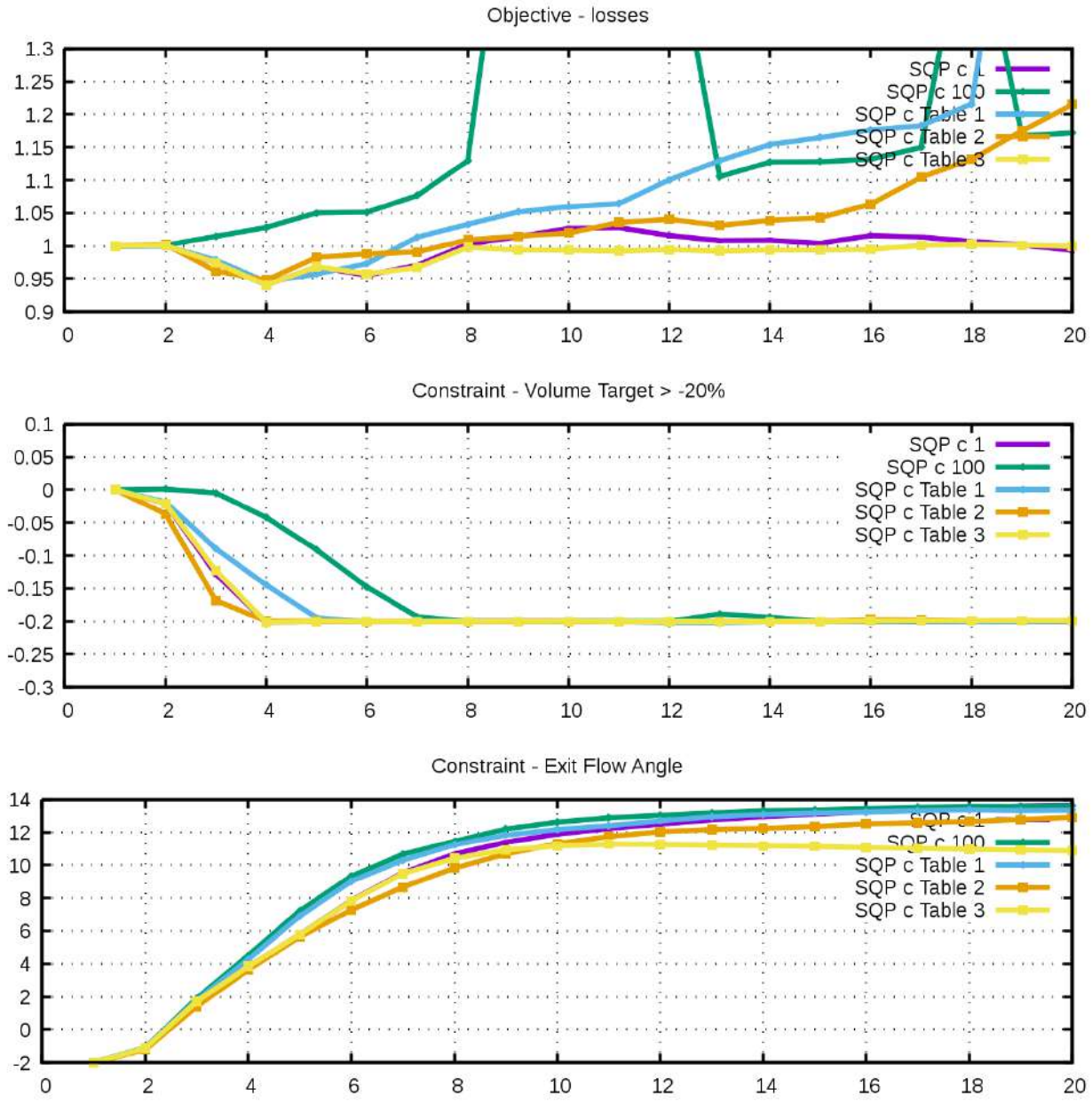

Figure 5.14: Objective and constraints results for the different settings of factor c for TU Berlin TurboLab Stator Blade case.

(a) c = 1

(b) c = 100

(c) c = Table 1

(d) c = Table 2

(e) c = Table 3

Figure 5.15: Optimised TU Berlin TurboLab Stator Blades (brighter lines) compared to the original (lower opacity).

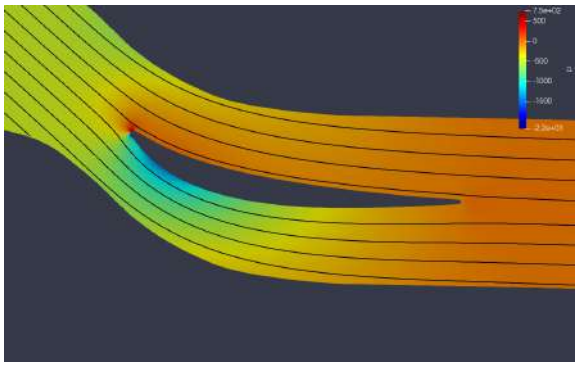

(a) pressure, initial

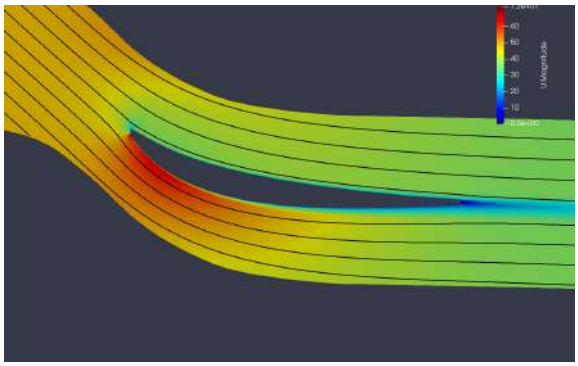

(b) velocity magnitude, initial

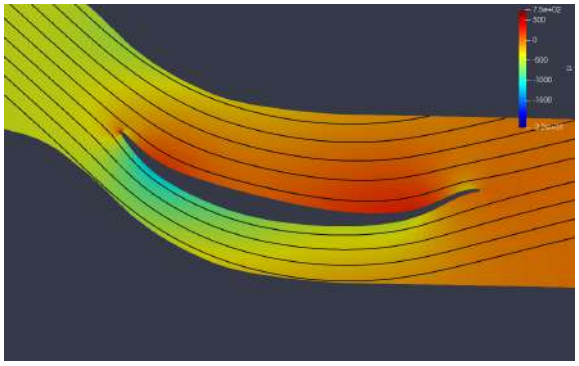

(c) pressure, c = 1

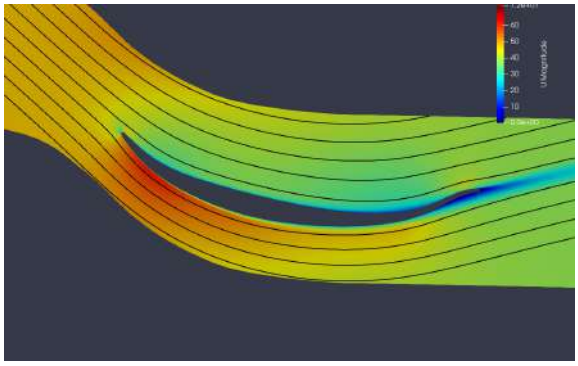

(d) velocity, c = 1

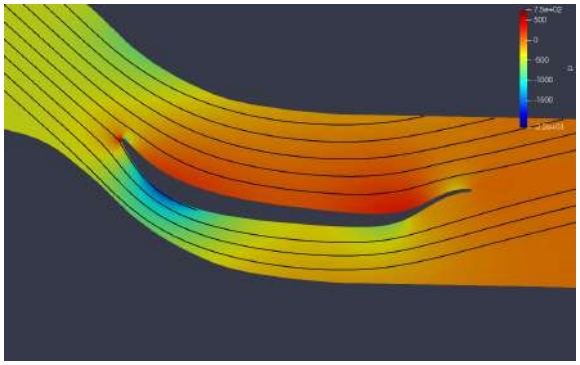

(e) pressure, c = 100

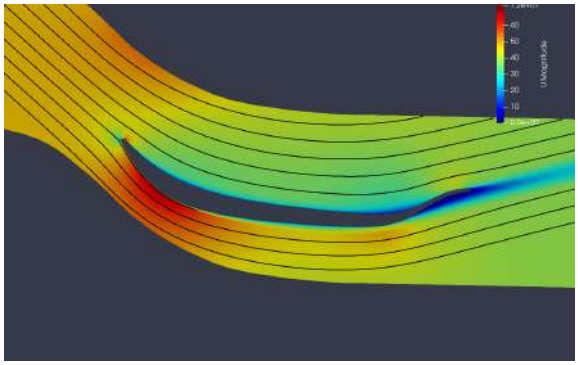

(f) velocity, c = 100

Figure 5.16: Pressure and velocity magnitude fields for initial and optimised blades for constant values of factor c.

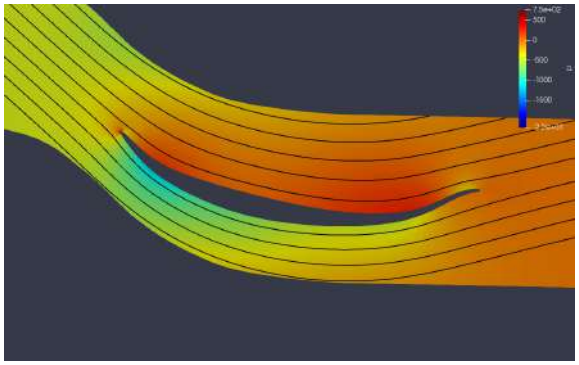

(a) pressure, c = Table 1

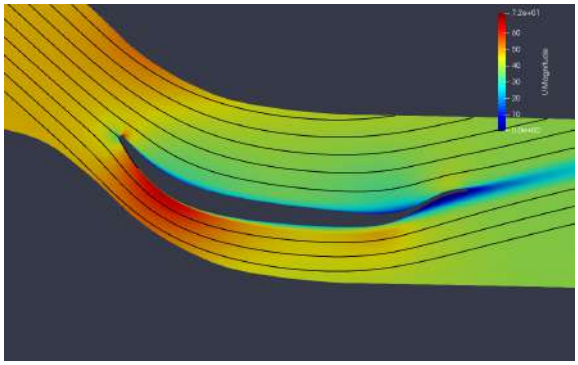

(b) velocity, c = Table 1

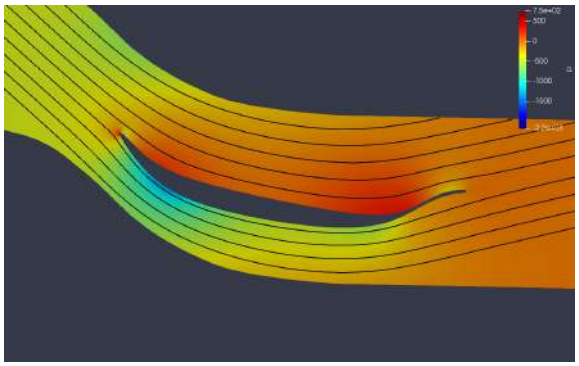

(c) pressure, c = Table 2

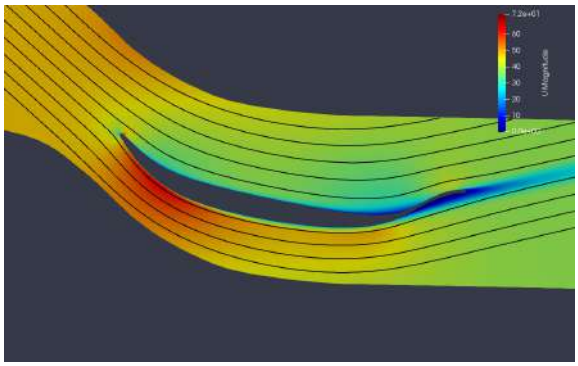

(d) velocity, c = Table 2

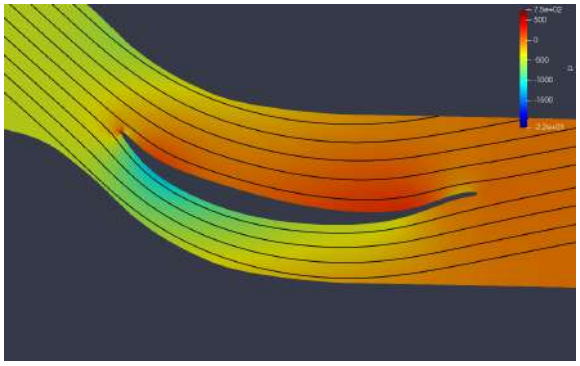

(e) pressure, c = Table 3

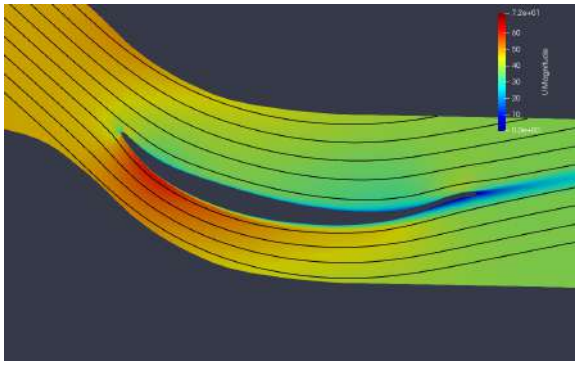

(f) velocity, c = Table 3

Figure 5.17: Pressure and velocity magnitude fields optimised blades for varying values of c.

Chapter 6

Overcoming SQP Issues - Demonstrations in CHT TopO

In this chapter, three mono-fluid Conjugate Heat Transfer (CHT) TopO cases are examined. The resulting geometries are aluminum heat sinks designed for cooling applications, using cool air at 273 K (0°C) as the working fluid to abduct heat from the hot aluminum boundary, maintained at 373 K (100°C). In all cases the same mesh, boundary conditions and constraint, setup is being used with the only difference located in the objective function.

Specifically the case consists of a 2D, symmetric, one (1) inlet, one (1) outlet geometry, presented in Figure (6.1.a). The active domain is colored in blue and its corresponding volume constraint is being set as a maximum air-occupied volume fraction of 70%. The mesh is made of 13,750 rectangular cells and is presented in Figure (6.1.b).

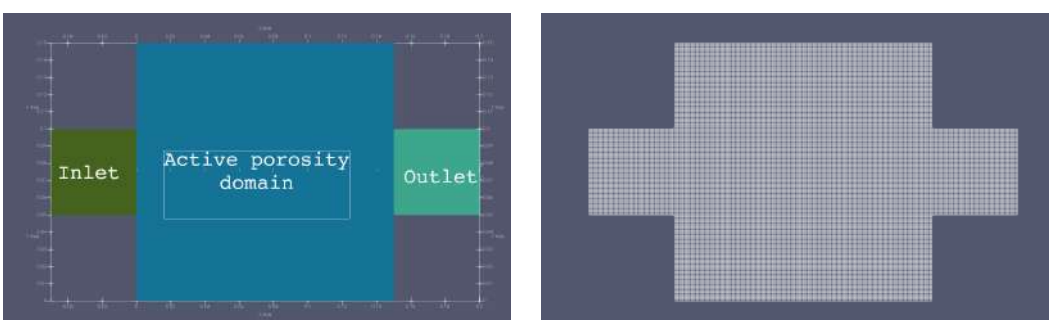

(a) (b)

Figure 6.1: Working 2D domain and respective mesh of CHT cases in chapter 5. The air flow is entering from the inlet located at the left and exiting the symmetrical domain from the right outlet. The cell set with variable porosity field values is depicted in blue.

The flow is turbulent, modeled using the Spalart-Allmaras model and the Reynolds number

corresponding to the inlet height is, $Re = 20,000$. The boundary conditions for the velocity, pressure, temperature and $\tilde{\nu}$ fields are shown in Table 6.1:

Region	**U**	**p**	**T**	$\tilde{\nu}$
Inlet	(6, 0)	zero gradient	273	10^{-4}
Outlet	zero gradient	0	zero gradient	zero gradient
Domain Boundary	(0,0)	zero gradient	373	zero gradient

Table 6.1: Boundary Conditions of the primal problem in 2D turbulent cases of chapter 6.

The objective function in the following three cases is a weighted sum of the mean domain temperature, used as a characteristic value related to the cooling performance of the generated heat sink at each optimization cycle, and the inlet-to-outlet total pressure losses. In every case the dominant term is the mean temperature, while the pressure losses term imposes energy efficiency characteristics to the overall objective function. The objective is mathematically expressed as:

$$J = w_1 \overline{T} + w_2 \Delta p_t$$

where,

$$w_{1,2} \in [0, 1], \quad w_1 + w_2 = 1$$

$$\Delta p_t = -\int_{S_{I,O}} \left(p + \frac{1}{2} v_k^2 \right) v_i n_i \, dS$$

$$\overline{T} = \frac{1}{S} \int_S T \, dS$$

In each case the weight sum is equal to 1 and the values used for each run is presented in Table 6.2:

case	$\mathrm{w}_1(\overline{T})$	$\mathrm{w}_2(\Delta \mathrm{p}_t)$
1	0.95	0.05
2	0.90	0.10
3	0.80	0.20

Table 6.2: Objective components weight values for the three cases of chapter 5. w_1 corresponds to the mean domain temperature, while w_2 corresponds to the total inlet-to-outlet pressure losses.

The results for 50 optimisation cycles, using constant c values, of $c = 1, 5, 100$ and identical to the aerodynamic TopO cases, varying values are presented in the following sections.

6.1 Objective's components weights: 95% - 5%

The convergence of objective's and constraint's values across the 50 cycles are presented in Figure 6.2. The generated heat sinks for all c settings are included in Figures 6.3 and 6.4. Decreasing c values, lead to lower objective's value, in comparison to the other runs, but fail to satisfy the volume constraint, as it is observed in figures 6.2 and 6.4, 'Table 3' results. All other runs are successful and one of them lead to best results, with respect to objective's both components and that's the 'Table 2' run of increasing c values. The resulting total pressure losses percentage with respect to the initial value has a value of 89% and the mean temperature a value of 43 C.

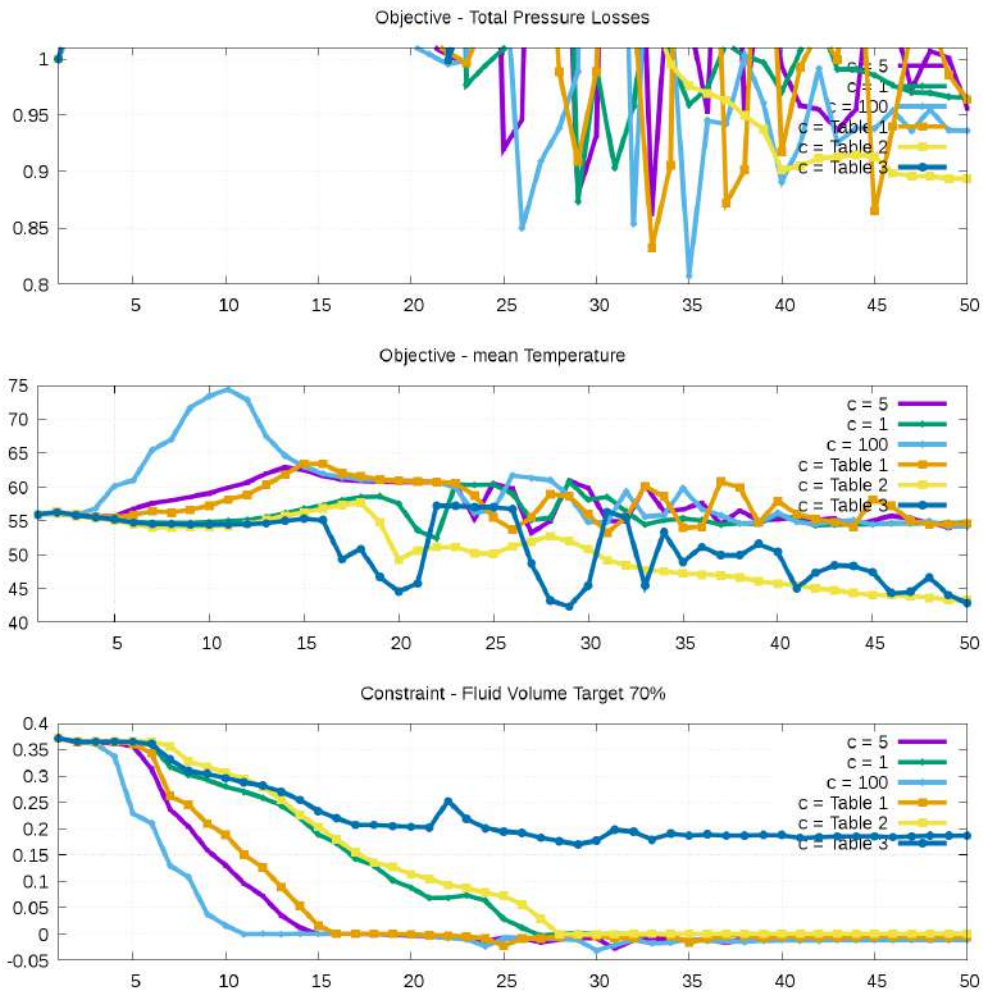

Figure 6.2: Results of the CHT case 1 of chapter 5, using in the objective, weight values 0.95 and 0.05 for the mean temperature and total pressure losses respectively.

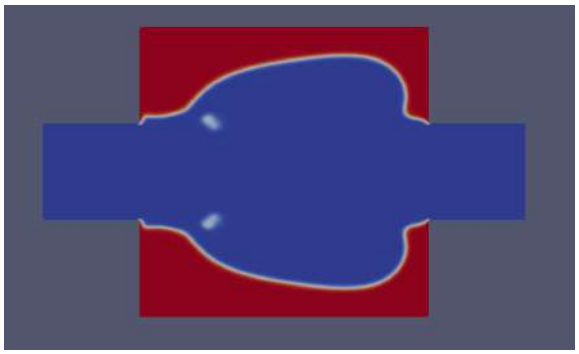

(a) porosity, c = 1

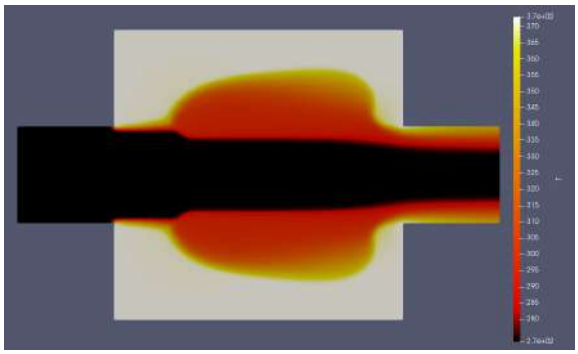

(b) temperature, c = 1

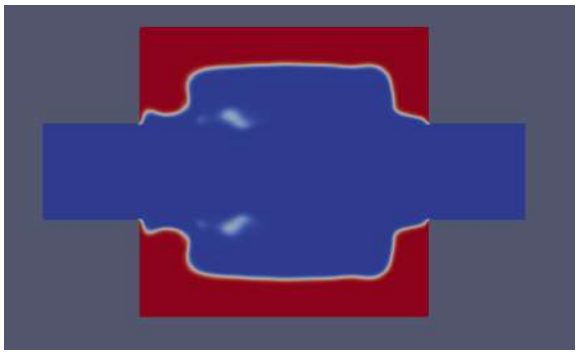

(c) porosity, c = 5

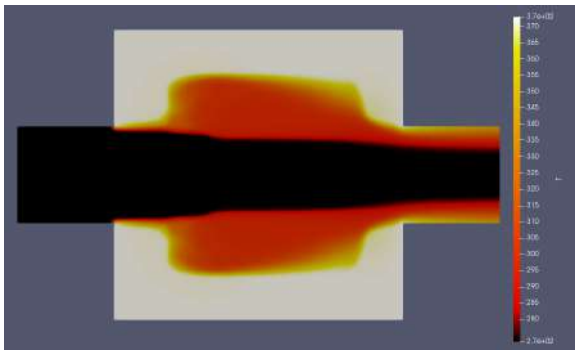

(d) temperature, c = 5

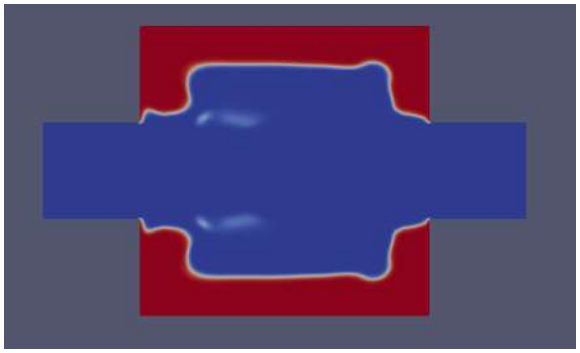

(e) porosity, c = 100

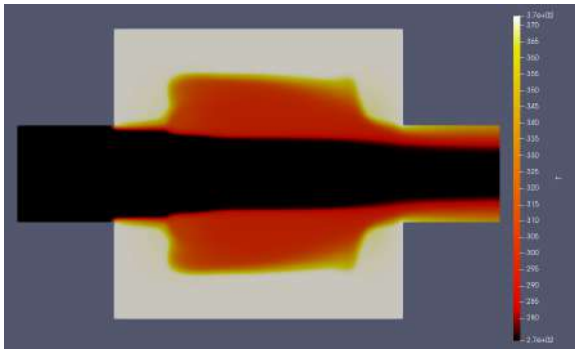

(f) temperature, c = 100

Figure 6.3: Porosity and temperature fields of generated heat sinks for constant c values.

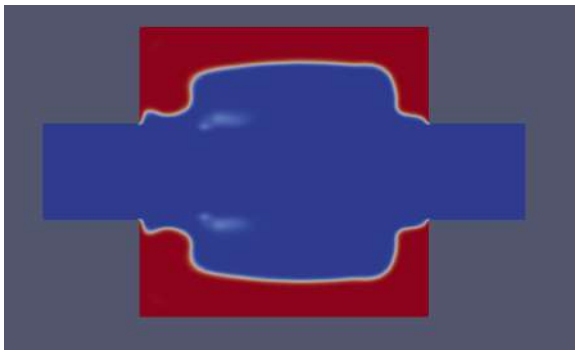

(a) porosity, c = table 1

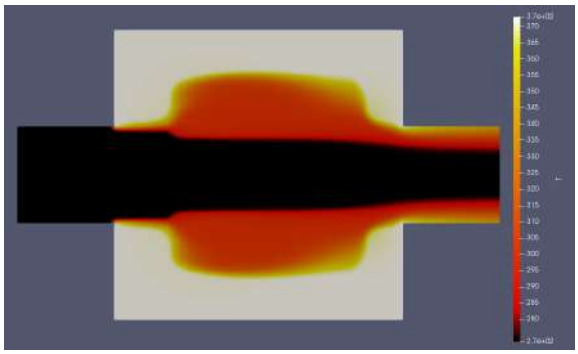

(b) temperature, c = table 1

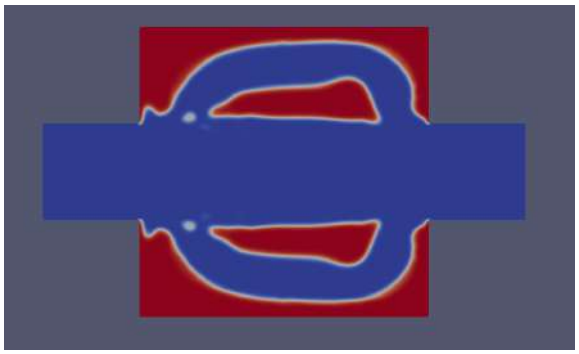

(c) porosity, c = table 2

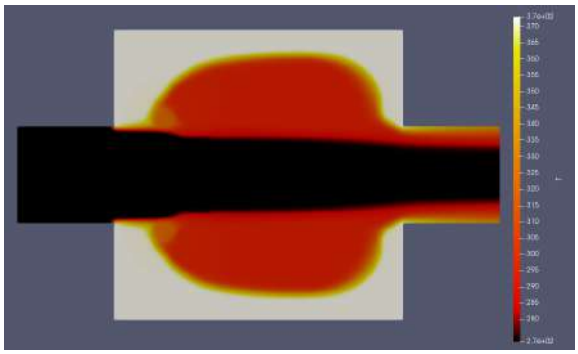

(d) temperature, c = table 2

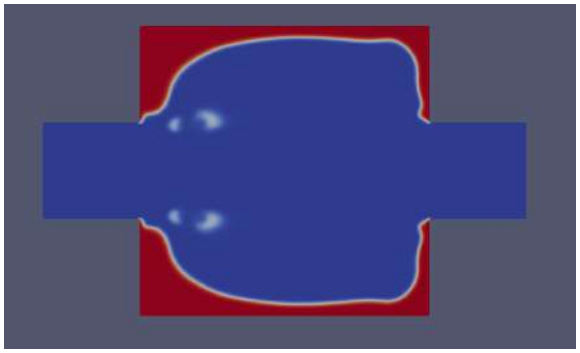

(e) porosity, c = table 3

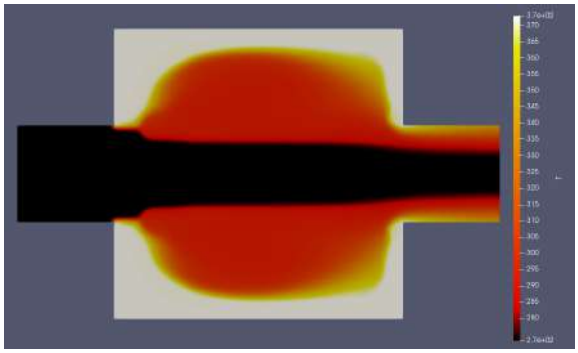

(f) temperature, c = table 3

Figure 6.4: Porosity and temperature fields of generated heat sinks for varying c values.

6.2 Objective's components weights: 90% - 10%

In Figure 6.5 the optimization loop results are depicted. The optimized heat sinks for constant and varying c values are included in Figures 6.6 and 6.7. In figures 6.6 and 6.7 is shown similarly to case 1, that decreasing c values leads to in-satisfaction of the volume constraint, yet low objective values. All other runs are successful and two of them lead to best results, with respect to objective's components. 'c = 5' run leads to the lowest total pressure losses, value of 82% and a mean temperature value of 58 C, while 'c = Table 2' run leads to the lowest mean temperature of 48 C and total pressure losses of 86 %.

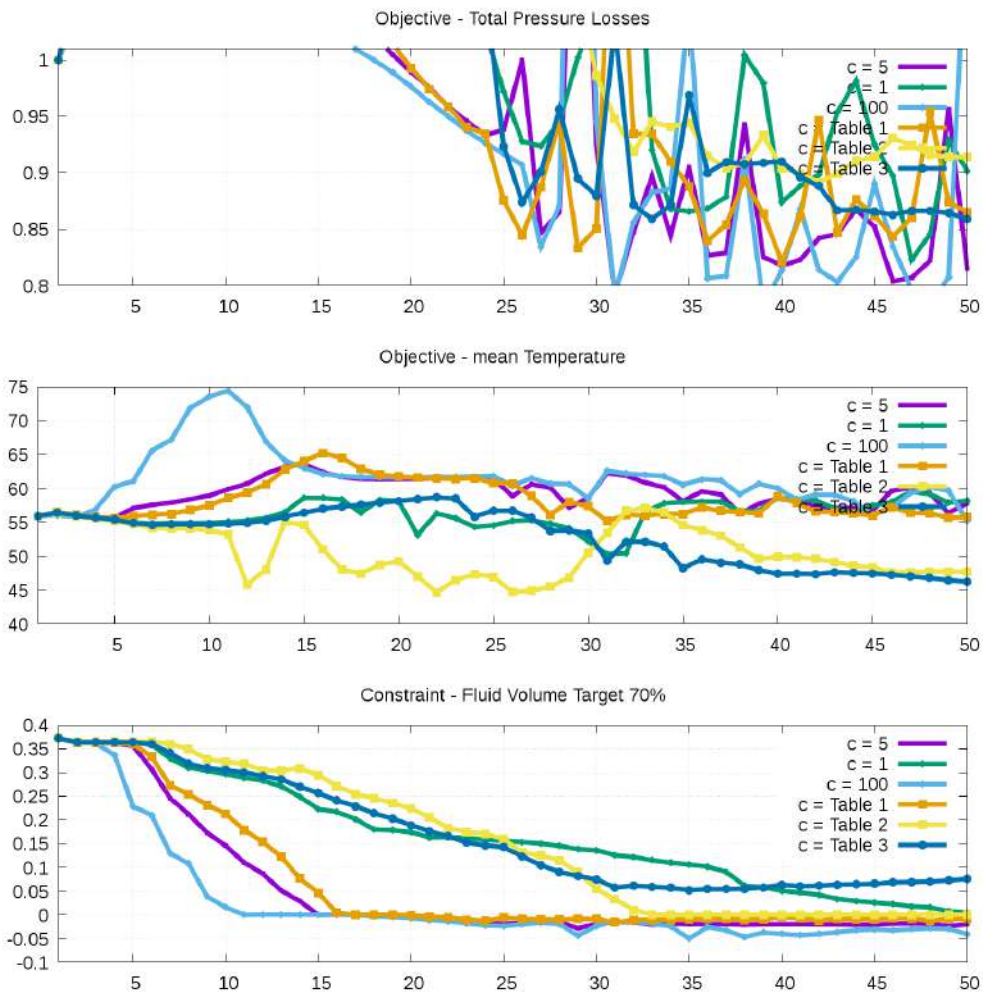

Figure 6.5: Results of the CHT case 1 of chapter 5, using in the objective, weight values 0.90 and 0.10 for the mean temperature and total pressure losses respectively.

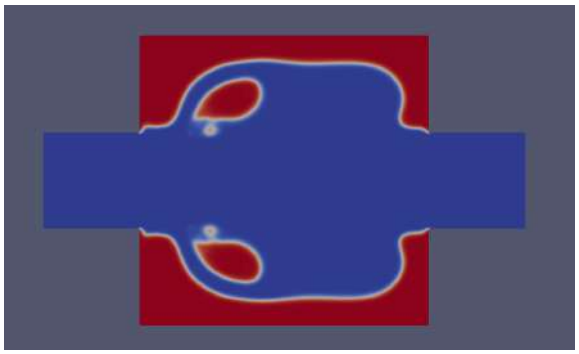

(a) porosity, c = 1

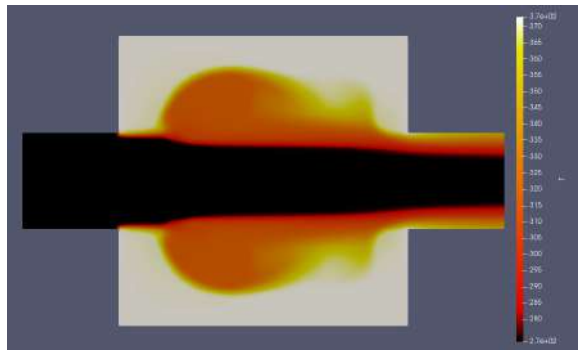

(b) temperature, c = 1

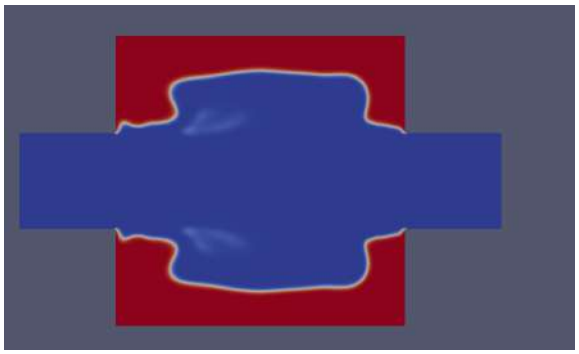

(c) porosity, c = 5

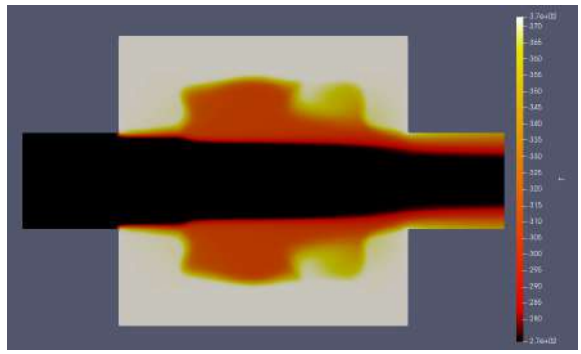

(d) temperature, c = 5

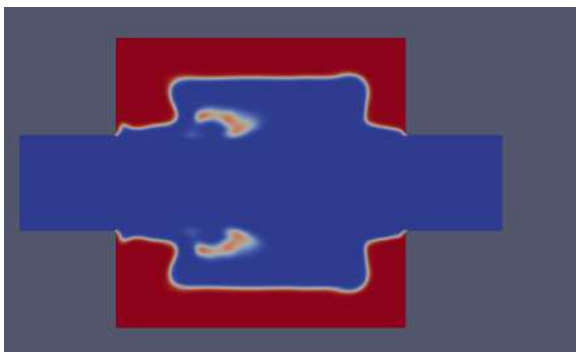

(e) porosity, c = 100

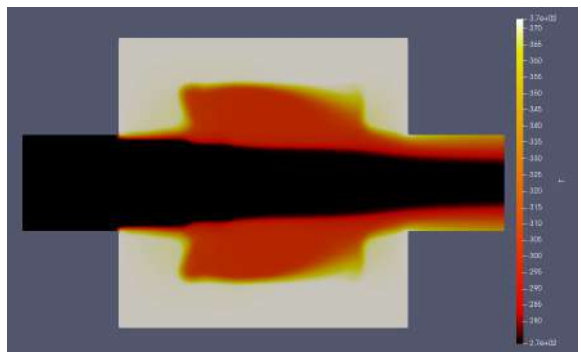

(f) temperature, c = 100

Figure 6.6: Porosity and temperature fields of generated heat sinks for constant c values.

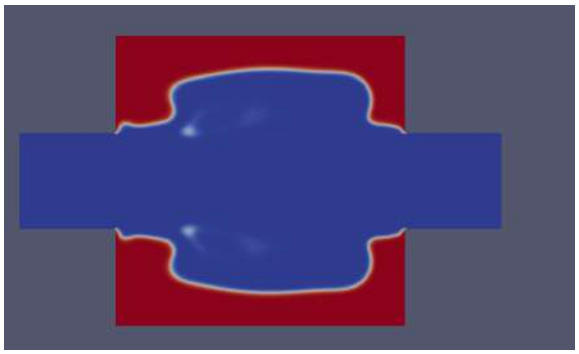

(a) porosity, c = table 1

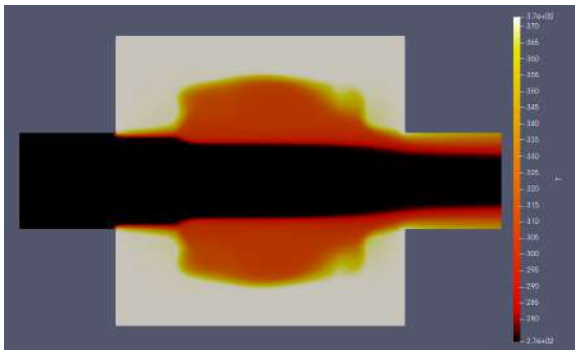

(b) temperature, c = table 1

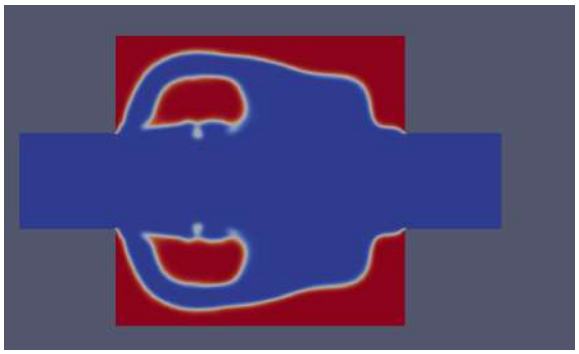

(c) porosity, c = table 2

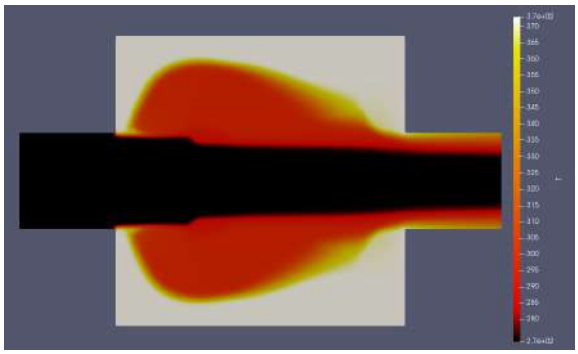

(d) temperature, c = table 2

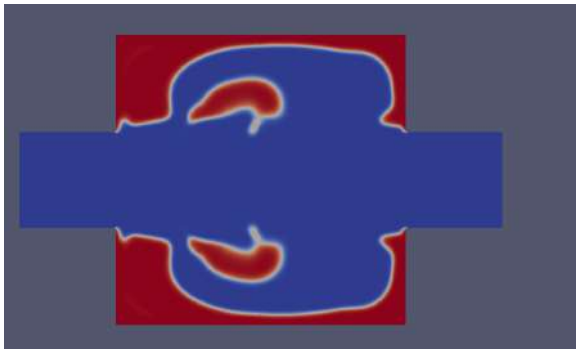

(e) porosity, c = table 3

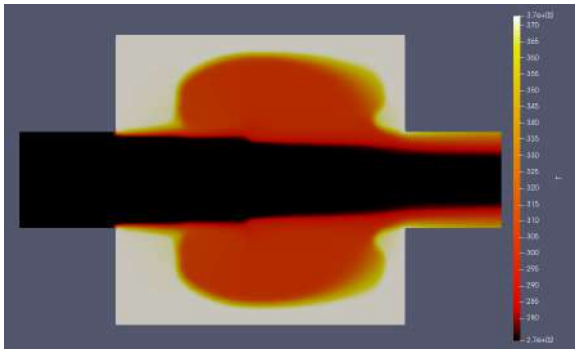

(f) temperature, c = table 3

Figure 6.7: Porosity and temperature fields of generated heat sinks for varying c values.

	c = Table 1	**c = Table 2**	**c = Table 3**
Δp_t[%]	70	76	80
T [C]	58	40	30

Table 6.3: Objective components weight values for the three cases of chapter 6. w_1 corresponds to the mean domain temperature, while w_2 corresponds to the total inlet-to-outlet pressure losses.

6.3 Objective's components weights: 80% - 20%

For mean-temperature and total-pressure-losses weights of 80% and 20% respectivelly, the convergence of objective's and constraint's values are presented in Figure 6.8 and the generated heat sinks are included in Figures 6.9 and 6.10. Using the current weights for the objective's components, 3 runs produced geometries with improved aerodynamic and thermal qualities, with characteristic values composing the pareto front of the dominating solutions of all 3 case runs. In table 6.3 the values of objective's components for 'c = 100', 'c = Table 2' and 'c = Table 3' runs are presented and in Figure 6.11 the Pareto front is shown. Increasing the weight of total pressure losses drives the algorithm towards local minima with improved qualities. This suggests that by focusing more on the aerodynamic efficiency of the heat sink, the d.v set is steered into a region with multiple flow canals, which, in turn, results in improved thermal dissipation qualities as well.

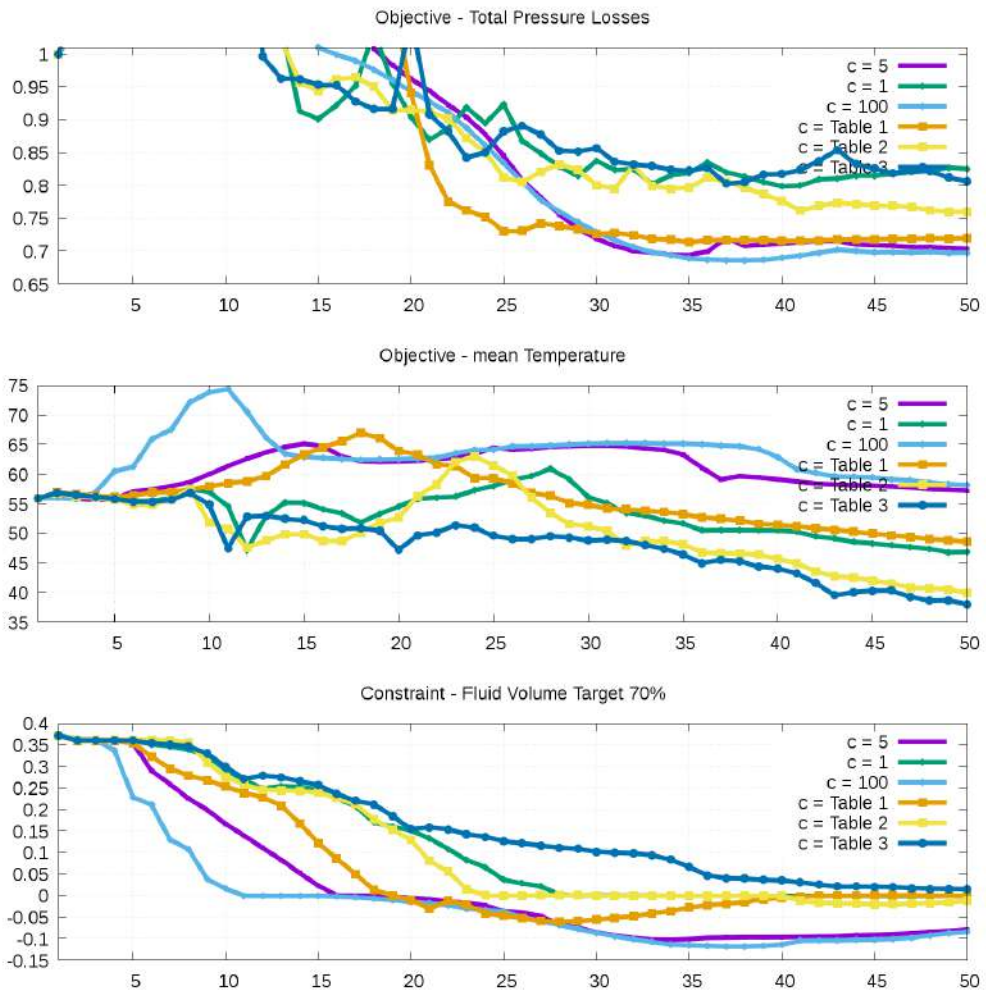

Figure 6.8: Results of the CHT case 3 of chapter 5, using in the objective, weight values 0.80 and 0.20 for the mean temperature and total pressure losses respectively.

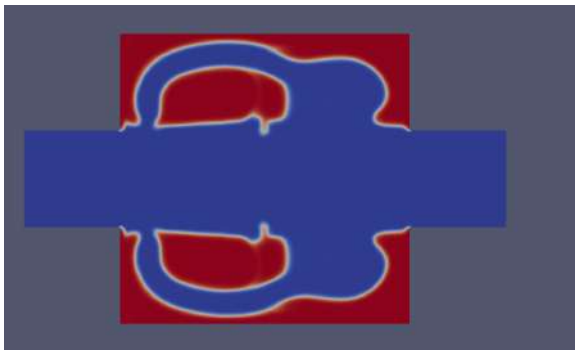

(a) porosity, c = 1

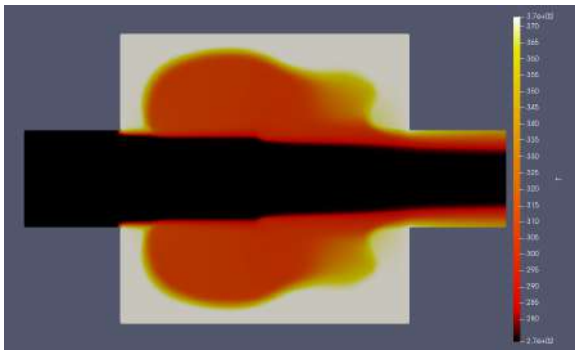

(b) temperature, c = 1

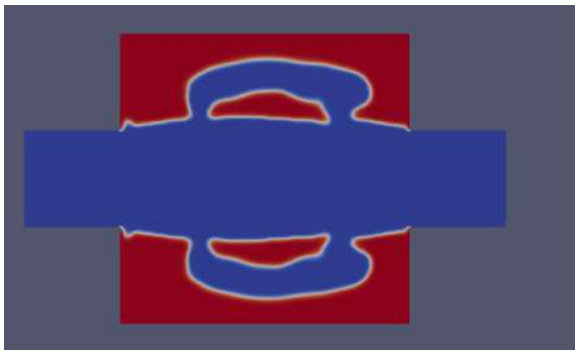

(c) porosity, c = 5

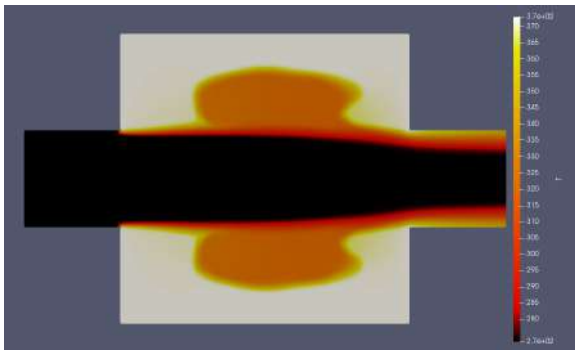

(d) temperature, c = 5

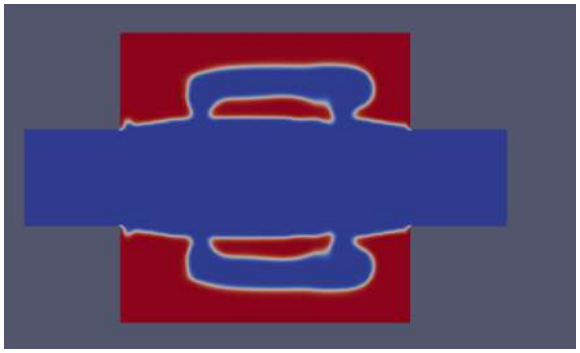

(e) porosity, c = 100

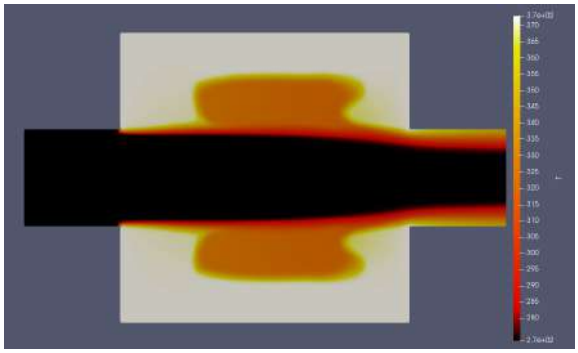

(f) temperature, c = 100

Figure 6.9: Porosity and temperature fields of generated heat sinks for constant c values.

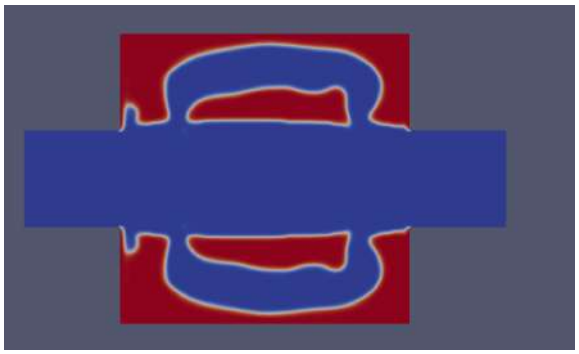

(a) porosity, c = table 1

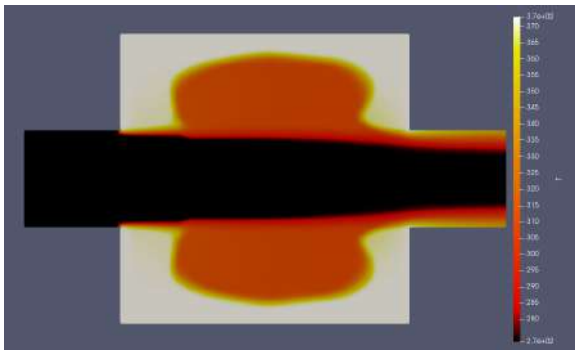

(b) temperature, c = table 1

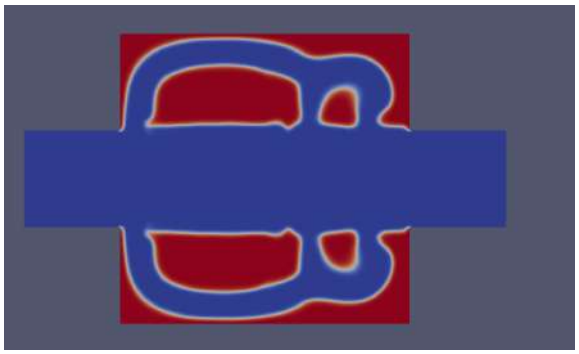

(c) porosity, c = table 2

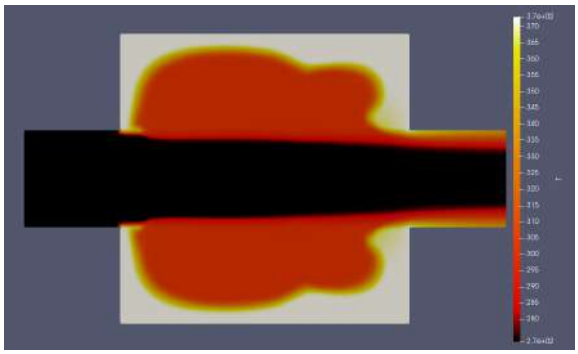

(d) temperature, c = table 2

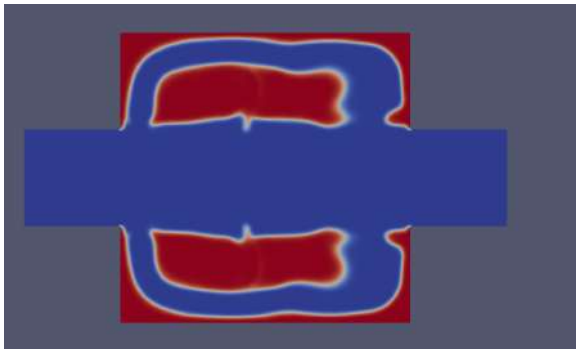

(e) porosity, c = table 3

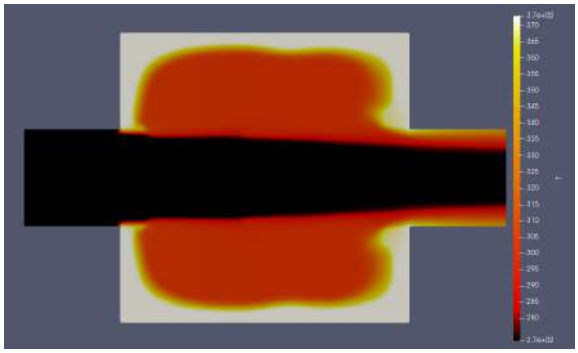

(f) temperature, c = table 3

Figure 6.10: Porosity and temperature fields of generated heat sinks for varying c values.

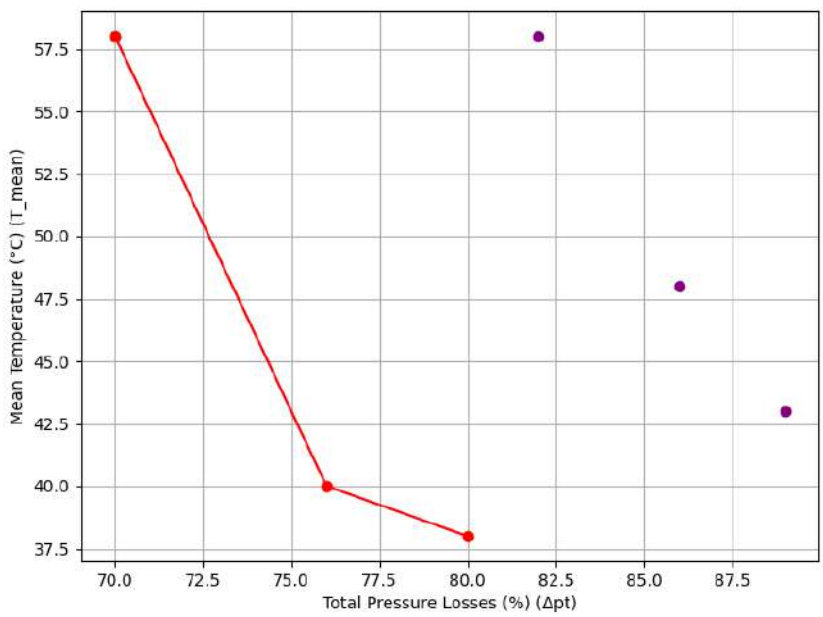

Figure 6.11: The Pareto front for the dominating solutions of the CHT cases from Chapter 5 is shown. The red-colored solutions represent the dominating outcomes generated using the third version of the objective function, with weights of 0.80 and 0.20 assigned to mean temperature and total pressure losses, respectively. The purple-colored points highlight the top three best solutions from the first and second sets of runs.

Chapter 7

Summary - Conclusion

This thesis explored the challenges and methodologies for handling infeasibilities in Computational Fluid Dynamics (CFD) optimization problems, focusing on topology optimization (TopO) and shape optimization (ShpO) within the Sequential Quadratic Programming (SQP) framework. The study highlighted the role of the additional design variables multiplier's value in addressing infeasibility and influencing the convergence behavior of optimization processes.

The analysis demonstrated that its value significantly affects the optimization trajectory, particularly in 2D TopO problems, where a default multiplier value of $c = 100$, based on the original MMA paper, led to impractical geometries or oscillatory convergence. Decreasing the multiplier dynamically across iterations was shown to produce smoother optimization paths in some test cases and improved solutions. In contrast, 3D TopO problems exhibited greater robustness to the multiplier's value, with the default setting achieving feasible solutions more consistently. Decreasing the factor's values was shown in one of the two cases to produce better solutions.

In ShpO problems, the influence of the multiplier was less pronounced compared to TopO problems, yet still played a role in convergence speed and objective's value in the Stator's Blade case in which the infeasibility located in the targeted exit flow angle constraint.

For conjugate heat transfer (CHT) TopO problems, no safe consensus can be extracted, as both constant and varying factor's values lead to the best results in the three test cases.

Bibliography

[1] *H. Hajdik, B. Pacini, A. Yildirim, B. Brelje, and J. Martins. Combined systems packaging and aerodynamic shape optimization of a full aircraft configuration. In AIAA Aviation 2023 Forum, 2023.*

[2] *C. Othmer. Adjoint methods for car aerodynamics. Journal of Mathematics in Industry, 4(6), 2014.*

[3] *E. Papoutsis-Kiachagias, V. Asouti, K. Giannakoglou, K. Gkagkas, S. Shimokawa, and E. Itakura. Multi-point aerodynamic shape optimization of cars based on continuous adjoint. Structural and Multidisciplinary Optimization, 59(2):675–694, 2019.*

[4] *H. Wu, X. Da, D. Wang, and X. Huang. Multi-row turbomachinery aerodynamic design optimization by an efficient and accurate discrete adjoint solver. Aerospace, 10(2), 2023.*

[5] *M. P. Bendsoe, O. Sigmund, Topology optimization: theory, methods, and applications, Springer Science Business Media, 2013.*

[6] *P. Y. Vrionisa, K. D. Samouchosa, K. C. Giannakoglou, Topology Optimization in Fluid Mechanics using Continuous Adjoint and the Cut-cell Method (2022).*

[7] *M. P. Bendsøe, N. Kikuchi, Generating optimal topologies in structural design using a homogenization method, Computer Methods in Applied Mechanics and Engineering 71 (2) (1988) 197 – 224.*

[8] *T. Borrvall, J. Petersson, Topology optimization of fluids in Stokes flow, International Journal for Numerical Methods in Fluids 41 (1) (2003) 77– 107.*

[9] *C. Othmer, A continuous adjoint formulation for the computation of topological and surface sensitivities of ducted flows, International Journal for Numerical Methods in Fluids 58 (8) (2008) 861–877.*

[10] *G. Liu, M. Geier, Z. Liu, M. Krafczyk, T. Chen, Discrete adjoint sensitivity analysis for fluid flow topology optimization based on the generalized lattice Boltzmann method, Computers Mathematics with Applications 68 (10) (2014) 1374–1392.*

[11] *E. Kontoleontos, E. Papoutsis-Kiachagias, A. Zymaris, D. Papadimitriou,K. Giannakoglou, Adjoint-based constrained topology optimization for viscous flows, including heat transfer, Engineering Optimization 45 (8) (2013).*

[12] *C. B. Dilgen, S. B. Dilgen, D. R. Fuhrman, O. Sigmund, B. S. Lazarov, Topology optimization of turbulent flows, Computer Methods in Applied Mechanics and Engineering 331 (2018) 363–393.*

[13] *Y. Deng, Z. Liu, P. Zhang, Y. Liu, Y. Wu, Topology optimization of unsteady incompressible Navier–Stokes flows, Journal of Computational Physics 230 (17) (2011) 6688–6708.*

[14] *C. H. Villanueva, K. Maute, CutFEM topology optimization of 3D laminar incompressible flow problems, Computer Methods in Applied Mechanics and Engineering 320 (2017) 444–473.*

[15] *T. Nguyen, H. Isakari, T. Takahashi, K. Yaji, M. Yoshino, T. Matsumoto, Level-set based topology optimization of transient flow using lattice Boltzmann method considering an oscillating flow condition, Computers Mathematics with Applications 80 (1) (2020) 82–108.*

[16] *S. Kreissl, K. Maute, Levelset based fluid topology optimization using theextended finite element method, Structural and Multidisciplinary Optimization 46 (3) (2012) 311–326.*

[17] *C. Lundgaard, J. Alexandersen, M. Zhou, C. S. Andreasen, O. Sigmund, Revisiting density-based topology optimization for fluid-structure-interaction problems, Structural and Multidisciplinary Optimization 58 (3) (2018) 969–995.*

[18] *J. Koch, E. Papoutsis-Kiachagias, K. Giannakoglou, Transition from adjoint level set topology to shape optimization for 2D fluid mechanics, Computers Fluids 150 (2017) 123–138.*

[19] *N. Jenkins, K. Maute, Level set topology optimization of stationary fluid-structure interaction problems, Structural and Multidisciplinary Optimization 52 (1) (2015) 179–195.*

[20] *T. Vu-Huu, P. Phung-Van, H. Nguyen-Xuan, M. A. Wahab, A polytree-based adaptive polygonal finite element method for topology optimization of fluid-submerged breakwater interaction, Computers Mathematics with Applications 76 (5) (2018) 1198–1218.*

[21] *V. J. Challis, J. K. Guest, Level set topology optimization of fluids in Stokes flow, International Journal for Numerical Methods in Engineering 79 (10) (2009) 1284–1308.*

[22] *X. Duan, F. Li, X. Qin, Topology optimization of incompressible Navier– Stokes problem by level set based adaptive mesh method, Computers Mathematics with Applications 72 (4) (2016) 1131–1141.*

[23] *N. P. van Dijk, K. Maute, M. Langelaar, F. Van Keulen, Level-set methods for structural topology optimization: a review, Structural and Multidisciplinary Optimization 48 (3) (2013) 437–472.*

[24] *L. S´a, R. Amigo, A. Novotny, E. Silva, Topological derivatives applied to fluid flow channel design optimization problems, Structural and Multidisciplinary Optimization 54 (2) (2016) 249–264.*

[25] *N. Galanos, Topology and Shape Optimization in Fluid Mechanics Conjugate Heat Transfer using Continuous Adjoint with Consistent Discretization, 2025.*

[26] *Andreas-Stefanos I. Margetis, Kyriakos C. Giannakoglou, PhD Thesis: Unsteady RANS (D)DES Continuous Adjoint and Compression Techniques in Aerodynamic Shape Optimization (2024).*

[27] *T. Bäck. Evolutionary algorithms in theory and practice: Evolution strategies, evolutionary programming, genetic algorithms. Oxford University Press, 02 1996.*

[28] *D. Sudholt. Parallel evolutionary algorithms, pages 929–959. Springer Berlin Heidelberg, Berlin, Heidelberg, 2015.*

[29] *F. Herrera, M. Lozano, and C. Moraga. Hierarchical distributed genetic algorithms. International Journal of of Intelligent Systems, 14(9):1099–1121, 1999.*

[30] *K. Giannakoglou. Design of optimal aerodynamic shapes using stochastic optimization methods and computational intelligence. Progress in Aerospace Sciences, 38(1):43–76, 2002.*

[31] *M. El-Beltagy, P. Nair, and A. Keane. Metalmodeling techniques for evolutionary optimization of computationally expensive problems: Promises and limitations. In Proceedings of the Genetic and Evolutionary Computation Conference (GECCO-99), pages 196–203, 1999.*

[32] *J. Nocedal and S. Wright. Numerical optimization. Springer, New York, USA, 2e edition, 2006.*

[33] *J. Peter and R. Dwight. Numerical sensitivity analysis for aerodynamic optimization: A survey of approaches. Computers Fluids, 39(3):373–391, 2010.*

[34] *D. Papadimitriou and K. Giannakoglou. Third-order sensitivity analysis for robust aerodynamic design using continuous adjoint. International Journal for Numerical Methods in Fluids, 71(5):652–670, 2013.*

[35] *E. Papoutsis-Kiachagias, V. Asouti, K. Giannakoglou, K. Gkagkas, S. Shimokawa, and E. Itakura. Multi-point aerodynamic shape optimization of cars based on continuous adjoint. Structural and Multidisciplinary Optimization, 59(2):675–694, 2019.*

[36] *B. Zhou, T. Albring, N. Gauger, T. Economon, F. Palacios, and J. Alonso. A discrete adjoint framework for unsteady aerodynamic and aeroacoustic optimization. In 16th AIAA/ISSMO Multidisciplinary Analysis and Optimization Conference, 06 2015.*

[37] *C. Broyden. The convergence of a class of double-rank minimization algorithms 1. General considerations. IMA Journal of Applied Mathematics, 6(1):76–90, 03 1970.*

[38] *R. Byrd, H. Khalfan, and R. Schnabel. Analysis of a symmetric rank-one trust region method. SIAM Journal on Optimization, 6(4):1025–1039, 1996.*

[39] *R. Fletcher and C. Reeves. Function minimization by conjugate gradients. The Computer Journal, 7(2):149–154, 1964.*

[40] K. Svanberg. The method of moving asymptotes—a new method for structural optimization. *International Journal for Numerical Methods in Engineering*, 24:359–373, 1987.

[41] N. Aage and O. Sigmund. Topology optimization of laminar incompressible flows. *Computers and Fluids*, 107:121–136, 2013.

[42] M. Stolpe and K. Svanberg. On the convergence of mma and some extensions. *Structural and Multidisciplinary Optimization*, 21:116–126, 2001.

[43] O. Sigmund and K. Maute. Topology optimization approaches: A comparative review. *Structural and Multidisciplinary Optimization*, 48:1031–1055, 2013.

[44] T. Borrvall and J. Petersson. Topology optimization of fluids in stokes flow. *International Journal for Numerical Methods in Fluids*, 41:77–107, 2001.

[45] J. Nocedal and S. J. Wright. *Numerical Optimization.* Springer, 2006.

[46] W. Murray P. E. Gill and M. H. Wright. Practical optimization. *Academic Press*, 1981.

[47] B. J. Ramm K. U. Bletzinger, F. L. Darwich and R. Wüchner. Shape optimization and sensitivity analysis. *Computational Mechanics*, 57:565–583, 2016.

Εθνικό Μετσόβιο Πολυτεχνείο
Σχολή Μηχανολόγων Μηχανικών
Τομέας Ρευστών
Μονάδα Παράλληλης Υπολογιστικής Ρευστοδυναμικής
& Βελτιστοποίησης

Συμβολή στη διαχείριση περιορισμών σε προβλήματα βελτιστοποίησης μορφής και τοπολογίας στην Υπολογιστική Ρευστοδυναμική

Διπλωματική Εργασία - Εκτενής Περίληψη στα Ελληνικά

Όθων Βαλεράς

Επιβλέπων: Κυριάκος Χ. Γιαννάκογλου, Καθηγητής ΕΜΠ

Αθήνα, Φεβρουάριος 2025

Εισαγωγή

Πρωταρχικός στόχος αυτής της διπλωματικής εργασίας, είναι η αντιμετώπιση προβλημάτων ανεφικτότητας των περιορισμών στη βελτιστοποίηση μορφής και τοπολογίας, αξιοποιώντας μια μέθοδο Διαδοσχικού Τετραγωνικού Προγραμματισμού (Sequential Quadratic Programming SQP) επαυξημένη με επιπλέον μεταβλητές σχεδιασμού. Οι τελευταίες χαλαρώνουν τους περιορισμούς και προστίθενται στην αντικειμενική συνάρτηση, επιβαρύνοντάς την όταν ένας περιορισμός δεν ικανοποιείται. Στην επαυξημένη συνάρτηση, το σχετικό βάρος μεταξύ αρχικής αντικειμενικής συνάρτησης και επιπλέον όρων, ελέγχεται από μία παράμετρο που παίζει καθοριστικό ρόλο στην πορεία σύγκλισης και στην τελική λύση που παράγει ο αλγόριθμος βελτιστοποίησης.

Η SQP εφαρμόζεται χρησιμοποιώντας το λογισμικό βελτιστοποίησης του OpenFOAM σε διάφορα προβλήματα μορφής και τοπολογίας, σε 2Δ και 3Δ γεωμετρίες. Σε όλες τις εφαρμογές δοκιμάζονται διαφορετικές αρχικοποιήσεις της μεθόδου, ώστε να εξαχθούν συμπεράσματα για την επίδραση που έχει το σχετικό βάρος των δύο όρων της αντικειμενικής συνάρτησης, στην τελική λύση.

Αλγόριθμος SQP

Όλα τα προβλήματα που παρουσιάζονται στη διπλωματική εργασία εμπεριέχουν περιορισμούς ανισότητας. Όλοι οι περιορισμοί ισότητας έχουν διαμορφωθεί κατάλληλα ώστε να περιγράφονται με χρήση ανισοτήτων. Η μέθοδος SQP που χρησιμοποιήθηκε παρουσιάζεται στην απλή εφαρμογή όπου μόνο ένας περιορισμός g δεσμεύει τις μεταβλητές σχεδιασμού x, της αντικειμενικής συνάρτησης f. Το πρόβλημα έχει την ακόλουθη μορφή:

$$\begin{aligned} &\min_{x \in \Re^n} \; f(x) \\ &\text{s.t.} \quad g(x) \leq 0 \end{aligned} \tag{7.1}$$

Αφού λυθεί το ευθύ και το συζυγές πρόβλημα στον τωρινό κύκλο υπολογίζονται οι τιμές της αντικειμενικής συνάρτησης, f_k, των παραγώγων αυτής, ∇f_k, και του περιορισμού, ∇g_k, και μια προσέγγιση του εσσιανού μητρώου, H_k, χρησιμοποιώντας μια μέθοδο όπως η BFGS. Στην συνέχεια κατασκευάζεται το τετραγωνικό πρόβλημα που προσεγγίζει το αρχικό στην περιοχή γύρω από την τωρινή θέση, x_k, των μεταβλητών σχεδιασμού. Το προσεγγιστικό πρόβλημα γράφεται ως εξής:

$$\begin{aligned} &\min_{p_x \in \Re^n} \tilde{f}(p_x) \\ &\text{s.t.} \;\; \tilde{g}(p_x) \;\; \leq 0 \end{aligned} \tag{7.2}$$

όπου

$\tilde{f}(p_x) \;=\; f_k + \nabla f_k^T p_x + \frac{1}{2} p_x^T H_k p_x$, η τετραγωνική προσέγγιση της αντικειμενικής συνάρτησης και

$\tilde{g}(p_x) \;=\; g_k + \nabla g_k^T p_x$ η γραμμική προσέγγιση του περιορισμού αντίστοιχα.

Στη βελτιστοποίηση CFD, όπου οι αντικειμενικές συναρτήσεις και οι συναρτήσεις των περιορισμών δεν είναι γνωστές αναλυτικά, η αρχικοποίηση των μεταβλητών σχεδιασμού x στο τετραγωνικό πρόβλημα (QP) ενδέχεται να μην ικανοποιεί τους περιορισμούς του προβλήματος, οδηγώντας έτσι τον αλγόριθμο SQP σε αποτυχία από την αρχή. Περιορισμοί που δεν ικανοποιούνται ονομάζονται μη εφικτοί περιορισμοί (infeasible constraints). Σε αυτή τη διπλωματική εργασία, ο όρος μη εφικτότητα (infeasibility) αναφέρεται πάντοτε στο τετραγωνικό πρόβλημα και όχι στο αρχικό πρόβλημα, εκτός αν δηλώνεται ρητά το αντίθετο.

Η μη εφικτότητα εμφανίζεται συχνά στη βελτιστοποίηση τοπολογίας (TopO) στον αρχικό κύκλο της διαδικασίας, λόγω του περιορισμού που σχετίζεται με τον όγκο. Για να ξεπεραστούν αυτά τα ζητήματα, ο γραμμικοποιημένος περιορισμός $\tilde{g}$ χαλαρώνεται μέσω της εισαγωγής μιας μη αρνητικής, βοηθητικής μεταβλητής y, η οποία ενσωματώνεται στην προσεγγιστική αντικειμενική συνάρτηση $\tilde{f}$ με έναν συντελεστή βαρύτητας c, σχηματίζοντας το υποχαλαρωμένο πρόβλημα (7.3):

$$\begin{aligned} \min_{p_x \in \Re^n,\ y \in \Re} \; & \tilde{f}(p_x) + cy \\ \text{s.t. } & \tilde{g}(p_x) - y \leq 0 \\ & -y \leq 0 \end{aligned} \tag{7.3}$$

Στο τροποποιημένο πρόβλημα (7.3), υπάρχει πάντα μια θετική τιμή του y που ικανοποιεί τον ενισχυμένο περιορισμό, ακόμα και αν το $\tilde{g}(p_x)$ είναι μη εφικτό, δηλαδή όταν $\tilde{g}(p_x) > 0$. Φυσικά, εάν το πρόβλημα (7.3) γίνει εφικτό, η πρόσθετη μεταβλητή y θα μηδενιστεί, αποκτώντας μη μηδενική τιμή μόνο όταν οι μεταβλητές σχεδιασμού δεν ικανοποιούν τον περιορισμό $\tilde{g}$. Συνεπώς, ο αλγόριθμος βελτιστοποίησης μετατοπίζει την εστίασή του από την αποκλειστική ελαχιστοποίηση της αρχικής αντικειμενικής συνάρτησης f η $\tilde{f}$ στη μείωση της μεταβλητής y, προσαρμόζοντας έτσι τις μεταβλητές σχεδιασμού x ώστε να αποκατασταθεί η ικανοποίηση των περιορισμών.

Ο συντελεστής βαρύτητας c ελέγχει την επίδραση των περιορισμών στην αντικειμενική συνάρτηση. Μεγαλύτερες τιμές του c αυξάνουν την επιρροή της πρόσθετης μεταβλητής y_m στην επαυξημένη αντικειμενική συνάρτηση και ωθούν τον αλγόριθμο να κατευθύνει πιο επιθετικά τις μεταβλητές σχεδιασμού προς την περιοχή ικανοποίησης των περιορισμών, εξασφαλίζοντας ταχύτερη ικανοποίηση των περιορισμών. Ωστόσο, αυτό ενέχει τον κίνδυνο σύγκλισης σε περιοχές με σχετικά υψηλές τιμές της αντικειμενικής συνάρτησης. Αντίθετα, μικρότερες τιμές του c επιτρέ-

πουν στις μεταβλητές σχεδιασμού να εξερευνήσουν καλύτερες περιοχές ως προς την τιμή της αντικειμενικής συνάρτησης, αλλά μπορεί να καθυστερήσουν την ικανοποίηση των περιορισμών. Αν και το c διατηρείται συνήθως σταθερό, σε ορισμένες περιπτώσεις μπορεί να είναι ωφέλιμο να μεταβάλλεται σε κάθε επανάληψη. Οι μεταβαλλόμενες τιμές του c κατά τη διάρκεια των κύκλων βελτιστοποίησης μπορούν να οδηγήσουν τον αλγόριθμο SQP σε διαφορετικές τελικές λύσεις, όπως και παρουσιάζεται στα επόμενα κεφάλαια.

Για την απόκτηση των αναγκαίων συνθηκών βέλτιστης λύσης KKT για το υποπρόβλημα (7.3), προστίθεται η θετική μεταβλητή χαλάρωσης g_s στον περιορισμό, μετατρέποντάς τον σε περιορισμό ισότητας. Οι δύο εναπομείναντες, απλούστεροι περιορισμοί ανισότητας, $y \geq 0$ και $g_s \geq 0$, εξαλείφονται ενσωματώνοντάς τους στους λογαριθμικούς όρους, οι οποίοι προστίθενται στην αντικειμενική συνάρτηση, μετατρέποντας έτσι το πρόβλημα (7.3) στο τελικό:

$$\begin{aligned} \min_{p_x \in \Re^n,\ y \in \Re,\ g_s \in \Re} \quad & \tilde{f}(p_x) + cy - \epsilon log(y) - \epsilon log(g_s) \\ \text{s.t. } & G(p_x, y, g_s) = \tilde{g}(p_x) - y + g_s = 0 \end{aligned} \tag{7.4}$$

όπου το ϵ είναι ένας θετικός βαθμωτός αριθμός, γνωστός ως παράμετρος φραγμού (barrier parameter).

Παρατηρούμε ότι καθώς οι g_s και y πλησιάζουν το μηδέν (από θετικές τιμές, δηλαδή από τον εφικτό χώρο), οι αρνητικοί όροι του φραγμού τείνουν στο άπειρο. Αυτό προφανώς επιβαρύνει την αντικειμενική συνάρτηση και εξαναγκάζει τον αλγόριθμο να διατηρεί το g_s θετικό. Ο αλγόριθμος εσωτερικού σημείου (IP) επιλύει, σε κάθε κύκλο βελτιστοποίησης, μια ακολουθία υποπροβλημάτων της εξίσωσης (7.4) για ένα διαδοχικά μειούμενο σύνολο παραμέτρων φραγμού ϵ.

Η συνάρτηση Lagrange του προβλήματος (7.4) ορίζεται ως:

$$L(p_x, y, \lambda, g_s) = \tilde{f}(p_x) + cy - \epsilon \log(y) - \epsilon \log(g_s) - \lambda G(p_x, y, g_s) \tag{7.5}$$

όπου το λ είναι ο μη αρνητικός πολλαπλασιαστής Lagrange του περιορισμού ισότητας στο πρόβλημα (7.3).

Οι συνθήκες KKT του υποπροβλήματος (7.4), διατυπώνονται ως εξής:

$$
\begin{aligned}
&F_{L,x}(p_x, y, \lambda, \mu, g_s) = \nabla \tilde{f} - \lambda \nabla \tilde{g} = H_k p_k + \lambda \nabla g_k = 0 \\
&F_{L,y}(p_x, y, \lambda, \mu, g_s) = cy - \lambda y - \epsilon = 0 \\
&F_{\lambda}(p_x, y, \lambda, \mu, g_s) = \tilde{g}(p_x) - y + g_s = g_k + \nabla g_k p_k + gs - y = 0 \\
&F_{g_s}(p_x, y, \lambda, \mu, g_s) = \lambda g_s + \epsilon = 0
\end{aligned} \tag{7.6}
$$

Η λύση του συστήματος (7.6), δηλαδή το διάνυσμα $(p'_x, y', \lambda', g'_s)$, δίνεται από:

$$
\begin{aligned}
p'_x &= p_x + \delta p_x \\
y' &= y + \delta y \\
\lambda' &= \lambda + \delta \lambda \\
g'_s &= g_s + \delta g_s
\end{aligned} \tag{7.7}
$$

όπου οι διορθώσεις υπολογίζονται μέσω της επίλυσης του γραμμικού συστήματος:

$$
\begin{pmatrix} H_k & 0 & \nabla g_k^T & 0 \\ 0 & c+\lambda & y & -1 \\ \nabla g_k^T & -1 & 0 & 1 \\ 0 & 0 & g_s & \lambda \end{pmatrix} \begin{pmatrix} \delta p_x \\ \delta y \\ \delta \lambda \\ \delta g_s \end{pmatrix} = - \begin{pmatrix} F_{L,x} \\ F_{L,y} \\ F_{\lambda} \\ F_{g_s} \end{pmatrix} \tag{7.8}
$$

Το σύστημα (7.8) επιλύεται διαδοχικά για προοδευτικά μειούμενες τιμές της ϵ, έως ότου επιτευχθεί μια απαιτούμενη μικρή τιμή. Μετά από αυτό, ξεκινά ο επόμενος κύκλος βελτιστοποίησης.

Το διάγραμμα επίλυσης του προβλήματος βελτιστοποίησης σε κάθε βήμα παρουσιάζεται στον Αλγόριθμο 3:

Algorithm 3 Αλγόριθμος SQP

1: Επίλυση των του primal και του adjoint προβλήματος και υπολογισμός των παραγώγων ευαισθησίας και του εσσιανού μητρώου
2: Αρχικοποίηση του ϵ
3: **while** δεν ικανοποιούνται τα κριτήρια σύγκλισης **do**
4: Επίλυση KKT και υπολογισμός κατεύθυνσης ενημέρωσης μεταβλητών σχεδιασμού
5: Ανίχνευση κατά γραμμή και ενημέρωση μεταβλητών σχεδιασμού
6: Μείωση του ϵ
7: **end while**
8: Αρχή επόμενου κύκλου βελτιστοποίησης

Ο πολλαπλασιαστής των επιπλέον μεταβλητών σχεδιασμού, c (βλ. αντικειμενική συνάρτηση στο πρόβλημα (7.3)), ελέγχει την επίδραση της μη ικανοποίησης των περιορισμών στη διευρυμένη

αντικειμενική συνάρτηση και διαδραματίζει σημαντικό ρόλο στη σύγκλιση ενός προβλήματος βελτιστοποίησης με περιορισμούς.

Λαμβάνοντας αυτό υπόψη, ο κύριος στόχος αυτής της διπλωματικής εργασίας είναι η αναζήτηση της καταλληλότερης επιλογής του όρου περιορισμού στην εμπλουτισμένη αντικειμενική συνάρτηση του προβλήματος (7.3) που χρησιμοποιείται στον αλγόριθμο SQP, για προβλήματα 2D, 3D, TopO και ShpO. Στο πλαίσιο αυτής της προσπάθειας, δοκιμάστηκαν σταθερές και μεταβαλλόμενες τιμές του c, με τις τελευταίες να εμφανίζουν (σε πολλές περιπτώσεις) βελτιωμένα αποτελέσματα, όπως θα παρουσιαστεί στην επόμενη ενότητα.

Εφαρμογή SQP και Αντιμετώπιση Ανεφικτότητας σε 2D TopO πρόβλημα

Το ακόλουθο TopO πρόβλημα, αφορά ένα στρωτό πρόβλημα με 1 είσοδο και 2 εξόδους, όπου ο αριθμός Reynolds, βασισμένος στο ύψος της εισόδου, είναι $Re = 200$. Η αντικειμενική συνάρτηση που χρησιμοποιείται είναι οι συνολικές απώλειες ολικής πίεσης μεταξύ της εισόδου και των εξόδων, κανονικοποιημένες ως προς την αρχική τιμή. Το πεδίο ψευδοπυκνότητας (density or poroscity field) αρχικοποιείται σε 0 σε κάθε κελί, που σημαίνει ότι ολόκληρος ο όγκος καταλαμβάνεται αρχικά από ρευστό. Ο μόνος περιορισμός είναι ο περιορισμός του καταλαμβανόμενου όγκου από ρευστό, με στόχο το 46.2% του υπολογιστικού πεδίου. Οι οριακές συνθήκες που χρησιμοποιούνται για τα πρωταρχικά πεδία παρουσιάζονται στον Πίνακα (7.1).

Περιοχή	**Ταχύτητα U**	**Πίεση p**
Είσοδος	(1,0) (Dirichlet)	μηδενική κλίση (Neumann)
Έξοδοι	μηδενική κλίση (Neumann)	0 (Dirichlet)
Οριακά τοιχώματα περιοχής	(0,0) (Dirichlet)	μηδενική κλίση (Neumann)

Table 7.1: Οριακές συνθήκες του πρωτεύοντος προβλήματος για την 2D στρωτή περίπτωση 1, με 1 είσοδο και 2 εξόδους.

Στο Σχήμα 7.1, παρουσιάζεται η γεωμετρία του αγωγού για τέσσερις επαναλήψεις, συμπεριλαμβανομένης της τελικής, για τρεις διαφορετικές εκτελέσεις του προβλήματος με $c = 1$, 5 και 100. Οι τιμές της αντικειμενικής συνάρτησης και του περιορισμού, για 100 επαναλήψεις του κύκλου βελτιστοποίησης, παρουσιάζονται στο Σχήμα 7.2.

Όπως αναμενόταν, ο ρυθμός μείωσης του περιορισμού είναι ανάλογος της τιμής του c, γεγονός που μπορεί να παρατηρηθεί στο Σχήμα 7.3. Αυτό φαίνεται περαιτέρω στη θέση των στερεών οριακών γραμμών στο Σχήμα 7.2. Συγκεκριμένα, η 'μωβ' γραμμή, που αντιστοιχεί στο $c = 100$, κινείται σημαντικά ταχύτερα από τις άλλες δύο, ώστε να περικλείσει το μέγιστο ποσοστό όγκου

ρευστού του περιορισμού, δηλαδή 46.2%. Ο ρυθμός με τον οποίο επιτυγχάνεται η εφικτότητα είναι τόσο γρήγορος που το μονοπάτι προς τη δεξιά έξοδο στερεοποιείται, παραμένοντας έτσι για το υπόλοιπο του κύκλου βελτιστοποίησης. Αυτό δείχνει ότι η προεπιλεγμένη τιμή $c = 100$ δεν είναι κατάλληλη για αυτό το πρόβλημα. Αντίθετα, οι κύκλοι με $c = 1$ και 5 καταλήγουν σε μια λύση με συνολική μείωση της αντικειμενικής συνάρτησης κατά 26%.

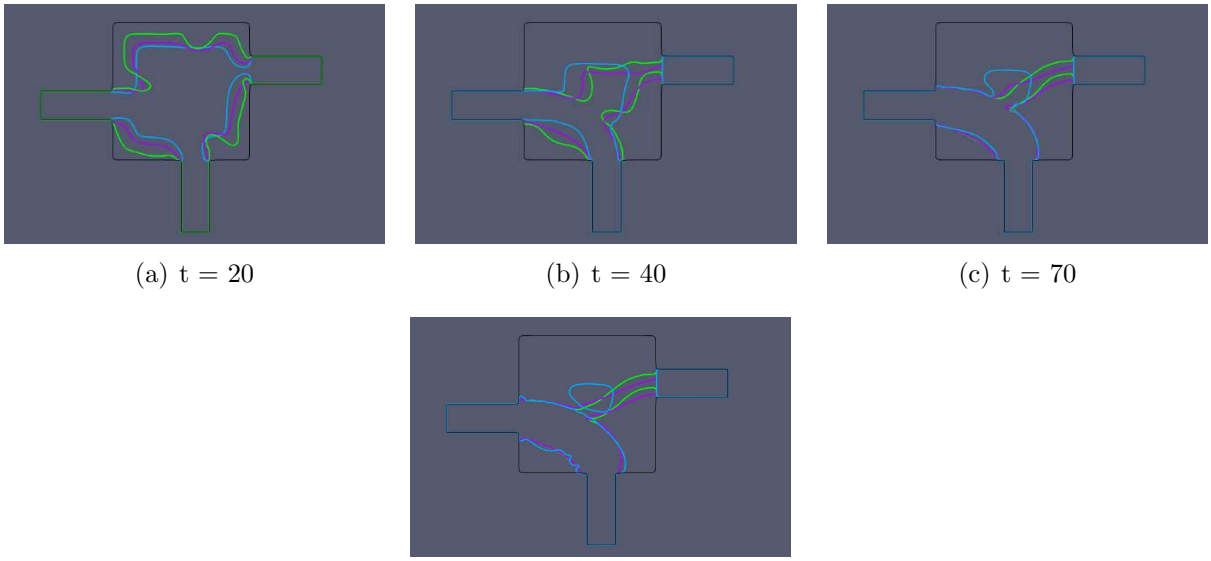

(a) t = 20 (b) t = 40 (c) t = 70

(d) t = 100

Σχήμα 7.1: Η εξελισσόμενη γεωμετρία του αγωγού στην του 2D TopO προβλήματος στους κύκλους 20, 40, 70, 100. Η αρχική περιοχή που καταλαμβάνεται πλήρως από ρευστό απεικονίζεται με μαύρο χρώμα, η γεωμετρία για $c = 1$ με πράσινο, η γεωμετρία για $c = 5$ με μωβ και η γεωμετρία για $c = 100$ με μπλε.

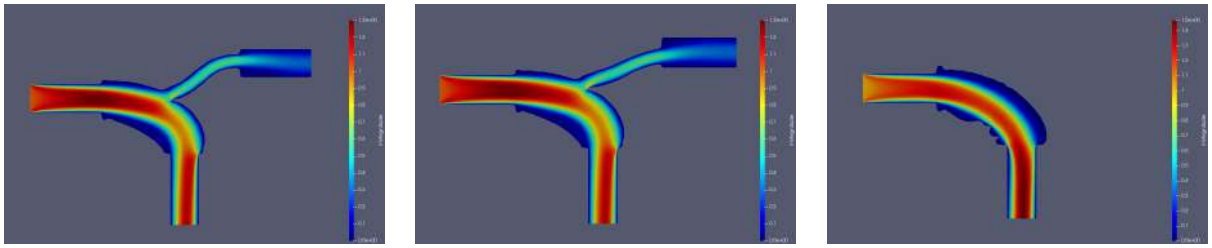

(a) c = 1 (b) c = 5 (c) c = 100

Σχήμα 7.2: Πεδία ταχυτήτων για τις τελικές γεωμετρίες στο 2D TopO πρόβλημα $c = 1, 5, 100$.

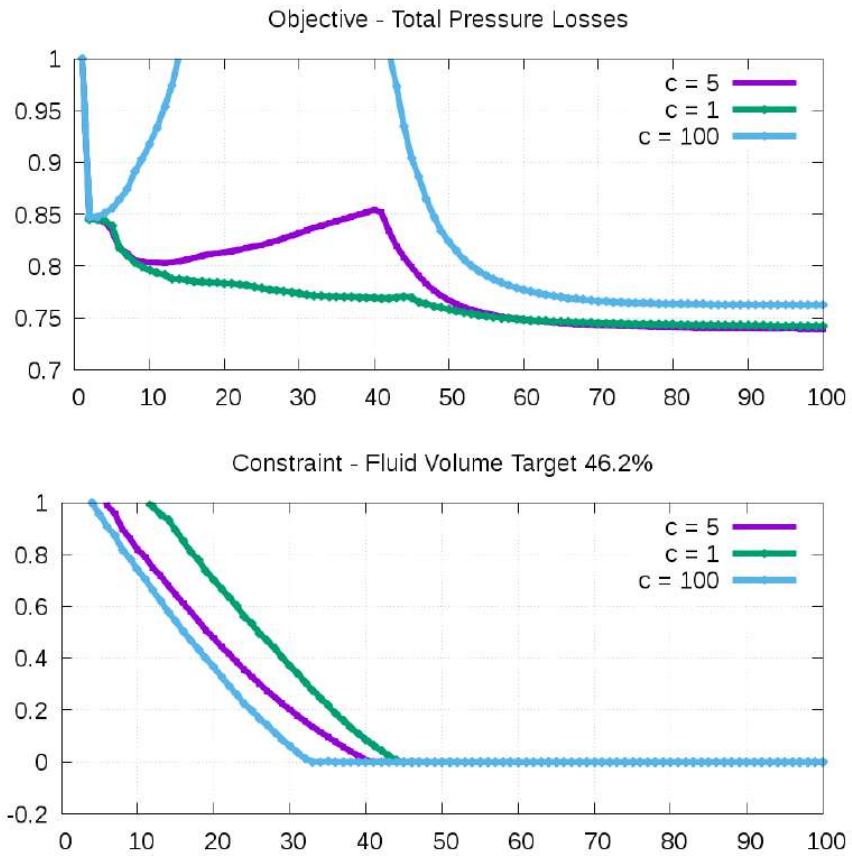

Σχήμα 7.3: Σύγκλιση αντικειμενικής συνάρτησης - ολικές πτώσεις πίεσης και περιορισμού όγκου στπ 2D TopO πρόβλημα για $c = 1, 5, 100$.

Εφαρμογή SQP και Αντιμετώπιση Ανεφικτότητας σε 3D TopO πρόβλημα

Το επόμενο πρόβλημα αφορά τον σχεδιασμό ενός κλιματιστικού αεραγωγού αυτοκινήτουπου με 1 είσοδο και 3 εξόδου και τυρβώδη ροή όπου ο αριθμός Reynolds, βασισμένος στο ύψος της εισόδου, είναι $Re = 50,000$. Η αντικειμενική συνάρτηση που χρησιμοποιείται είναι ο δείκτης ομοιομορφίας ροής στις τρεις εξόδους, κανονικοποιημένος ως προς την αρχική του τιμή. Το πεδίο ψευδοπυκνότητας αρχικοποιείται σε 0.5 σε κάθε κελί.

Υπάρχουν 3 περιορισμοί σε αυτό το πρόβλημα:
- ένας στόχος συνολικών απωλειών πίεσης ίσος με 20 Pa,
- ένας περιορισμός όγκου ρευστού στο 15%, και
- κατανομές μαζικών ροών στις εξόδους ίσες με 33-33-33%.

Το υπολογιστικό πλέγμα, και συνεπώς το διάνυσμα μεταβλητών σχεδιασμού, αποτελείται από 109.960 στοιχεία. Για την ταχύτητα στην είσοδο, χρησιμοποιείται μια σταθερή τιμή, υπολογισ-

μένη ώστε να αντιστοιχεί σε σταθερή παροχή όγκου 0.05 m^3/s. Στις εξόδους, εφαρμόζεται μια μικτή συνοριακή συνθήκη, με μηδενική κλίση για εκροή και τιμή 0 για εισροή. Χρησιμοποιείται μια συνάρτηση τοιχώματος για τον υπολογισμό της $\tilde{\nu}$ στα κελιά που γειτνιάζουν με τα τοιχώματα. Οι οριακές συνθήκες για τα πρωτεύοντα πεδία παρουσιάζονται στον Πίνακα (7.2).

Περιοχή	**Ταχύτητα U**	**Πίεση p**	$\tilde{\nu}$
Είσοδος	* (Dirichlet)	μηδενική κλίση	0.0001 (Dirichlet)
Έξοδοι	* μικτή	0 (Dirichlet)	μηδενική κλίση
Οριακά τοιχώματα περιοχής	(0,0,0) (Dirichlet)	μηδενική κλίση (Neumann)	-

Table 7.2: Οριακές συνθήκες του πρωτεύοντος προβλήματος για την 3D συμμετρική, τυρβώδη περίπτωση 4, με 1 είσοδο και 3 εξόδους. Το $\vec{n}$ αντιπροσωπεύει το μοναδιαίο διανυσματικό πεδίο κάθετης διεύθυνσης στην αντίστοιχη επιφάνεια.

Για τις τιμές $c = 2$ και $c = 5$, οι συζυγείς εξισώσεις αποτυγχάνουν να συγκλίνουν μετά τη δεύτερη επανάληψη. Ο κύκλος με $c = 100$ παράγει λύση, αν και λόγω της προβληματικής σύγκλισης του συζυγούς πεδίου ταχύτητας για την αντικειμενική συνάρτηση ομοιομορφίας, παρουσιάζεται ξαφνική αλλαγή στη γεωμετρία του αγωγού στη 32η επανάληψη, γεγονός που επιδεινώνει την τελική λύση.

Εκτελέστηκαν επίσης τρεξίματα με μεταβλητές τιμές του c και συγκεκριμένα:

- γραμμική αύξηση του c, με τους κύκλους βελτιστοποίησης, $c = 100 + t$
- γραμμική μείωση του c, με τους κύκλους βελτιστοποίησης, $c = 100 - 2t$
- τετραγωνική αύξηση του c, με τους κύκλους βελτιστοποίησης, $c = 100 + 0.04t^2$
- τετραγωνική μείωση του c, με τους κύκλους βελτιστοποίησης, $c = 100 - 0.04t^2$

Παρατηρείται μια ξαφνική μεταβολή ξανά στην επανάληψη 32 για την γραμμικά μειούμενη τιμή του c και στην επανάληψη 45 για την τετραγωνικά αυξανόμενη τιμή του c. Προέκυψαν διαφορετικές εφικτές λύσεις για κάθε εκτέλεση, με τα καλύτερα αποτελέσματα να επιτυγχάνονται χρησιμοποιώντας γραμμικά και τετραγωνικά μειούμενες τιμές του c. Ωστόσο, η τρίτη εκτέλεση με μειούμενες τιμές δεν έφτασε στην επανάληψη 50, λόγω προβλημάτων σύγκλισης στην επανάληψη 46 στα συζυγή πεδία ρυθμού μαζικής ροής. Οι πορείες σύγκλισης της αντικειμενικής συνάρτησης και των περιορισμών παρουσιάζονται στο Σχήμα 7.4. Οι προκύπτουσες γεωμετρίες και τα αντίστοιχα πεδία ροής απεικονίζονται στο Σχήμα 7.5.

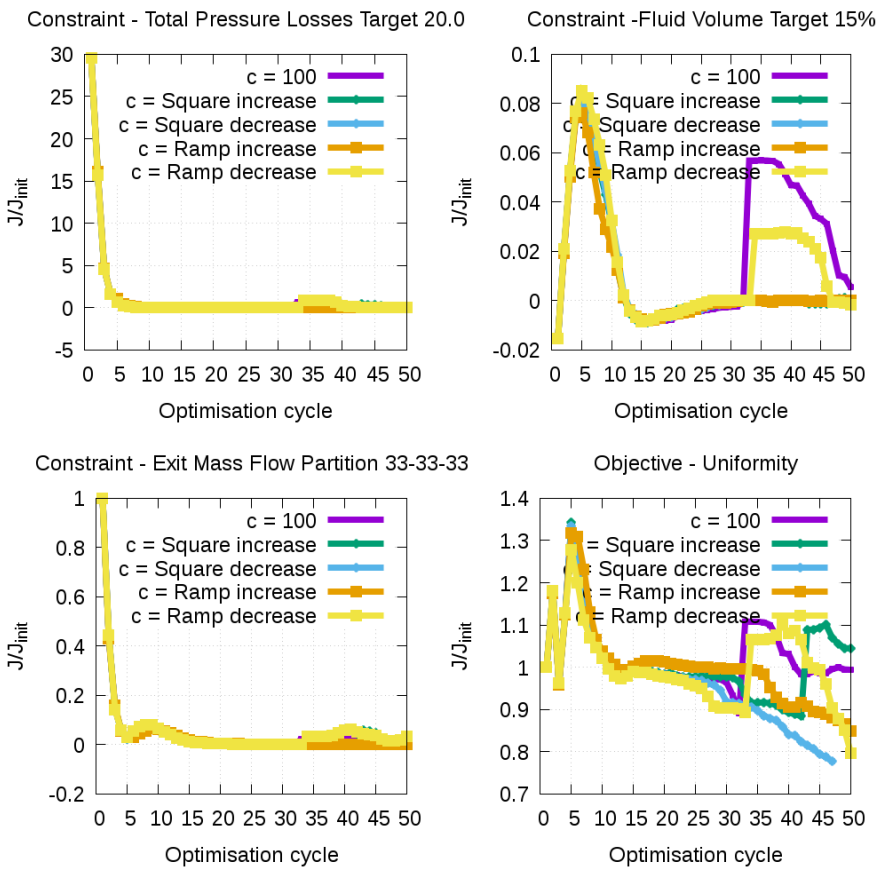

Σχήμα 7.4: Η αντικειμενική συνάρτηση (ομοιομορφία ροής στις εξόδους) και οι περιορισμοί (όγκος TopO, κατανομή παροχής όγκου στις εξόδους και συνολικές απώλειες πίεσης) για το 3D TopO πρόβλημα, με c σταθερό στο 100, καθώς και με τιμές c που μεταβάλλονται γραμμικά και τετραγωνικά (αυξανόμενες και μειούμενες).

Εφαρμογή SQP και Αντιμετώπιση Ανεφικτότητας σε 2D ShpO πρόβλημα

Το ακόλουθο ShpO πρόβλημα αφορά τη μείωση των συνολικών απωλειών πίεσης μιας διδιάστατης τομής του TU Berlin TurboLab πτερύγιου. Η ταχύτητα εισέρχεται στο πεδίο με γωνία προσβολής $-42\,\mathrm{deg}$ και μέγεθος $48m/s$ και εξέρχεται με γωνία $-2\,\mathrm{deg}$ και μηδενική πίεση.

Η ροή του αέρα θεωρείται ασυμπίεστη και τυρβώδης, και επιλέγεται High-Re θεώρηση με χρήση συνάρτησης τοίχου για τον υπολογισμό της $\tilde{\nu}$ στα συνοριακά κελιά του στερεού τοιχώματος. Το κινηματικό ιξώδες του αέρα είναι $\nu = 1.339e-05$. Το πλέγμα αποτελείται από 63.332 κελιά και το κουτί ελέγχου των B-splines παρουσιάζεται στο Σχήμα 7.7. Οι δύο αριστερές και δύο δεξιές στήλες των CPs παραμένουν σταθερές ώστε να αποτραπεί η μείωση του πάχους του άκρου του πτερυγίου. Οι κάτω και πάνω οριακές συνθήκες είναι με κυκλικές συνθήκες.

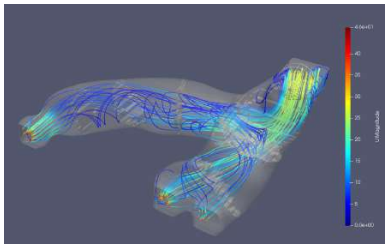

(a) Linearly reduced c.

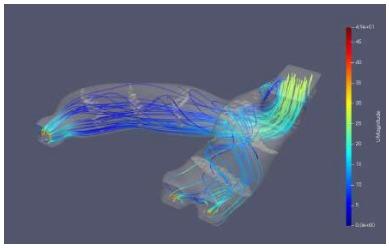

(b) Linearly increased c.

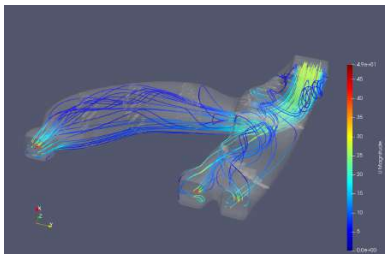

(c) Quadratically reduced c.

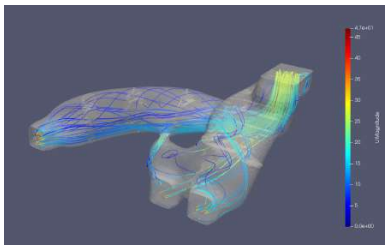

(d) Quadratically increased c.

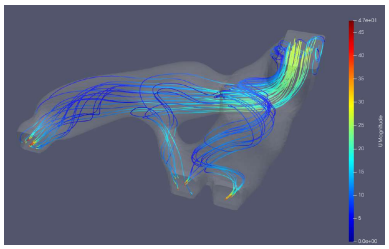

(e) $c = 100$

Σχήμα 7.5: Οι προκύπτουσες γεωμετρίες και οι γραμμές ροής για τις περιπτώσεις με μειούμενες και αυξανόμενες τιμές του c (γραμμικά και τετραγωνικά) καθώς και για την σταθερή τιμή $c = 100$.

Οι οριακές συνθήκες παρουσιάζονται στον Πίνακα 7.3. Ο στόχος αυτής της περίπτωσης είναι η ελαχιστοποίηση των συνολικών απωλειών ολικής πίεσης από την είσοδο στην έξοδο και περιλαμβάνονται δύο περιορισμοί: μέγιστη επιτρεπόμενη μείωση όγκου 20% και ελάχιστη τιμή γωνίας εξόδου ροής 15 deg. Για τις σταθερές τιμές $c = 1$. $c = 100$ και τις μεταβλητές σύμφωνα με τις στήλες του πίνακα 7.4, οι τιμές της αντικειμενικής συνάρτησης και των περιορισμών σε 20 κύκλους βελτιστοποίησης παρουσιάζονται στο Σχήμα 7.4.

Περιοχή	**U**	**p**	$\tilde{\nu}$
Είσοδος	(35.67, -32.11)	μηδενική κλίση	30e-5
Έξοδος	μηδενική κλίση	0	μηδενική κλίση
Πτέρυγα	0	μηδενική κλίση	-

Table 7.3: Οριακές συνθήκες του πρωτεύοντος προβλήματος στο ShpO πρόβλημα.

Σε όλες τις περιπτώσεις, ο περιορισμός γωνίας για τις βελτιστοποιημένες γεωμετρίες παραμένει ανικανοποίητος. Όλες οι ρυθμίσεις του c, εκτός από τις δυναμικά μειούμενες τιμές της 3ης στήλης του Πίνακα 7.4, οδηγούν σε γωνίες ροής εξόδου πάνω από 13 deg και οι περισσότερες από αυτές σε αυξημένες τιμές του στόχου μέχρι 20%. Αυτό επιδεικνύεται επίσης από την ανομοιόμορφη αεροτομή, που απεικονίζεται στις αντίστοιχες βελτιστοποιημένες γεωμετρίες που παρουσιάζονται στα Σχήματα 7.9, για αυξανόμενες ή σταθερές τιμές, $c = 100$ και c που μεταβάλλεται σύμφωνα με την 1η και 2η στήλη του Πίνακα 7.4. Από την άλλη πλευρά, τιμές του c μικρότερες ή ίσες

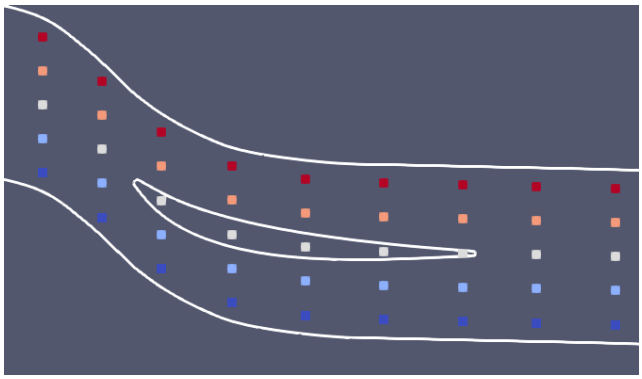

Σχήμα 7.6: Κουτί ελέγχου B-splines για την περίπτωση του Στροβιλοπτερύγιου TU Berlin TurboLab.

Cycle	**1**	**2**	**3**
1	1	0.1	1
30	5	1	0.5
60	5	2	0.2
80	20	5	0.1
100	50	50	0

Table 7.4: Μεταβαλλόμενες τιμές του c.

από 1, οδηγούν σε πτώσεις ολικής πίεσης ίσες με την αρχική τιμή και η αντίστοιχη στρέψη ροής είναι παρόμοια με τα υπόλοιπα τρεξίματα. Τα πεδία πίεσης και ταχύτητας της αρχικής πτέρυγας και των βελτιστοποιημένων παρουσιάζονται στα Σχήματα 7.10 και 7.11.

Συμπεράσματα

Το διαφορετικό σχετικό βάρος της αρχικής αντικειμενικής συνάρτησης και των επιπλέων όρων που σχετίζονται με την ανικανοποίηση των περιορισμών, έδειξε ότι επηρεάζει σε πολλές περιπτώσεις την πορεία σύγκλισης και σε TopO και σε ShpO προβλήματα.

Λανθασμένη, εκ των υστέρων, τιμή του c μπορεί να οδηγήσει ένα 2D TopO πρόβλημα σε λύση, με φραγμένη έξοδο. Μειούμενες τιμές του c έδειξαν ότι παράγουν καλύτερες τιμές της αντικειμενικής συνάρτησης, όπως φαίνεται στο 3D TopO και στο 2D ShpO πρόβλημα.

Η χρήση επιπλέον μεταβλητών σχεδιασμού αντιμετωπίζει επιπλέον προβλήματα με περιορισμούς που δεν μπορούν να ικανοποιηθούν, όπως φαίνεται στα αποτελέσματα του προβλήματος του πτερυγίου. Συγκεκριμένα, ο περιορισμός της γωνίας εξόδου της ροής δεν έφτασε τις 15 μοίρες σε κανένα τρέξιμο, παρ όλα αυτά εξήχθησαν λύσεις σχετικά κοντά στην τιμή αυτή.

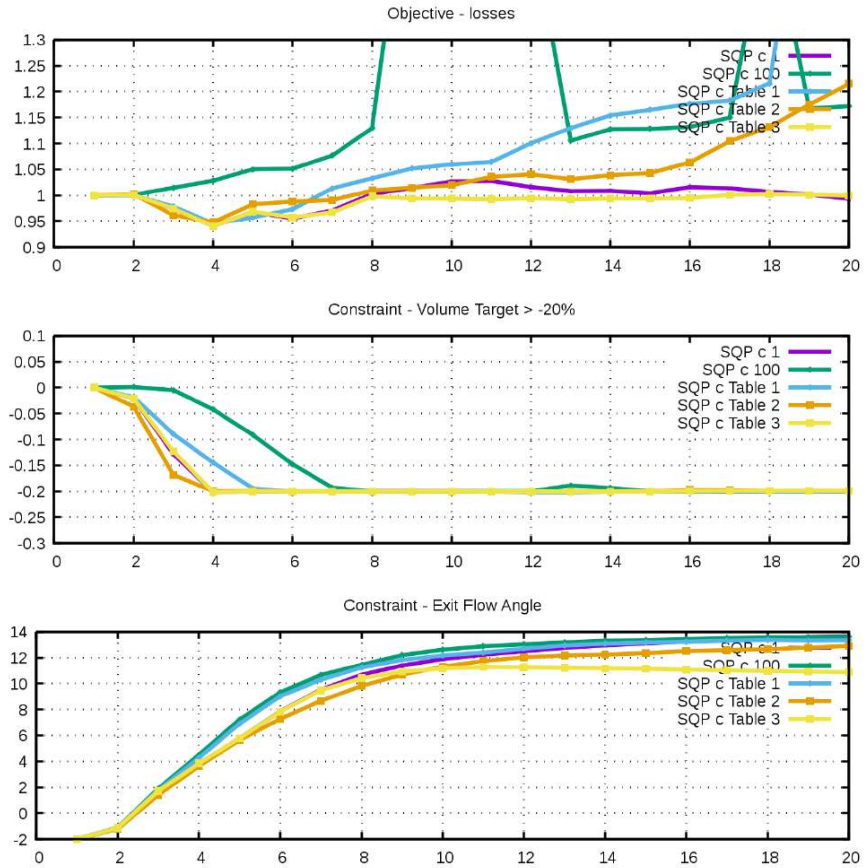

Σχήμα 7.7: Αποτελέσματα στόχου και περιορισμών για διαφορετικές ρυθμίσεις του παράγοντα c στην περίπτωση του σταθερού πτερυγίου TU Berlin TurboLab.

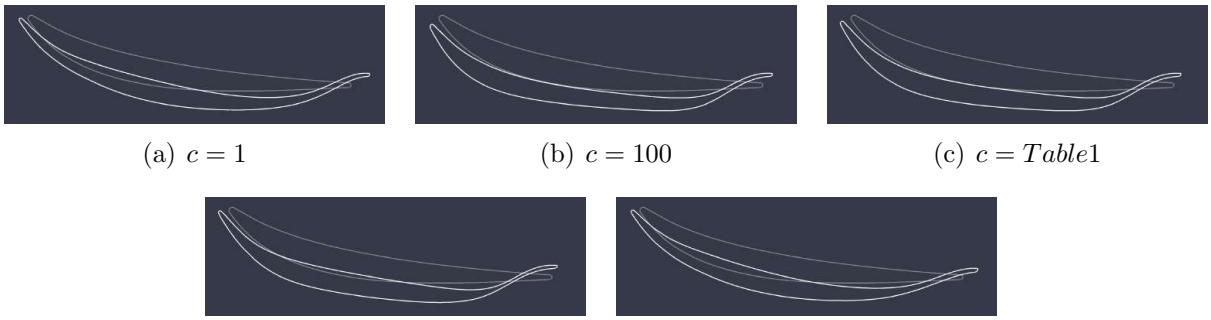

(a) $c = 1$ (b) $c = 100$ (c) $c = Table1$

(d) $c = Table2$ (e) $c = Table3$

Σχήμα 7.8: Βελτιστοποιημένα πτερύγια TU Berlin TurboLab (λαμπρότερες γραμμές) συγκριτικά με την αρχική (αμυδρότερες γραμμές).

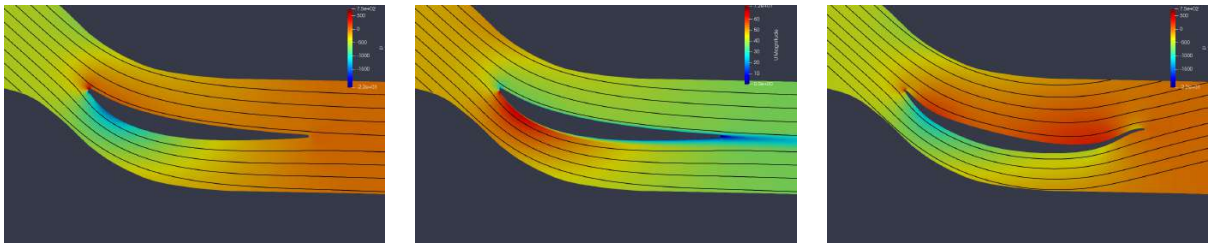

(a) πίεση, αρχική (b) μέγεθος ταχύτητας, αρχική (c) πίεση, $c = 1$

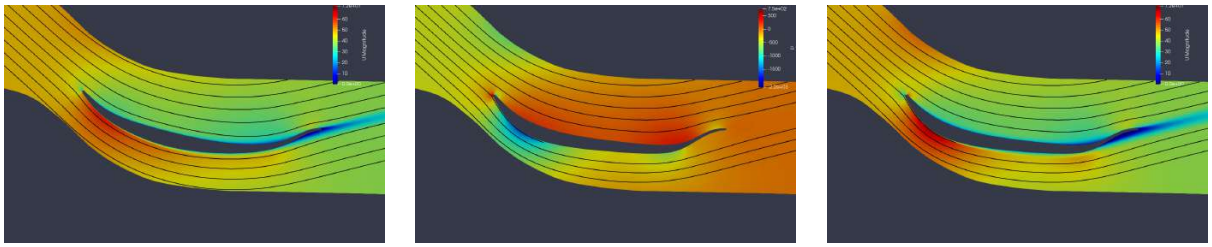

(d) ταχύτητα, $c = 1$ (e) πίεση, $c = 100$ (f) ταχύτητα, $c = 100$

Σχήμα 7.9: Πεδία πίεσης και μεγέθους ταχύτητας για τις αρχικές και βελτιστοποιημένες πτέρυγες για σταθερές τιμές του παράγοντα c.

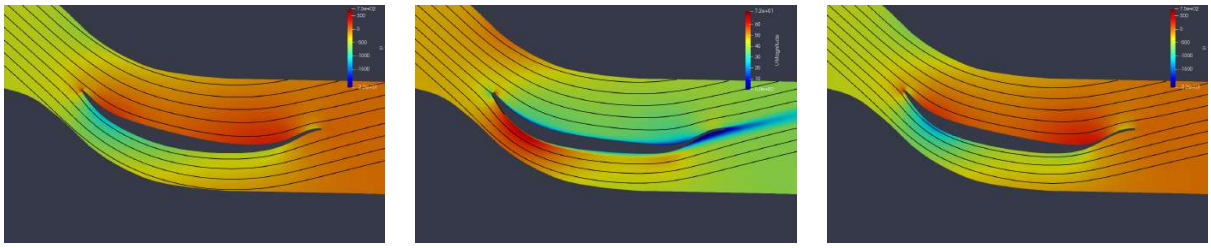

(a) πίεση, $c = Table1$ (b) ταχύτητα, $c = Table1$ (c) πίεση, $c = Table2$

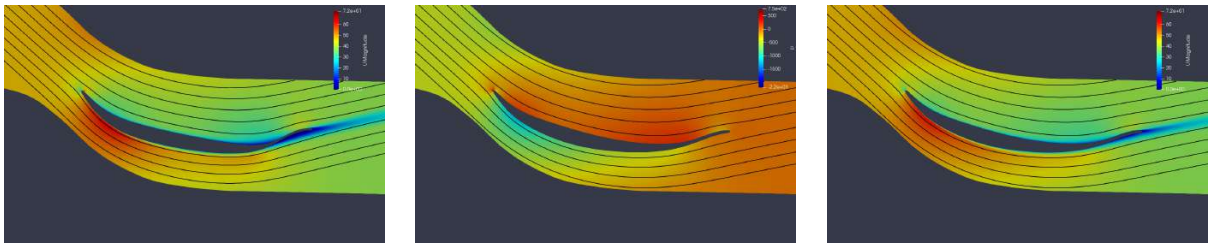

(d) ταχύτητα, $c = Table2$ (e) πίεση, $c = Table3$ (f) ταχύτητα, $c = Table3$

Σχήμα 7.10: Πεδία πίεσης και μεγέθους ταχύτητας για τις βελτιστοποιημένες πτέρυγες για μεταβαλλόμενες τιμές του c.